TECHNISCHE UNIVERSITÄT MÜNCHEN

WALTHER-MEISSNER-INSTITUT FÜR TIEF-TEMPERATURFORSCHUNG

BAYERISCHE AKADEMIE DER WISSENSCHAFTEN

Development of Scalable On-Chip Circuit Quantum Acoustodynamics

Master's Thesis

Christopher Waas

Supervisor: Priv.-Doz. Dr. Hans Hübl

Garching, June 24, 2021

Fakultät für Physik

Technische Universität München

Contents

1 Introduction **1**

2 Theoretical Concepts **3**

2.1 Strain and Stress in Solids . . . 3
2.1.1 Isotropic Materials . . . 3
2.1.2 Piezoelectric Materials . . . 4
2.2 Surface Acoustic Waves . . . 6
2.2.1 SAWs in Isotropic Materials . . . 6
2.2.2 SAWs in Piezoelectric Materials . . . 8
2.2.3 SAWs in Thin-Film Piezoelectric Materials . . . 9
2.3 Coupled Quantum Systems . . . 10
2.3.1 The Jaynes-Cumming Hamiltonian . . . 10
2.3.2 Resonant Regime . . . 12
2.3.3 Dispersive Regime . . . 12
2.4 Superconducting Transmon Qubits . . . 13
2.4.1 Physical Model of the Transmon Qubit . . . 13
2.4.2 Driven Qubit Dynamics . . . 15
2.4.3 Qubit Readout . . . 18
2.4.4 Qubit Decay and Dephasing . . . 18
2.5 Superconducting Microwave Resonators . . . 22
2.5.1 Quality Factor and Loss Rates . . . 22
2.5.2 Mean Photon Number . . . 23
2.6 Surface Acoustic Wave Resonators . . . 23
2.6.1 Interdigitated Transducers . . . 24
2.6.2 Gratings . . . 27
2.6.3 1-port SAW Resonator . . . 30

3 Design & Fabrication **33**

3.1 Design . . . 33
3.1.1 cQED Sample Design . . . 33
3.1.2 Surface Acoustic Wave Elements . . . 36
3.1.3 SAW Resonator Design . . . 37
3.2 Fabrication . . . 38
3.2.1 General Fabrication Process . . . 38
3.2.2 cQED Device Fabrication . . . 39

3.2.3 SAW Device Fabrication . . . 42
3.3 Proximity Effect Correction with BEAMER . . . 42

4 Measurement Setup **45**
4.1 cQED Measurement Setup . . . 45
4.1.1 Frequency Domain Measurements . . . 45
4.1.2 Time Domain Measurement . . . 46
4.2 SAW Measurement Setup . . . 48

5 Experimental Results **51**
5.1 Experimental Results of the Coupled Transmon-Microwave Resonator Device . . . 51
5.1.1 Single-Tone Spectroscopy . . . 51
5.1.2 Two-Tone Spectroscopy . . . 53
5.1.3 Photon Number Calibration . . . 57
5.1.4 Time Domain Measurements . . . 58
5.1.5 Discussion . . . 63
5.2 Surface Acoustic Wave Resonator Measurements . . . 65
5.2.1 Frequency Domain Measurements . . . 65
5.2.2 Time Domain Measurements . . . 69
5.2.3 Discussion . . . 75

6 Outlook & Summary **77**
6.1 Future Prospects: On-Chip cQAD . . . 77
6.2 Summary . . . 78

A Appendix: Theory **79**
A.1 Rotating Frame and Optical Bloch Equations . . . 79
A.1.1 Driven Qubit in the Rotating Frame . . . 79
A.1.2 Optical Bloch Equation . . . 80
A.2 Qubit Frequency Drift . . . 81

B Appendix: Fabrication **83**
B.1 cQED Fabrication . . . 83
B.2 SAW Devices . . . 85

Bibliography **86**

Acknowledgments **95**

Chapter 1

Introduction

Over the last decades, a broad variety of controllable quantum systems was established ranging from single atoms [1, 2] and ensembles of atoms [3, 4] over macroscopic systems like superconducting qubits [5, 6] and mechanical oscillators [7, 8, 9] to large-scale detectors like LIGO [10]. Each platform offers unique advantages. For example, single nuclear spins in solids can exhibit hour-long coherence times [11], superconducting qubits are a promising candidate for scaling the number of interacting quantum systems [12, 13] and rare-earth dopants in solids emit photons in the telecommunication band where fiber losses are minimal [14, 15]. Therefore, combinations of different quantum systems promise exciting physics which pave the way for future applications in quantum computing, simulation and sensing. A few years ago, a physical system known since the late 1800s [16] and widely used in electronic devices as filters since the 1960s [17, 18] experienced its "quantum" renaissance [19]: surface acoustic waves (SAWs). These acoustic waves propagate along the surface of a solid and can be created in a controlled way on piezoelectric substrates. As opposed to other mechanical systems like nanobeams, levitating spheres [20] and mechanical drums [21], SAWs are not stationary but travel with the speed of sound on the order of a few kilometers per second. Therefore, spatially separated quantum systems can be coupled with SAWs. Due to the inherent coupling of mechanical motion to electromagnetic fields provided by the piezoelectric substrate, SAW-based systems are ideally suited to interface the research fields of acoustics and electrodynamics. Analogously to the field of circuit quantum electrodynamics (cQED) [22, 23, 24], where superconducting qubits are coupled with microwaves, circuit quantum acoustodynamics (cQAD) [25, 26, 27, 28, 29, 30] was born exploiting SAWs instead of photons as information carriers. As the propagation velocity ($\mathcal{O}\left(10^3\ \mathrm{m/s}\right)$) is around five orders of magnitude lower than the speed of light ($\mathcal{O}\left(10^8\ \mathrm{m/s}\right)$), this coupling allows for the investigation of new physical regimes inaccessible by conventional coupling via photons. For instance, quantum systems can be manipulated during the propagation of the SAW, enabling quantum shift registers. As the wavelength of SAWs for GHz-frequencies is in the sub-micron range, giant artifical atoms - where the atom dimensions are much larger than the wavelength of the emitted excitation carrier - can be realized [31, 32, 33], opening the door to non-Markovian quantum experiments [34].

In this thesis, we tackle the challenge of on-chip coupling of superconducting qubits to surface acoustic wave devices. A piezoelectric substrate is essential for the creation of SAWs, but forms a strong loss channel for qubits and superconducting circuits as the electromagnetic energy in

the quantum system can be spontaneously converted to mechanical strain. Therefore, cQAD experiments use weak piezoelectric materials [27, 29] or flip chip settings to combine a low-loss qubit substrate and piezoelectric SAW substrate [28, 30]. These solutions have limitations in qubit coherence and scalability, respectively. Our ansatz to cQAD is to realize an on-chip consolidation of a low-loss substrate for superconducting qubits and microwave resonators and strong piezoelectric materials with maximum electromagnetic-to-mechanical conversion for the efficient generation and readout of SAWs. To this end, we choose to investigate a multi-layer system comprised of thin-film lithium niobate on silicon. Lithium niobate (LNO) is a well established bulk material, has a strong piezoelectric coupling [18] and is also used in the optics community as material for photonic waveguides [35, 36]. Special wafer orientations, such as the used 128°-Y-X cut, have been found to exhibit high SAW generation [37]. On the other hand, silicon is a well-known substrate for microwave as well as CMOS technology and is a standard substrate used for cQED experiments.

We start with a basic survey of piezoelectricity, surface acoustic waves and the physics of coupled quantum systems in the form of qubits and quantum harmonic oscillators. Subsequently, the concepts, designs and fabrication of the three implemented systems - superconducting qubits, superconducting microwave resonators and SAW resonators - are discussed.

We design, fabricate and measure samples for cQED and SAW experiments respectively, investigating a newly introduced fabrication process for superconducting qubits and the acoustic properties of a lithium niobate thin-film.

Lastly, we conclude the thesis with a brief summary and an outlook on future work in order to realize the combination of cQED and SAW devices on a single chip.

Chapter 2

Theoretical Concepts

The realization of circuit quantum acoustodynamic (cQAD) experiments requires the coupling of circuit quantum electrodynamics (cQED) elements such as superconducting qubits and superconducting resonators with acoustic resonators. In this field of physics, electromagnetic waves are coupled with acoustic waves, which can be elegantly accomplished using the concept of piezoelectricity (see sec. 2.1), which appropriately desigend allows to excite surface acoustic waves (see sec. 2.2). In sec. 2.3, we will give a brief overview of the physics describing the interaction of a coupled qubit and resonator. We introduce the Jaynes-Cummings model, which describes the interaction of a qubit with a single mode of a resonator [23].After the introduction of the model, we will discuss three specific quantum systems used in the context of quantum acoustic devices: (i) superconducting transmon qubits (sec. 2.4), (ii) superconducting microwave resonators (sec. 2.5) and (iii) surface acoustic wave resonators (sec. 2.6). While (i) & (ii) are established building blocks for superconducting quantum circuits [12, 38, 39], surface acoustic wave resonators have predominantly been studied in the context of delay lines and bandpass frequency filters [40]. More recently, a new interest in surface acoustic wave devices has evolved for their use in quantum acoustodynamics, where they are used as phonon based components integrated into quantum circuits [30, 25]. Therefore, we will present a short overview concerning superconducting qubits and resonators and a more comprehensive description of surface acoustic wave devices.

2.1 Strain and Stress in Solids

For cQAD experiments, surface acoustic waves (SAWs) on piezoelectric materials are used as information carrier between superconducting qubits. These waves travel along the surface of a solid and, in contrast to bulk acoustic waves, penetrate into the solid only on the order of a wavelength. While piezoelectric substrates are more relevant in experiments, analytic solutions for SAWs are often only available for isotropic materials. Hence, we start with a brief introduction of strain and stress in isotropic materials (sec. 2.1.1). The obtained equations of motion for the lattice atoms can be used to derive surface acoustic wave solutions. Subsequently, we introduce the concept of piezoelectricy and modify the equations of motion for piezoelectric materials (sec. 2.1.2). In this section, we closely follow the treatment of SAWs in Chapter 2 of Ref. [18].

2.1.1 Isotropic Materials

Forces acting on a rigid crystal cause the crystal atoms to be displaced from their equilibrium position. Typically these forces are expressed in terms of *stress* T and the distortion of the atoms

as *strain* S. For an atom with equilibrium position (x_1, x_2, x_3) displaced by (u_1, u_2, u_3), the strain is a second order tensor defined as

$$S_{ij} = \frac{1}{2}\left(\frac{\partial u_i}{\partial x_j} + \frac{\partial u_j}{\partial x_i}\right) \qquad i, j = 1,2,3. \tag{2.1}$$

This definition guarantees that translational and rotational movements of the crystal as a whole lead to no strain. The tensor is symmetric, meaning $S_{ij} = S_{ji}$.
The stress T_{ij} is defined as the force per unit area exerted along x_i acting on a surface with normal vector x_j [41]. To prevent any rotational moment caused by stresses, it can be shown that the stress tensor also is symmetrical, i.e. $T_{ij} = T_{ji}$. Stress can either be applied from the outside or caused by internal strains. In the linear response regime, the relation between stress and strain is linear and the stiffness tensor c_{ijkl} is defined by

$$T_{ij} = \sum_k \sum_l c_{ijkl} S_{kl} \qquad i, j, k, l = 1,2,3. \tag{2.2}$$

The stiffness tensor generally has 36 independent variables of the 81 total elements due to the symmetry relations of T_{ij} and S_{ij}. Furthermore, it can be shown that the first and second pair of indices of the stiffness tensor can be interchanged, i.e. $c_{ijkl} = c_{klij}$, leaving only 21 independent entries.
Using Newton's second law, the equation of motion (EOM) for atoms around their equilibrium position is

$$\rho \frac{\partial^2 u_i}{\partial t^2} = \sum_j \frac{\partial T_{ij}}{\partial x_j}, \tag{2.3}$$

where ρ is the material mass density and $i, j = 1,2,3$.

2.1.2 Piezoelectric Materials

Piezoelectricity is the property of some anisotropic materials to produce electric fields when exposed to elastic stress and vice versa. This can happen due to the lack of a symmetry center in the materials. Fig. 2.1 shows a simple structure of ions without an inversion center. In equilibrium, the center of both charge types are identical and there is no polarization (panel a)). However, an applied force (panel b)) shifts ions by a displacement u and consequently the charge centers relative to each other. Note, that the displacement is different for each ion as illustrated in fig. 2.1b), where ions of the same kind undergo different displacements from their equilibrium state (dashed circles). This creates a finite polarization P and therefore an electric displacement D. The total electric displacement inside the material is then given by the electric field $\vec{E}$ and the piezoelectric contribution due to the strain and can be expressed as [41]

$$D_i = \sum_j \epsilon_{ij}^S E_j + \sum_j \sum_k e_{ijk} S_{jk}, \tag{2.4}$$

where ϵ_{ij}^S is the electrical permittivity tensor for constant strain. The piezoelectric tensor e_{ijk} connects electric and elastic fields and is symmetric in the last two indices $e_{ijk} = e_{ikj}$ due to the

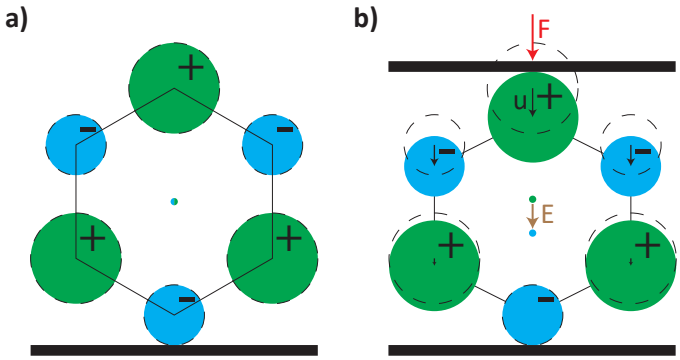

Figure 2.1: Illustration of the ion arrangement in a piezoelectric material. **a)** Equilibrium state with aligning charge centers. **b)** Force is applied along a polar axis compressing the cell. The following displacement of the ions leads to a relative shift of the charge centers and creates a finite polarization. The inverse effect with an applied electric field creates a contraction or elongation of the cell due to different displacement directions of the differently charged ions.

symmetry of S_{ij}.

For the inverse piezoelectric effect, an electric field E is applied leading to an electric displacement $D_i = \epsilon_{ij} E_j$. The electric displacement favors a different motional displacement for the charged ions which leads to a contraction or elongation of the crystal along the axis of the applied field. Usually, this contribution is denoted as an additional term in the stress of the material by

$$T_{ij} = \sum_k \sum_l c^E_{ijkl} S_{kl} - \sum_k e_{kij} E_k. \tag{2.5}$$

Similarly to above, the superscript in c^E_{ijkl} denotes a constant electric field. Usually, the quasi-static approximation is used to express electrical fields by a potential Φ [18]

$$E_i = -\frac{\partial \Phi}{\partial x_i}. \tag{2.6}$$

This approximation is legitimate as phonons propagate with the speed of sound ($\approx 1 \times 10^3\,\mathrm{m/s}$) while electromagnetic fields propagate as electromagnetic waves with a reduced speed of light in the material ($c \approx 1 \times 10^8\,\mathrm{m/s}$).
These more complex relations also lead to a modification of the EOM. Assuming the piezoelectric material to be an insulator ($\mathrm{div}\,\vec{D} = 0$), one can obtain the following relations [18]:

$$\rho \frac{\partial^2 u_i}{\partial t^2} = \sum_j \sum_k \left[e_{kij} \frac{\partial^2 \Phi}{\partial x_j \partial x_k} + \sum_l c^E_{ijkl} \frac{\partial^2 u_k}{\partial x_j \partial x_l} \right], \tag{2.7}$$

$$0 = \sum_i \sum_j \left[\epsilon^S_{ij} \frac{\partial^2 \Phi}{\partial x_i \partial x_j} - \sum_k e_{ijk} \frac{\partial^2 u_j}{\partial x_i \partial x_k} \right]. \tag{2.8}$$

Eq. 2.7 is a modified version of eq. 2.3 with an additional contribution of the piezoelectric tensor

e_{kij}. Spatial variations of the electric potential Φ induce an additional acceleration of the lattice atoms. Eq. 2.8 is a consequence of the assumption of an insulating material ($\operatorname{div} \vec{D} = 0$) and eq. 2.4. As there are no free charges, variations in the electric field can only be induced by the displacement of lattice atoms in the piezoelectric material and the consequent effective electric displacement. Eqs. 2.7 and 2.8 give four relations between the lattice displacement u_i and the electric potential Φ [18]. With appropriate boundary conditions, this gives a distinct solution for Φ and (u_1,u_2,u_3), however these equations have to be evaluated numerically in most piezoelectric cases [18].
A very important measure for the strength of a piezoelectric material is the piezoelectric coupling coefficient K^2 [42]

$$K^2 = \frac{e_{33}^2}{\epsilon_{33}^S c_{33}^E}. \tag{2.9}$$

The coupling coefficient quantifies the efficiency with which mechanical strain is converted to electric fields and vice versa. K^2 is calculated by the piezoelectric, permittivity and stiffness tensor values along the surface normal and is therefore strongly dependent on the crystal orientation.

2.2 Surface Acoustic Waves

Surface accoustic waves (SAWs) are mechanical confined to an interface, i.e. the surface of a substrate. Their penetration depth into the substrate is on the order of one wavelength. The phenomenon was first reported by Lord Rayleigh in 1885 [16]. The surface acoustic wave solution that he discovered is therefore also known as the Rayleigh wave. Since the EOM for piezoelectric materials are usually not analytically solvable [43, 18], we will discuss the analytic solution for SAWs on isotropic (i.e. non-piezoelectric) materials to get an understanding of the fundamental principles in a simple picture. A short qualitative description of SAWs in anisotropic materials will be given afterward.

2.2.1 SAWs in Isotropic Materials

Figure 2.2a) shows a bulk crystal on which SAWs propagate as indicated by lattice displacements. We define a coordinate system with x_1 being the propagation direction and x_3 the surface normal. With this definition, the Rayleigh wave is uniform along x_2, and the displacement only takes place in the sagittal plane spanned by x_1 and x_3. The Rayleigh wave is the solution of eq. 2.3 for an infinite half-space, meaning the isotropic material expands infinitely in x_1 and x_2, and into the negative x_3 direction. For $x_3 > 0$, we assume vacuum. This leads to the boundary conditions $T_{13} = T_{23} = T_{33} = 0$ at $x_3 = 0$ since there can be no stress at the free surface of the substrate [43, 18, 45]. To solve eq. 2.3 with these boundary conditions, the Rayleigh wave is constructed out of two partial waves [18], a plane longitudinal wave with phase velocity v_l and a plane shear wave (w.r.t. the sagittal plane) with v_t. The respective strains S_{11}, S_{33} and S_{13} are illustrated, all displacements decay in the negative x_3 direction. This is a necessary condition for a confinement confinement to the surface. Therefore, it can be shown that the phase velocity of the Rayleigh wave v_R has to obey [18]

$$v_\mathrm{R} < v_\mathrm{t}. \tag{2.10}$$

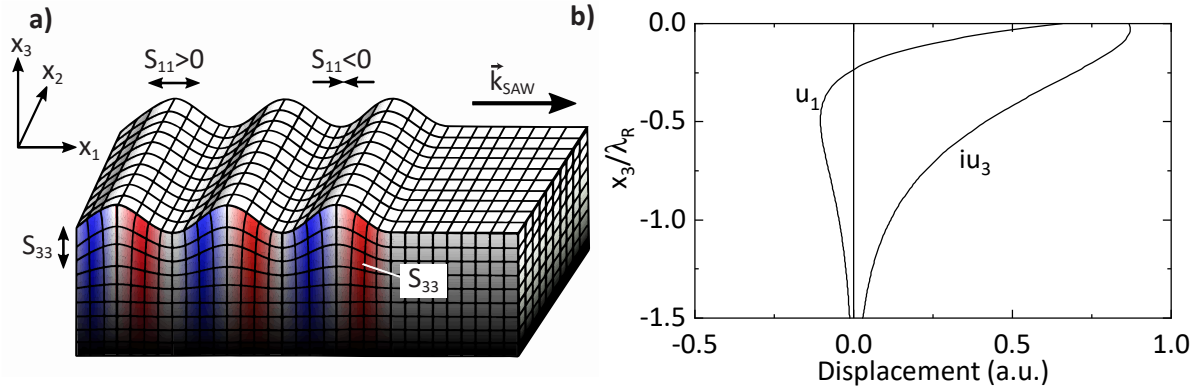

Figure 2.2: **a)** Schematic representation of a Rayleigh wave. Rayleigh waves propagate along x_1 and have no deflection along x_2, the movement is confined in the sagittal plane spanned by x_1 and x_3. The strain S_{11} and S_{33} parallel/orthogonal to the wave vector $\vec{k}_{\mathrm{SAW}}$ decays in negative x_3 direction. Positive and negative strain of the shear vertical strain S_{13} is illustrated in blue and red. Figure adapted from [44]. **b)** Displacement of particles for a Rayleigh wave in dependence of the depth in fused quartz with $v_{\mathrm{l}}/v_{\mathrm{t}} \approx 1.48$. u_1 and u_3 have a 90° phase shift leading to an elliptical movement. See text for further explanation. Figure adapted from [18].

Note, that this implies $v_{\mathrm{R}} < v_{\mathrm{l}}$ since $v_{\mathrm{t}} < v_{\mathrm{l}}$. This gives an upper bound for the speed of Rayleigh waves depending on the material. v_{R} can be shown to be the solution of [18]

$$\left(2 - \frac{v^2}{v_{\mathrm{t}}^2}\right)^2 = 4\sqrt{1 - \frac{v^2}{v_{\mathrm{t}}^2}}\sqrt{1 - \frac{v^2}{v_{\mathrm{l}}^2}}. \tag{2.11}$$

There is only one real-valued solution fulfilling $v^2 < v_{\mathrm{t}}^2$. With the now known v_{R}, it is possible to calculate the displacements of the material as a function of the depth $-x_3$ [18]. Fig. 2.2b) shows the displacement amplitudes u_1 and u_3 depending on the depth in the substrate $-x_3$ which is normalized by the Rayleigh wavelength $\lambda_{\mathrm{R}} = 2\pi v_{\mathrm{R}}/\omega$, where ω is the angular frequency of the propagating wave. Exemplarily, at each given depth $-x_3$ and a fixed position x_1 the lattice atoms perform a motion given by

$$\vec{u} = \mathrm{Re}\left[(u_1\vec{x}_1 + iu_3\vec{x}_3)e^{i\omega t}\right]. \tag{2.12}$$

The phase shift of 90° between u_1 and u_3 leads to an elliptical motion. At $-x_3 \approx 0.2\lambda_{\mathrm{R}}$, the sign of u_1 and therefore also the direction of rotation changes. Both motions decay quickly within one wavelength.

The exact displacements at a fixed moment in time are visualized in fig. 2.3. The dots indicate particles in equilibrium while the lines show the displacement when subjected to a Rayleigh wave for a fixed moment in time. Following a line of particles downwards into the substrate, the decay of the motional amplitude is clearly visible. A picture of particle motion in time can be obtained by following a line of particles horizontally in opposite direction of the propagation[1]. The motion close to the surface is retrograde while the motion deeper in the substrate is prograde.

[1] The rotation takes place following $\vec{u} \propto \exp[k(x_1 - v_{\mathrm{R}}t)]$, so moving backwards in space gives the same picture as moving forwards in time.

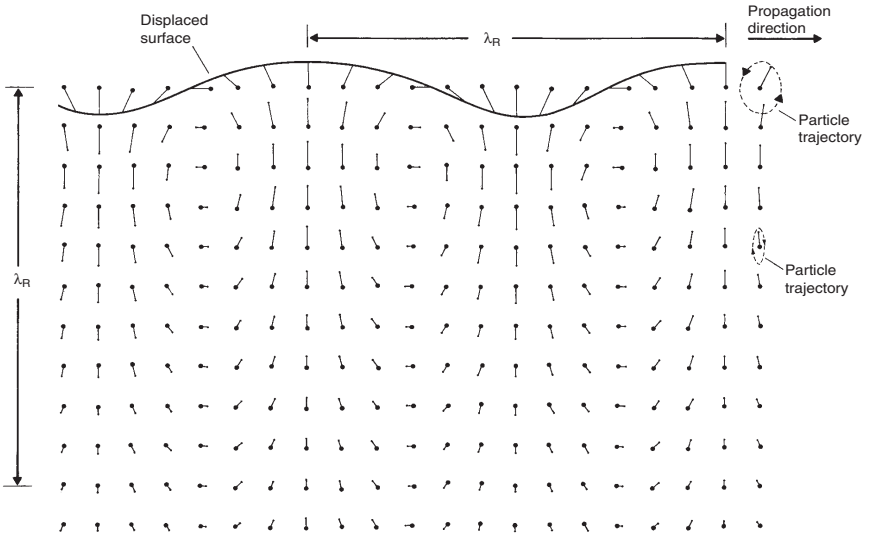

Figure 2.3: Displacements of particels (dots) subjected to a Rayleigh wave at a given moment in time. The rotation is retrograde at the surface and prograde deeper down in the substrate. Figure from [18].

2.2.2 SAWs in Piezoelectric Materials

Surface wave solutions of equations 2.7 and 2.8 are generally complicated and require numerical calculations. In most cases, there are one or more SAW solutions for piezoelectric materials [18], however we are interested in the *piezoelectric Rayleigh wave*. It is a modified version of the isotropic Rayleigh wave with respect to anisotropy and piezoelectricity. A crucial feature of SAWs in piezoelectric materials is the different phase velocity depending on whether the substrate is metallized or not. For metallized surfaces, the parallel electric field component E_1 has to be zero while this does not have to be the case for non-metallized substrates. For a piezoelectrically coupled SAW, the free-space phase velocity v_f is always larger than the metallized velocity v_m [18]. These phase velocities lead to an alternative definiton of the electromechanical coupling coefficient[2]

$$K^2 = 2\frac{v_\mathrm{f} - v_\mathrm{m}}{v_\mathrm{f}} = 2\frac{\Delta v}{v}. \tag{2.13}$$

As for the isotropic case, the phase velocity of the Rayleigh wave must be smaller than the slowest of the partial waves contributing to the Rayleigh wave. Furthermore, the crystal displacement is bound to the sagittal plane. In the piezoelectric case, the wave is not strictly bound to the sagittal plane which allows a composition of all three plane wave types of an infinite material: longitudinal, fast shear and slow shear waves. However, the Rayleigh phase velocity is still bound by the lowest velocity of the contributing plane waves. For the piezoelectric Rayleigh wave solution, the displacement vector $\vec{u}$ is (at least almost) parallel to the sagittal plane.

[2]Note that this is the definition used in most of the literature, however Ref. [18] defines K^2 without the factor of 2.

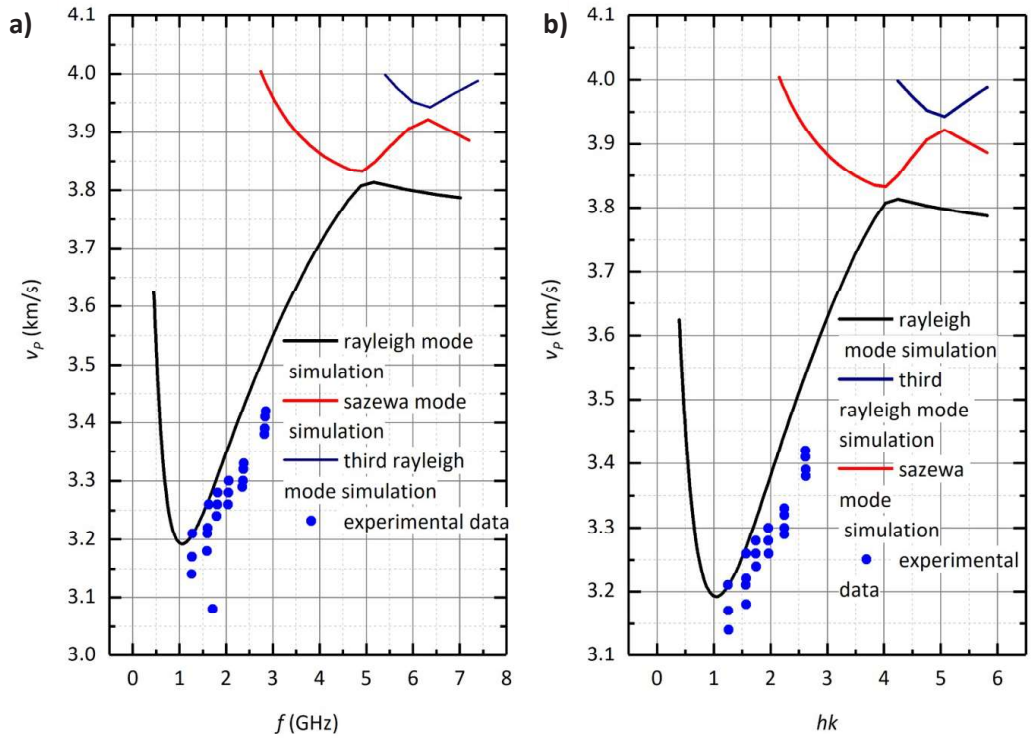

Figure 2.4: Phase velocity of SAW modes plotted against **a)** frequency f and **b)** kh with h being the LNO film thickness. In addition to the discussed first order Rayleigh mode, Sezewa and higher Rayleigh modes are shown. Figure taken from [46].

2.2.3 SAWs in Thin-Film Piezoelectric Materials

When investigating a stack of (piezoelectric) thin-film substrate layers on a bulk material, the solutions for SAWs can become more complex. Since SAWs decay on the order of a wavelength into the substrate, different scenarios can be observed. The SAW can be hosted either just in the top thin-film layer for very short wavelengths or all material layers of the stack for very long wavelengths. While the former case is quite similar to the discussion of a bulk piezoelectric substrate, the latter case leads to a more complex SAW behavior as the sound velocities of the layers involved in the propagation of the SAWS can differ. This results in a wavelength- and therefore also frequency-dependent phase velocity of the SAW. In the experiments discussed in sec. 5.2, we use a stack of (100)-silicon (350µm), silicon oxide (2µm) and 128°Y-X cut lithium niobate (500nm). Hence, we need to discuss the properties of the SAWs in ths more complex arrangement. Fig. 2.4 shows a simulation of the SAW velocities for this stack. In panel a), the phase velocities of different SAW solutions, including Rayleigh waves and other higher mode solutions like Sezewa modes, on the stack are plotted as a function of their frequency, in panel b) as a function of the lithium niobate (LNO) film thickness h and the wavevector $k = 2\pi/\lambda$ (figure taken from Ref. [46]). For long wavelengths, i.e. small kh, the wave penetrates deeply into the substrate and is mainly supported by the bulk silicon ($v_\mathrm{l} = 8433\,\mathrm{m/s}$ [47]). As the wavelength is decreased, the wave is supported mostly by the silicon oxide layer with a transversal speed of sound $v_{\mathrm{t,SiOx}} = 3159\,\mathrm{m/s}$ [18]. For very short wavelengths, i.e. large kh, the SAW is hosted in the

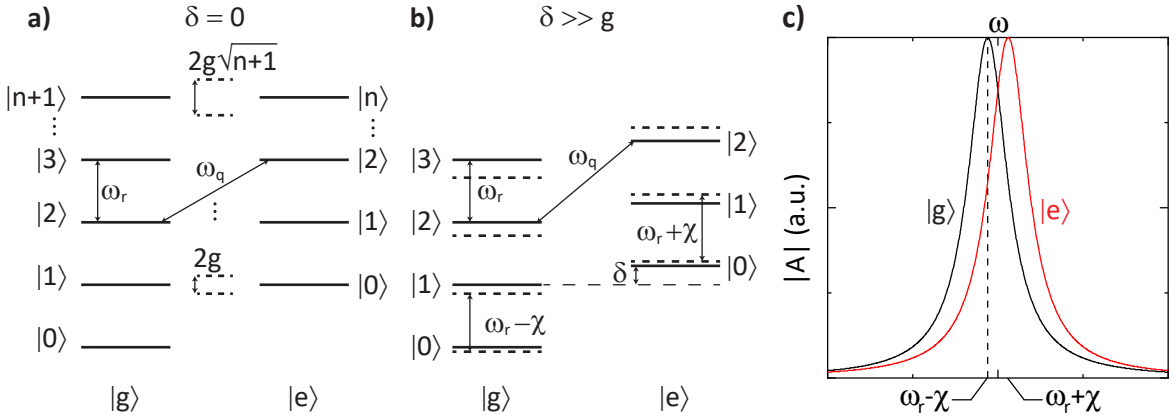

Figure 2.5: Energy eigenstates of a combined qubit-resonator system in the Jaynes-Cummings regime. **a)** Jaynes-Cummings Ladder at $\delta = 0$, i.e. $\omega_\mathrm{r} = \omega_\mathrm{q}$ (resonant regime). Levels with the same amount of energy quanta are degenerate and form pairs for zero coupling g (solid lines). Finite coupling lifts the degeneracy and introduces a level-splitting scaling with $\sqrt{n}$ (dashed lines). **b)** Jaynes-Cummings Ladder for large detuning of qubit and resonator compared to the coupling, i.e. $|\delta| \gg g$ (dispersive regime). For zero coupling, energy levels with an excited qubit state are shifted by δ with respect to levels with the qubit in the ground state $|g\rangle$ (solid lines). Finite coupling leads to a dispersive shift χ, i.e. the level separation of the oscillator depends on the state of the two-level system (dashed lines). Shown is the case for $\delta > 0$. **c)** Frequency response of a driven harmonic oscillator. Probing the harmonic oscillator at a fixed frequency (dashed line) leads to a different response depending on the state of the qubit.

LNO layer, approaching the transversal velocity of 128°Y-X LNO $v_{\mathrm{l,LNO}} = 3979\,\mathrm{m/s}$. Hence, a strong frequency dependence in the SAW phase velocity is expected at the working frequencies of the investigated device ($\approx 5\,\mathrm{GHz}$) which has to be taken into account during the design process of SAW devices with different working frequencies.

2.3 Coupled Quantum Systems

In this section, we will focus on the physics of a coupled quantum system consisting of a two-level system and a quantum harmonic oscillator. The physics are described by the Jaynes-Cummings Hamiltonian. Here, we provide a qualitative discussion of the dispersive and resonant regime.

2.3.1 The Jaynes-Cumming Hamiltonian

A quantum harmonic oscillator [48] is the quantum-mechanical equivalent of a classical harmonic oscillator with eigenfrequency ω_r and bosonic ladder operators $\hat{a}$, $\hat{a}^\dagger$ fulfilling $\hat{a}^\dagger\hat{a} = \hat{n}$, where $\hat{n}$ is the number operator. The ladder operators fulfill the bosonic commutation relation $\left[\hat{a}, \hat{a}^\dagger\right] = 1$. The harmonic oscillator Hamiltonian takes the form

$$\hat{H}_\mathrm{r}/\hbar = \omega_\mathrm{r}\left(\hat{a}^\dagger\hat{a} + \frac{1}{2}\right), \tag{2.14}$$

with $\hbar = h/2\pi = 1.0546 \times 10^{-34}\,\mathrm{Js}$ being the reduced Planck constant. All energy levels are equally spaced by ω_r and usually labeled as Fock states $|n\rangle$ according to the expectation value n of the number operator $\hat{n}$.
The two-level system is described by a Hamiltonian of the form [49]

$$\hat{H}_\mathrm{q}/\hbar = \frac{\omega_\mathrm{q}}{2}\hat{\sigma}_\mathrm{z}, \tag{2.15}$$

where $\hbar\omega_\mathrm{q}$ is the energy splitting[3] of the two levels and $\hat{\sigma}_\mathrm{z}$ is the third Pauli matrix with eigenstates $|e\rangle$ and $|g\rangle$. The corresponding eigenenergies are $E_\mathrm{e}/\hbar = \omega_\mathrm{q}/2$ and $E_\mathrm{g}/\hbar = -\omega_\mathrm{q}/2$. Fig. 2.5a) and b) show the energy levels of the sum of Hamiltonians from eqs. 2.14 and 2.15 with solid lines [22]. If the system is degenerate (panel a)), i.e. $\delta = \omega_\mathrm{q} - \omega_\mathrm{r} = 0$, pairs of energy levels are formed by the states $|g, n+1\rangle$ and $|e, n\rangle$; only $|g, 0\rangle$ is a singlet unpaired. For $\delta \neq 0$, we find that there are no degenerate states, the branch for the two-level system state $|e\rangle$ is shifted by δ relative to the branch of $|g\rangle$.

Up to this point in the discussion, no interaction between the harmonic oscillator and the two-level system was considered. Such interaction can be taken into account by introducing a dipole interaction Hamiltonian $H_\mathrm{I} \propto \hat{d} \cdot \hat{E}$ with coupling strength g, that couples the resonator field amplitude $\hat{E} \propto (\hat{a} + \hat{a}^\dagger)$ and the qubit electric dipole $\hat{d} \propto (\hat{\sigma}_+ + \hat{\sigma}_-)$. This is the *dipole approximation* which is applicable if the dimension of the qubit is much smaller than the wavelength of the coupled mode in the resonator [50]. The raising and lowering operators for the two-level system $\hat{\sigma}_\pm = (\hat{\sigma}_\mathrm{x} \pm \hat{\sigma}_\mathrm{y})/2$ induce qubit transitions from $|g\rangle$ to $|e\rangle$ $(\hat{\sigma}_+)$ and from $|e\rangle$ to $|g\rangle$ $(\hat{\sigma}_-)$, respectively.
The resulting total Hamiltonian $\hat{H}_\mathrm{QR} = \hat{H}_\mathrm{r} + \hat{H}_\mathrm{q} + \hat{H}_\mathrm{I}$ is known as the quantum Rabi model

$$\hat{H}_\mathrm{QR}/\hbar = \omega_\mathrm{r}\hat{a}^\dagger\hat{a} + \frac{\omega_\mathrm{q}}{2}\hat{\sigma}_\mathrm{z} + g(\hat{a}^\dagger + \hat{a})(\hat{\sigma}_+ + \hat{\sigma}_-). \tag{2.16}$$

For better readability, we will neglect the constant energy offset $\omega_\mathrm{r}/2$ caused by the harmonic oscillator ground state energy from now on. In the regime where $|\omega_\mathrm{q} - \omega_\mathrm{r}| \ll \omega_\mathrm{q} + \omega_\mathrm{r}$, the Hamiltonian can be simplified by a rotating wave approximation [51, 49] to the Jaynes-Cummings Hamiltonian

$$\hat{H}_\mathrm{JC}/\hbar = \omega_\mathrm{r}\hat{a}^\dagger\hat{a} + \frac{\omega_\mathrm{q}}{2}\hat{\sigma}_\mathrm{z} + g(\hat{a}^\dagger\hat{\sigma}_- + \hat{a}\hat{\sigma}_+). \tag{2.17}$$

This Hamiltonian can be diagonalized [22] leading to eigenstates (also known as dressed states)

$$|+, n\rangle = \cos(\theta_n)\,|e, n\rangle + \sin(\theta_n)\,|g, n+1\rangle\,, \tag{2.18}$$
$$|-, n\rangle = -\sin(\theta_n)\,|e, n\rangle + \cos(\theta_n)\,|g, n+1\rangle\,, \tag{2.19}$$

for pairs of states with the same amount of energy quanta $n+1$, and a ground state $|g, 0\rangle$. The

[3] We conveniently introduce ω_r as the harmonic oscillator (or resonator) frequency and ω_q as the qubit transition frequency as we will use this notation in later chapters as well.

mixing angle is defined as $2\theta_n = \arctan\left(2g\sqrt{n+1}/\delta\right)$. The corresponding eigenenergies are

$$E_{\pm,n}/\hbar = \omega_\mathrm{r}\left(n+\frac{1}{2}\right) \pm \frac{1}{2}\sqrt{4g^2\left(n+1\right)+\delta^2}, \tag{2.20}$$

$$E_{\mathrm{g},0}/\hbar = -\frac{\omega_\mathrm{r}}{2}. \tag{2.21}$$

We distinguish two cases which will be discussed now: the resonant regime with $\delta = 0$ and the dispersive regime where $\delta \gg g$.

2.3.2 Resonant Regime

In the resonant regime, i.e. $\delta = 0$, we find $\theta_n = \pi/4$ and therefore a maximal entanglement of the originally degenerate states [22]. The eigenenergies of the dressed states are split by $2g\sqrt{n+1}$ and centered around the energy level of the uncoupled states as shown in fig. 2.5a). This leads to vacuum Rabi oscillations [49] where the initial excitation of e.g. $|e,n\rangle$ will be coherently passed to a resonator photon $|g,n+1\rangle$ and back with a frequency of $g\sqrt{n+1}/\pi$.

2.3.3 Dispersive Regime

A consequence of the Jaynes-Cumming Hamiltonian in the dispersive regime $\delta \gg g$ can be seen by transforming eq. 2.17 with $\hat{U} = \exp\left[g(\hat{a}\hat{\sigma}_+ + \hat{a}^\dagger\hat{\sigma}_-)/\delta\right]$ and expanding the resulting Hamiltonian up to the second order in $g/\delta \ll 1$ leading to [22]

$$\hat{H}^{(2)}_\mathrm{JC}/\hbar = \left(\omega_\mathrm{r} + \chi\hat{\sigma}_\mathrm{z}\right)\hat{a}^\dagger\hat{a} + \frac{1}{2}\left(\omega_\mathrm{q}+\chi\right)\hat{\sigma}_\mathrm{z}. \tag{2.22}$$

As the first term indicates, the resonance frequency of the harmonic oscillator is now dependent on the state of the two-level system. Fig. 2.5b) visualizes the energy spectrum of eq. 2.22. The resonator level spacing is decreased by χ if the qubit is in the ground state and increased by χ for an excited qubit. This so-called **dispersive shift** χ is of crucial importance for readout schemes using the resonator to determine the qubit state. This way, a *non-demolition measurement* can be realized, i.e. the qubit maintains its state after the readout[4] as long as the resonator is not occupied with more than a critical photon number $\langle n_\mathrm{crit}\rangle$ [22]. Furthermore, measuring the frequency response of a harmonic oscillator is very precise as microwave frequency analysis technology is established and widely and commercially available. Leaving the two-level system in its ground state (thermal excitation needs to be suppressed), one determines the modified resonance frequency of the oscillator $\widetilde{\omega}_\mathrm{r} = \omega_\mathrm{r} - g^2/\delta$. When the qubit is in the exited state, the dispersive shift alters the resonance frequency of the microwave resonator to $\omega_\mathrm{r} + g^2/\delta$ and hence a measurement of the resonance frequency of the microwave resonator allows to determine the state of the qubit. Typically, this measurement is performed by analyzing the phase or amplitude of the microwave resonator when exciting it with a fixed frequency.

Alternatively, when rearranging eq. 2.22 we can express the effect of the qubit-resonator

[4] Of course, an arbitrary state $|\psi\rangle$ is collapsed onto the computational basis $\{|e\rangle, |g\rangle\}$ upon measuring, but this determined eigenstate is maintained.

coupling as

$$\hat{H}_{\mathrm{JC}}/\hbar = \omega_{\mathrm{r}}\hat{a}^{\dagger}\hat{a} + \frac{1}{2}\left[\omega_{\mathrm{q}} + 2\chi\left(\hat{a}^{\dagger}\hat{a} + \frac{1}{2}\right)\right]\hat{\sigma}_{\mathrm{z}}. \tag{2.23}$$

With this form, we find the qubit to undergo an AC-Stark shift of $2\chi\langle n_{\mathrm{ph}}\rangle$ caused by the mean photon occupation $\langle n_{\mathrm{ph}}\rangle$ of the readout resonator. Additionally, the photon number statistics of the occupancy $\hat{a}^{\dagger}\hat{a}$ lead to an inhomogeneous line broadening of the qubit [23]. This effect will be used in measurements later to gain insight on the photon occupation $\langle n_{\mathrm{ph}}\rangle$ of the resonator.

2.4 Superconducting Transmon Qubits

There are many different implementations of two-level systems. Apart from natural systems like photon polarity, spin-1/2 particles, Rydberg atoms [52] or single trapped atoms [53], also artificial quantum systems can serve as two-level systems. Prominent examples are quantum dots [54] or superconducting qubits [5]. However, many artificial two-level systems are not truly two-leveled but have multiple excited states. The challenge is to decouple a single energy transition sufficiently from other excitations such that leakage into other states is minimized.
The transmon is a specific form of superconducting qubit which had proven to be successfull in a multitude of projects addressing the topics of quantum computing and simulation [12, 13] due to its long coherence times and 2D-scalability. It was introduced as a variation of a Cooper pair box in Ref. [55]. We will discuss its physics and consequences for the Jaynes-Cummings Hamiltonian as well as its control in the following. Afterwards, we will briefly introduce the mathematical description of qubit dynamics when subjected to a drive pulse. For this, the convenient Bloch sphere picture will be used. Finally, we will qualitatively discuss information loss of the qubit state in form of energy decay and dephasing without going into detail on the decoherence mechanisms. A detailed analysis of noise sources can be found in Ref. [56] and in chapter 2.4 of Ref. [57]. Measurement schemes to determine the qubit lifetime T_1 and decoherence time T_2 will be presented.

2.4.1 Physical Model of the Transmon Qubit

The transmission-line shunted plasma oscillation qubit (or transmon for short) consists of a dc-SQUID shunted by a large capacitance C_{S} to ground as shown in fig. 2.6a). A dc-SQUID is a parallel connection of two Josephson junctions. This arrangement leads to a flux-tunability of the Josephson energy E_{J}. The full transmon Hamiltonian can be shown to be [23]

$$\hat{H}_{\mathrm{T}} = 4E_{\mathrm{C}}\left(\hat{n}_{\mathrm{c}} - n_{\mathrm{c,g}}\right)^2 - E_{\mathrm{J}}\cos\left(\frac{2\pi}{\Phi_0}\hat{\Phi}\right). \tag{2.24}$$

$E_{\mathrm{C}} = e^2/2C_{\Sigma}$ is the charging energy of the total capacitance of the shunt capacitor and the Josephson junction $C_{\Sigma} = C_{\mathrm{S}} + C_{\mathrm{J}}$, Φ is the flux through the SQUID-loop (panel a) and $\Phi_0 = h/2e$ the flux quantum. We will not go into detail about the charge number operator $\hat{n}_{\mathrm{c}}$ and the offset charge $n_{\mathrm{c,g}}$, a more detailed treatment of the transmon Hamiltonian can be found in Refs. [23, 55].

To realize the Jaynes-Cummings interaction discussed in sec. 2.3, the qubit needs to be coupled

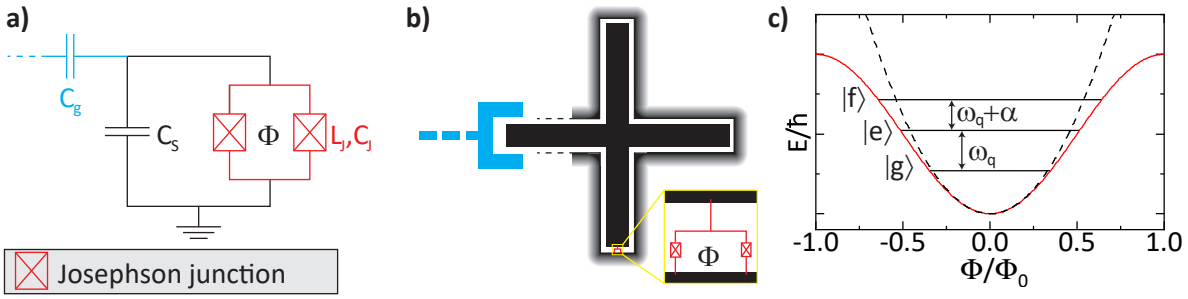

Figure 2.6: **a)** Circuit representation of a transmon qubit as a parallel circuit of two Josephson junctions (dc-SQUID) with a non-linear inductance L_J shunted by a capacitance C_S to ground. A coupling capacitance C_g allows for controlled interaction with the rest of the circuit. **b)** Schematic drawing of a transmon with a cross-shaped shunt capacitor (black). The shown transmon type is called Xmon and allows for coupling on up to three arms of the cross (blue). The dc-SQUID (red) connects the capacitor to ground. **c)** Energy scheme (red) of the transmon in dependence of the flux threading through the dc-SQUID. The non-linear inductance of the Josephson Junctions changes the energy splitting of higher excitation levels by the anharmonicity α. For transmons, α is typically negative. The dashed line is a harmonic oscillator potential for comparison.

to a harmonic oscillator. In circuit quantum electrodynamics, microwave resonators are used for this purpose. Apart from readout, the coupled resonator can also function as a storage for quantum states or as connection to other qubits. Therefore, multiple connections are useful. Panel b) shows a visual representation of a transmon in the form of a Xmon as introduced by Barends et al. in Ref. [58]. The benefit of this capacitor shape is the possibility to couple up to three different structures to it. In blue the coupling capacitor is schematically shown, its strength can be adjusted by changing its spatial dimensions and therefore the coupling capacitance C_g. This is important as different applications of a coupled resonator need different couplings. The coupling strength g is defined by [23]

$$g = \omega_\mathrm{r} \frac{C_\mathrm{g}}{C_\Sigma} \left(\frac{E_\mathrm{J}}{2E_\mathrm{C}} \right)^{1/4} \sqrt{\frac{\pi Z_\mathrm{r}}{R_\mathrm{K}}}. \tag{2.25}$$

In this expression, Z_r is the characteristic impedance of the coupled oscillator mode (usually 50Ω) and $R_\mathrm{K} = h/e^2 \approx 25.8\mathrm{k}\Omega$ the resistance quantum.
One of the arms, the lower one in the scheme, is used to short the capacitor to ground by a dc-SQUID (red).

In panel c), the potential of eq. 2.24 is shown as a solid line. The dashed line is the potential of an equivalent LC-resonator. For small flux values Φ, the transmon potential is well-described by the harmonic oscillator. However, for increasing flux the potentials diverge, leading to non-equidistant energy levels in the transmon case. The second excited state $|f\rangle$ is shifted downwards by the so-called anharmonicity α of the transmon. This is a direct consequence of the non-linearity of the Josephson inductance L_J, making the transmon a non-linear harmonic oscillator [23]. One finds that $\alpha = -E_\mathrm{C}$ [55], suggesting a maximization of the charging energy to separate the

transition frequencies as much as possible. However, the transmon would then be more susceptible to charge noise which decreases coherence times. Koch et. al [55] noticed that this susceptance decreases *exponentially* when increasing the ratio E_J/E_C while the anharmonicity decreases only *polynomially*. Therefore, a typical trade-off value is a ratio of $E_J/E_C \sim 10^2$ to keep a feasible anharmonicity but decouple the transmon sufficiently from charge noise on the chip.

The flux-tunability of the Josephson inductance additionally allows for a change of the qubit frequency (defined as the transition frequency between $|g\rangle$ and $|e\rangle$) via [55]

$$\omega_q(\Phi) = \omega_{q,0}\sqrt{\left|\cos\left(\pi\frac{\Phi}{\Phi_0}\right)\right|}. \tag{2.26}$$

This can be used to tune the transmon frequency coupled to a harmonic oscillator from the resonant to the dispersive regime and explore the Jaynes-Cummings physics discussed in sec. 2.3. Due to its nature of being not a true two-level system, the transmon experiences a more complex dispersive shift χ where also α needs to be taken into account [23]

$$\chi = \frac{g^2}{\delta}\frac{\alpha}{\delta+\alpha}. \tag{2.27}$$

Note, that χ is now negative for $\delta > 0$ since $\alpha < 0$ for transmons.

2.4.2 Driven Qubit Dynamics

For any two-level system, we can describe a *pure* state by a superposition of the energy eigenstates $|g\rangle$ and $|e\rangle$ as

$$|\psi(t)\rangle = a_e(t)\,|e\rangle + a_g(t)\,|g\rangle\,. \tag{2.28}$$

$a_e(t)$ and $a_g(t)$ are the (time-dependent) amplitude coefficients and fulfill $a_e(t)^2 + a_g(t)^2 = 1$ for all times which leads to $\langle\psi|\psi\rangle = 1$.

Transitioning to spherical coordinates, the state of a qubit can be represented by a vector on the Bloch sphere as shown in fig. 2.7a). It is a sphere of radius one centered around the origin of a right-handed coordinate system. Points on the sphere are described by a Bloch vector $\vec{r} = (r\sin\theta\cos\phi, r\sin\theta\sin\phi, r\cos\theta)$ with $0 \le \theta \le \pi$ and $0 \le \phi < 2\pi$ such that they are enclosed by the qubit state vector and the z- and x-axis respectively. Any vector pointing to the surface ($r = 1$) describes a *pure* state while vectors with a radius $r < 1$ describe *mixed* states. In the absence of decoherence, pure states will remain pure under unitary transformations [48].
If we chose the computational basis to be the z-axis, the excited state $|e\rangle$ is defined to be at the intersection of the sphere with the positive z-axis while the ground state $|g\rangle$ is at the intersection with the negative z-axis. This leads to the qubit Hamiltonian as introduced in eq. 2.15. For an arbitrary pure state we now find [49]

$$|\psi\rangle = \cos\left(\frac{\theta}{2}\right)|e\rangle + e^{i\phi}\sin\left(\frac{\theta}{2}\right)|g\rangle\,. \tag{2.29}$$

In order to change the qubit state, a coherent drive field at frequency ω_d with length t can be

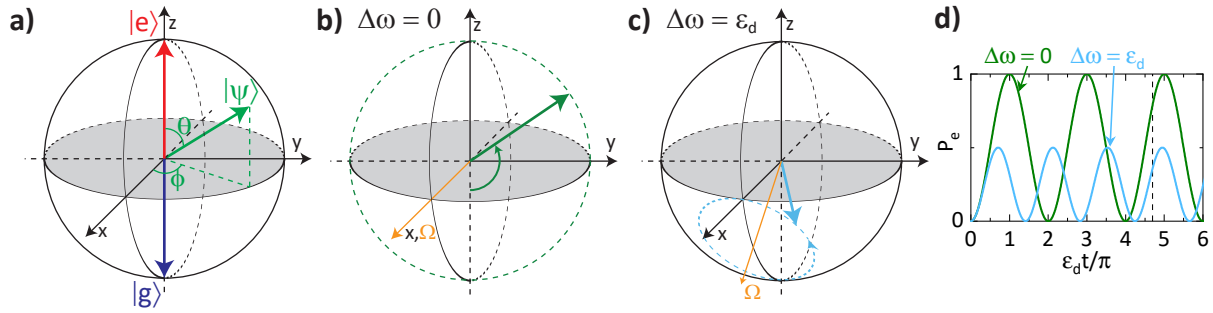

Figure 2.7: **a)** Bloch sphere representation of the qubit state. The orthogonal energy eigenstates $|e\rangle$ and $|g\rangle$ span the z-axis. Any pure qubit state can be expressed as a superposition of these eigenstates with two angles $\phi \in]-\pi, \pi]$ (measured from the x-axis) and $\theta \in [0, \pi]$ (measured from the z-axis). **b)** and **c)** Qubit state dynamics on the Bloch sphere for resonant drive. Starting from $|g\rangle$, the qubit rotates around an axis $\vec{\Omega}$. The qubit state rotates along the plane normal to the rotation direction that intersects the initial state, indicated by colored dashed circles. For resonant qubit drive (b)), the rotation axis lies in the equatorial plane, hence the qubit rotates along the full sphere circumference including the state $|e\rangle$. For non-resonant drive (c)), the rotation axis has a finite z-value. The qubit rotation is constrained to a smaller circle on the Bloch sphere. **d)** Time-dependence of the excited state population probability P_e. For resonant drive (green), the Rabi frequency Ω_R equals the drive amplitude ϵ_d and $P_\mathrm{e} = 1$ for $\epsilon_\mathrm{d} t = \pi$. For non-resonant drive (blue), the maximal amplitude of P_e is $\epsilon_\mathrm{d}^2/\Omega_\mathrm{R}^2$, so the qubit cannot purely populate the excited state. The oscillation frequency is Ω_R, hence detuning leads to faster oscillations.

applied to induce rotations around arbitrary axes. Applying a drive field of form

$$E = \frac{\epsilon_\mathrm{d}}{2}\left(e^{i\omega_\mathrm{d} t} + e^{-i\omega_\mathrm{d} t}\right), \tag{2.30}$$

with amplitude ϵ_d [50] leads to a total Hamiltonian[5]

$$\hat{H}_\mathrm{d,q}/\hbar = \frac{\omega_\mathrm{q}}{2}\hat{\sigma}_\mathrm{z} + \frac{\epsilon_\mathrm{d}}{2}\left(e^{-i\omega_\mathrm{d} t} + e^{i\omega_\mathrm{d} t}\right)\left(\hat{\sigma}_- + \hat{\sigma}_+\right). \tag{2.31}$$

This Hamiltonian is time-dependent and does not allow for a simple solution of the Schroedinger equation. However, switching to a rotating frame and neglecting any contributions with very fast frequencies (rotating wave approximation [59]), we find a stationary Hamiltonian $\tilde{H}$ that describes the same dynamics (see appendix A.1 for derivation)

$$\widetilde{H}_\mathrm{d,q}/\hbar = \frac{1}{2}\left(-\Delta\omega\hat{\sigma}_\mathrm{z} + \epsilon_\mathrm{d}\hat{\sigma}_\mathrm{x}\right). \tag{2.32}$$

Here, we introduce the detuning of the drive pulse $\Delta\omega = \omega_\mathrm{d} - \omega_\mathrm{q}$. The Hamiltonian in the rotating frame can be diagonalized easily and leads to the solution of the Schroedinger equation

$$\left|\widetilde{\psi}(t)\right\rangle = \cos\left(\frac{\theta}{2}\right)e^{i\Omega_\mathrm{R} t/2}\left|\widetilde{\psi}_-\right\rangle + \sin\left(\frac{\theta}{2}\right)e^{-i\Omega_\mathrm{R} t/2}\left|\widetilde{\psi}_+\right\rangle. \tag{2.33}$$

[5] We choose $\epsilon_\mathrm{d} \in \mathbb{R}$ for the sake of simplicity. A treatment with a complex amplitude would follow the same path.

In this expression, we introduced $\Omega_\mathrm{R} = \sqrt{\epsilon_\mathrm{d}^2 + \Delta\omega^2}$ as the Rabi frequency as well as the new eigenstates of the diagonalized Hamiltonian in the rotating wave approximation

$$\left|\widetilde{\psi}_+\right\rangle = \cos\left(\frac{\theta}{2}\right)|e\rangle + \sin\left(\frac{\theta}{2}\right)|g\rangle\,, \tag{2.34}$$

$$\left|\widetilde{\psi}_-\right\rangle = -\sin\left(\frac{\theta}{2}\right)|e\rangle + \cos\left(\frac{\theta}{2}\right)|g\rangle\,. \tag{2.35}$$

Ultimately, the probability to find the qubit in the excited state $P_\mathrm{e}(t) = \left|\left\langle e\middle|\widetilde{\psi}(t)\right\rangle\right|^2$ is given by

$$P_\mathrm{e}(t) = \frac{\epsilon_\mathrm{d}^2}{\Omega_\mathrm{R}^2}\sin^2\left(\frac{\Omega_\mathrm{R}t}{2}\right). \tag{2.36}$$

The amplitude of the oscillating population probability of a driven qubit is governed by the detuning $\Delta\omega = \omega_\mathrm{d} - \omega_\mathrm{q}$ of the drive pulse. For zero detuning, the Rabi frequency is given by the amplitude of the driving field $\Omega_\mathrm{R} = \epsilon_\mathrm{d}$. Therefore, the probability of finding the qubit in the excited state $|e\rangle$ alternates periodically between 0 and 1. In general, the dynamics of the qubit state vector $\vec{r}$ on the Bloch sphere is described by the Bloch equations [60] (see appendix A.1 for derivation)

$$\frac{\mathrm{d}}{\mathrm{d}t}\vec{r} = \vec{\Omega} \times \vec{r}, \tag{2.37}$$

with the rotation axis vector $\vec{\Omega} = (\epsilon_\mathrm{d}, 0, -\Delta\omega)$. As initial state at $t = 0$, we assume the ground state g. This leads to a trajectory plane of the qubit state vector that is orthogonal to $\vec{\Omega}$ and contains the initial state $|g\rangle$ (dashed circles in fig. 2.7a) and b)). Consequently, the qubit state vector $|e\rangle$ can be reached if and only if the detuning is zero, i.e. $\Delta\omega = 0$. For any finite detuning, there is always a non-zero probability of finding the qubit in the ground state.

The corresponding dynamics from eq. 2.37 are schematically shown in panel b) of fig. 2.7. The rotation axis $\vec{\Omega}$ (orange) of the state vector lies in the horizontal plane of the Bloch sphere along the x-axis. The state vector therefore rotates in a plane spanned by the z- and y-axis, containing both basis state vectors $|e\rangle$ and $|g\rangle$ from fig. 2.7a).
For non-zero detuning, there is no point in time where the qubit fully occupies $|e\rangle$. This is due to $\Omega_\mathrm{R} > \epsilon_\mathrm{d}$ for $\Delta\omega \neq 0$ in eq. 2.36. The rotation axis now has a finite z-contribution [61] which limits the state vector (blue) in its oscillations along z as depicted in fig. 2.7c). The shown case is for $\Delta\omega = \epsilon_\mathrm{d}$ where the maximum probability to find the qubit in the excited state is $P_\mathrm{e} = 1/2$ when occupying the state $(|e\rangle \pm i\,|g\rangle)/\sqrt{2}$.
Panel d) of fig. 2.7 shows the corresponding time evolution of P_e for the cases b) (green) and c) (blue). Additionally to the reduced amplitude of the oscillation, the detuned drive leads to a faster oscillation compared to a resonant drive since $\Omega_\mathrm{R} > \epsilon_\mathrm{d}$. We can define two important pulse lengths: The $\pi/2$-pulse rotates the qubit state around 90° on the Bloch sphere, bringing it from $|g\rangle$ or $|e\rangle$ to the equatorial plane or vice versa. The pulse has to fulfill $\Omega_\mathrm{R}\tau_{\pi/2} = \pi/2$. The π-pulse, however, inverts the qubit state by rotating it around 180°. It has a pulse length of $\Omega_\mathrm{R}\tau_\pi = \pi$ and has to be resonant, $\Delta\omega = 0$. Otherwise, a complete inversion of the population can not be achieved as the oscillation trajectory plane would not include the orthogonal state on the Bloch sphere (see fig. 2.7a) and b)).

2.4.3 Qubit Readout

In order to determine the qubit state, we use non-demolition measurements via a readout resonator. The qubit-resonator system is operated in the dispersive regime as discussed in sec. 2.3.3. Due to the finite coupling g, the qubit state alters the resonator frequency according to eq. 2.22 and fig. 2.5c). Additionally, the operation in the dispersive regime allows a distinct excitation of the qubit or resonator respectively as their resonance frequencies are far detuned, i.e. $|\omega_\mathrm{q} - \omega_\mathrm{r}| \gg 0$. Therefore, two different microwave pulses are used for the qubit excitation and readout via the resonator: a drive frequency $\omega_\mathrm{d} \approx \omega_\mathrm{q}$ and a resonator probe frequency $\omega_\mathrm{p} = \omega_\mathrm{r}$ as shown in fig. 2.8a). As discussed in the section for qubit measurement sequences, the qubit is driven off-resonant for some measurements. The resonator is always probed on resonance, deviations in the resonator response give knowledge on the qubit state via the dispersive shift.

2.4.4 Qubit Decay and Dephasing

A qubit will decay to its ground state $|g\rangle$ on a characteristic timescale T_1 as indicated in 2.8b) due to interaction with the environment [23]. On the other hand, the phase information of a qubit is lost on a timescale T_ϕ (see fig. 2.8c)) without a change in the energy, i.e. the z-component of the Bloch vector stays constant. These qubit life- and dephasing times limit the duration in which the qubit can be coherently manipulated. Since pure qubit dephasing, i.e. the loss of phase information ϕ loss of the energy information θ, cannot be observed as qubit energy decay is always present, both decay mechanisms are combined in the decoherence time [23]

$$\frac{1}{T_2} = \frac{1}{T_\phi} + \frac{1}{2T_1}. \tag{2.38}$$

This is the characteristic time scale on which information about the qubit state is lost. Longer and more complex drive schemes therefore require high coherence times. Since the qubit lifetime and dephasing time add up reciprocally, both have to be considerably long. Presently, long coherence times for superconducting aluminium transmon qubits are on the order of 100 µs [62, 63]. Compared to a π-pulse duration on the order of 10 ns, this allows for up to 10^4 coherent single qubit gates such as π- or $\pi/2$-pulses before the qubit state is lost.

In the following, we introduce measurement sequences that give insight on the qubit lifetime T_1 and decoherence time T_2. These measurement schemes require knowledge of the π-pulse length τ_π. To determine this pulse length, typically a Rabi measurement is conducted using the pulse scheme as shown in fig. 2.8d). The qubit is excited on resonance for τ_d (red) to induce a rotation in the Bloch sphere as discussed in sec. 2.4.2. Immediately after the drive, the qubit state is read out (blue), e.g. by using a readout resonator coupled to the qubit operating in the dispersive regime and measuring the resonator amplitude or phase response as introduced in sec. 2.3.3. The drive duration, for which the signal corresponding to the excited state $|e\rangle$ is maximal, is the π-pulse length.

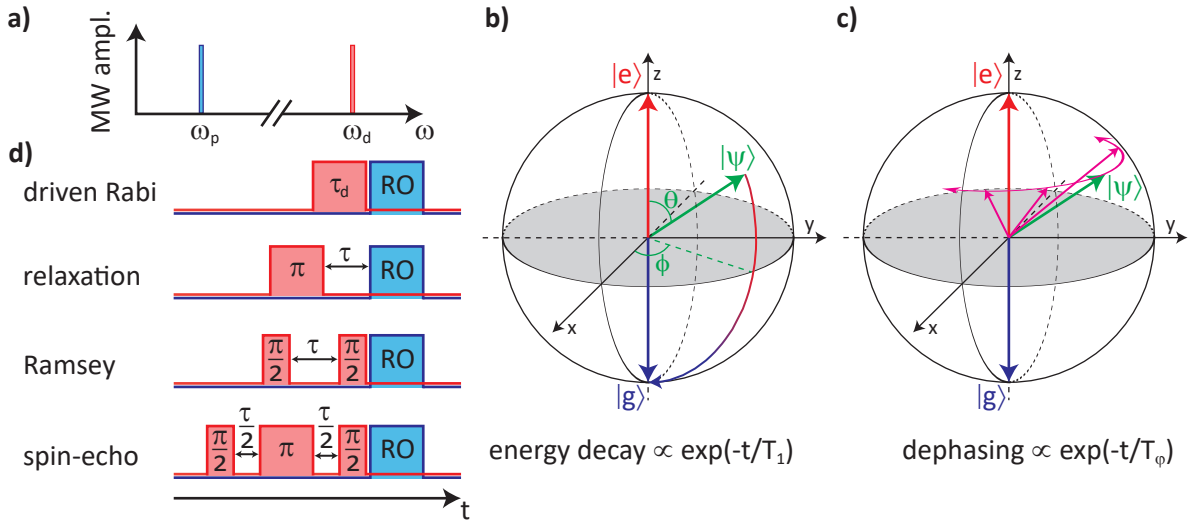

Figure 2.8: **a)** Microwave frequencies used for qubit drive (ω_d) and readout resonator probing (ω_p). Typically, the qubit is driven close to its resonance ($\omega_\mathrm{d} \approx \omega_\mathrm{q}$) and the resonator is probed with its resonance frequency ($\omega_\mathrm{p} = \omega_\mathrm{r}$). In the dispersive regime, the qubit and resonator frequencies are far detuned, such that both circuit elements can be individually addressed with their respective microwave pulses. **b)** Energy decay (gradient arrow) of an arbitrary qubit state $|\psi\rangle$ to the ground state $|g\rangle$ on a timescale T_1 due to interaction with the environment. The energy decay implies a loss of phase information as the ground state has no phase. **c)** Pure dephasing (magenta arrows) of a qubit state on a timescale T_ϕ. For pure dephasing, no energy is transferred. As energy decay is always present, pure dephasing cannot be observed directly but only in combination with energy relaxation. **d)** Pulse schemes used to determine the qubit π-pulse duration (driven Rabi), lifetime T_1 (relaxation) and decoherence time T_2 (Ramsey&spin-echo). A detailed description of the pulse schemes is given in the main text. The red pulse shape corresponds to the resonant qubit drive pulse with a variable length τ_d or fixed π- and $\pi/2$-pulse lengths, conveniently labeled as π and $\pi/2$ for better readability. The blue pulse shape schematically shows the dispersive readout at the resonator frequency as described in sec. 2.3.3. Schematic pulse lengths are not to scale.

2.4.4.1 Relaxation Measurement

The relaxation (or inversion recovery) measurement consists of a π-pulse followed by a waiting time τ and readout of the qubit state (see fig. 2.8d)). During the waiting time, the qubit can spontaneously collapse to the ground state due to interaction with the environment [23]. The probability of measuring the excited qubit state P_e decays exponentially with time, such that we expect

$$P_\mathrm{e}(t) = \exp(-\tau/T_1). \tag{2.39}$$

The characteristic timescale for the decay T_1 is called qubit lifetime and takes typical values of 10 to 100µs for transmon qubits based on aluminium [62].

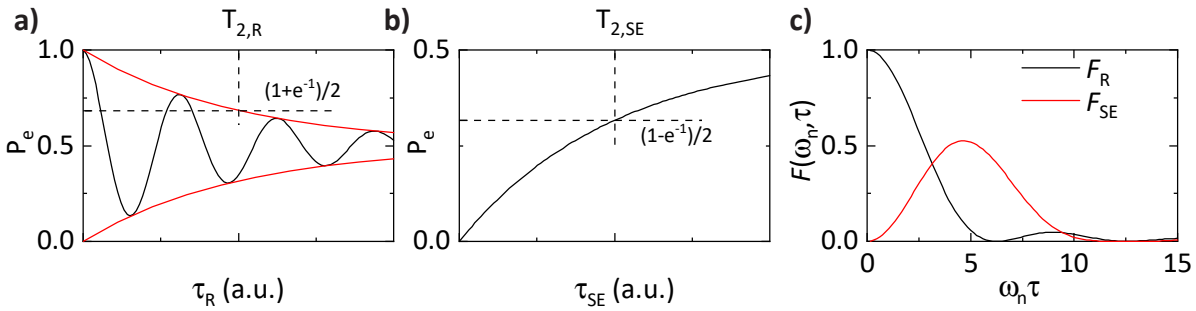

Figure 2.9: **a)** Qubit population P_e in dependence of the wait time τ_R for a Ramsey measurement. For off-resonant drive, the population oscillates with $\Delta\omega$ (black). On a timescale of $T_{2,\mathrm{R}}$, the qubit coherence is lost and constrains P_e, an envelope is shown in red. For $\tau_\mathrm{R} \to \infty$ the excitation probability is $P_\mathrm{e} = 0.5$. **b)** Spin-echo measurement conducted on resonance. The total qubit rotation for $\tau_\mathrm{SE} = 0$ is 2π such that the qubit is in the ground state after the sequence. Longer wait times lead to a non-zero probability of finding the qubit in the excited state. The probability increases to $P_\mathrm{e} = 0.5$ on a timescale of $T_{2,\mathrm{SE}}$. **c)** Filter functions F of Ramsey and spin-echo sequences depending on the noise frequency ω_n and wait time τ. The filter function determines the susceptibility of each sequence to noise. Ramsey measurements filter high-frequency noise, spin-echo measurements low-frequency noise. Pulse sequences can be found in fig. 2.8d).

2.4.4.2 Ramsey Measurement

Apart from excitation decay, dephasing plays an important role in the coherence of a qubit. Due to interaction with the environment, the phase information ϕ can be lost on a time scale of T_ϕ due to phase perturbations from various noise sources. However, one cannot measure T_ϕ directly, since energy decay will always be present. Therefore, different schemes are used to estimate the combined decay and dephasing process on a timescale T_2 following eq. 2.38. Historically, the first scheme performed on qubits (in this case spin-1/2 particles) was the Ramsey sequence [64] shown in fig. 2.8d). A $\pi/2$-pulse brings the qubit in an equal superposition of $|e\rangle$ and $|g\rangle$. After a waiting time τ, a second $\pi/2$-pulse is applied before the qubit state is measured. During the free evolution time, the qubit will precess around the z-axis with the detuning $\Delta\omega = \omega_\mathrm{d} - \omega_\mathrm{q}$ between the drive and qubit eigenfrequency. In the absence of decoherence and for zero detuning $\Delta\omega = 0$, the qubit state vector will remain stationary in the rotating frame picture, such that the second $\pi/2$-pulse will excite the qubit to $|e\rangle$. In the case of finite detuning $\Delta\omega \neq 0$, the qubit has rotated 180° around the z-axis (Lamor precession in the rotating frame) when $\Delta\omega\tau_\mathrm{R} = \pi$. Then, the second $\pi/2$-half pulse would rotate the qubit to $|g\rangle$ again.
However, interaction with a noise bath leads to decoherence during the waiting time τ_R such that the state vector will dephase and decay. Only accounting for dephasing at the moment, the qubit state vector will spread in the xy-plane (pink arrows in fig. 2.8c)). Therefore, there is a finite probability of finding the qubit in state $|g\rangle$ after the sequence for zero detuning. Analogously for the case of finite detuning, the probability of finding the qubit in state $|e\rangle$ is non-zero even for the condition $\Delta\omega\tau_\mathrm{r} = \pi$. The latter case shown in fig. 2.9a). The probability of finding the qubit in the excited state oscillates with a detuning $\Delta\omega$, a minimum of P_e is therefore found when

$\tau_R = \pi/\Delta\omega$. If $\tau_R = 0$, the total applied pulse is a π-pulse such that we find $P_e = 1$. For $\tau \gg T_1$, the qubit would relax back to the ground state due to energy decay, such that $P_e = 0.5$ after the second $\pi/2$-pulse. This is indicated by the red envelope approaching 0.5 as $\tau_R \to \infty$. Therefore, the Ramsey decoherence time $T_{2,R}$ is defined as the wait time τ_R after which P_e has decayed to $(1 + e^{-1})/2$.
It is to be noted that we assume an exponential time dependence of the qubit coherence following chapter 4.4 of Ref. [57]. However, in reality the process strongly depends on the noise spectral density acting on the qubit. Different source of noise change the decoherence behavior quantitatively. A detailed discussion of noise channels can be found in Ref. [56] and in chapter 2.4 of Ref. [57].

2.4.4.3 Spin-Echo Measurement

A different measurement protocol to determine the coherence time T_2 is a spin-echo sequence [65] (see. fig. 2.8d)). For this protocol, a $\pi/2$ pulse excites the qubit into the horizontal plane of the Bloch sphere before the qubit evolves for a time $\tau_{SE}/2$. This measurement is performed with resonant $\pi/2$ pulses, such that there will be no Lamor precession of the state vector in the rotating frame during the waiting time, but only dephasing. A π-pulse inverts the population of the qubit. This also inverts the dephasing effect as long as the noise source is dominated by low frequency components which remain approximately constant over the course of the pulse sequence [57]. After a second wait time of length $\tau_{SE}/2$, a $\pi/2$-pulse is applied before determining the qubit state. As for the Ramsey measurements, we expect $P_e = 0.5$ for $\tau \to \infty$. However, for $\tau_{SE} = 0$, the total applied pulse is a 2π-pulse, we therefore expect the qubit to be in state $|g\rangle$, i.e. $P_e = 0$. An exemplary time trace of the qubit population probability is shown in fig. 2.9b).

The critical difference between the Ramsey and spin-echo protocol becomes obvious in fig. 2.9c). Here, the filter functions F_R and F_{SE} for both sequences are shown as a function of the noise frequency ω_n and the wait time durations τ_R and τ_{SE}. The function formulas are given by [66]

$$F_R(\omega_n,\tau_R) = \frac{\sin^2(\omega_n\tau_R/2)}{(\omega_n\tau_R)^2}, \tag{2.40}$$

$$F_{SE}(\omega_n,\tau_{SE}) = \frac{\sin^4(\omega_n\tau_{SE}/2)}{(\omega_n\tau_{SE})^2}. \tag{2.41}$$

The filter function describes the susceptibility of the measurement to noise at frequency ω_n. Ramsey measurements are strongly influenced by low-frequency noise with $\omega \to 0$. For higher frequencies or longer wait times the phase added by the noise source averages to zero, so the filter function approaches zero.
A spin-echo sequence however filters slowly changing noise due to the inversion of the qubit state after half of the wait time. This leads to a compensation of the acquired phases during both waiting times and therefore no effective influence of the constant noise source [56]. If the noise field fluctuates on the timescale of the wait time τ_{SE} such that $\omega_n\tau_{SE} \approx 2\pi$, the filtering effect is lost. The spin-echo sequence therefore is mostly effective when dealing with $1/f$-noise while the

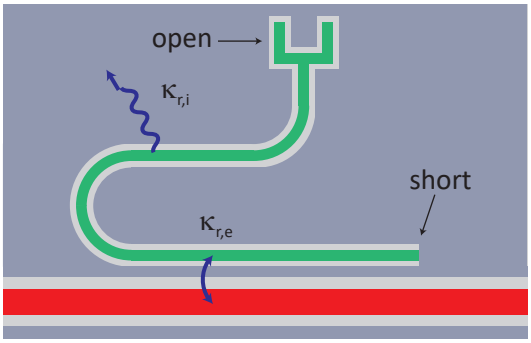

Figure 2.10: A $\lambda/4$ coplanar waveguide (CPW) resonator (green) is coupled to a CPW transmission line (red) via the external coupling rate $\kappa_{\mathrm{r,e}}$. The standing wave condition is imposed on an electromagnetic wave by the electrical open- and short-condition at the ends of the resonator. The resonator loses energy to the environment with an internal loss rate $\kappa_{\mathrm{r,i}}$. For readout resonators, the overcoupled regime $\kappa_{\mathrm{r,e}} > \kappa_{\mathrm{r,i}}$ is desirable to increase the interaction of the resonator with the measurement setup via the transmission line.

Ramsey sequence filters high-frequency noise. Hence, a comparison of both coherence times $T_{2,\mathrm{R}}$ and $T_{2,\mathrm{SE}}$ can provide valuable insight into the frequency of the noise sources dominating the decoherence of an investigated qubit.

2.5 Superconducting Microwave Resonators

After the discussion of transmon qubits as artificial two-level systems, we now focus on the harmonic oscillators. When moving from cavity quantum electrodynamics to circuit quantum electrodynamics, coplanar waveguide (CPW) resonators typically take the role of the harmonic oscillator [22]. We will only qualitatively introduce these microwave resonators, further reading with more details on the physics can be found in Refs. [57, 67].

Coplanar waveguide resonators (CPWR) are defined by a transmission line separated by a gap from two ground planes as shown in fig. 2.10. Here, a $\lambda/4$-resonator (green) coupled to a CPW transmission line (red) is shown, which is the 2D equivalent of a coaxial cable. For a $\lambda/4$-resonator, one end of the signal line is shorted to ground (gray) while the other end has an electrical open condition. Therefore, a standing wave can form if $(2n+1)\lambda/4 = l,\ n \in \mathbb{N}$ with λ being the wavelength of the electromagnetic wave. A resonator with open conditions at both ends of the signal line is similarly defined as a $\lambda/2$-resonator with a standing wave condition of $n\lambda/2 = l,\ n \in \mathbb{N}$.

2.5.1 Quality Factor and Loss Rates

An important figure of merit of a resonator is its quality factor Q. It is a measure for the average energy lost per cycle [67]

$$Q = \omega_{\mathrm{r}} \frac{\text{average energy stored}}{\text{energy loss/second}}. \tag{2.42}$$

With the introduction of a loss rate (or equivalently linewidth) κ_{r}, the quality factor is commonly defined as

$$Q = \frac{\omega_{\mathrm{r}}}{\kappa_{\mathrm{r}}}. \tag{2.43}$$

High quality factors are achieved when the loss rate is low, i.e. the resonator stores energy for a long time compared to its eigenfrequency. However, one has to distinguish between intended loss rates, e.g. coupling to external circuit elements denoted as $\kappa_{\mathrm{r,e}}$, and unfavorable internal losses $\kappa_{\mathrm{r,i}}$. In our scheme (fig. 2.10), the external loss or coupling rate quantifies the energy transfer between the resonator and the transmission line while the internal loss rate is attributed to all losses to the environment. As loss rates sum up to a total linewidth $\kappa_{\mathrm{r}} = \kappa_{\mathrm{r,e}} + \kappa_{\mathrm{r,i}}$, the respective quality factors have to be added reciprocally $Q^{-1} = Q_{\mathrm{e}}^{-1} + Q_{\mathrm{i}}^{-1}$. There are different regimes depending on the dominating loss channels [67].
In the case of $\kappa_{\mathrm{r,e}} > \kappa_{\mathrm{r,i}}$, the resonator is *overcoupled* to the feedline, i.e. the main channel for energy loss is to the coupled circuit. This allows for comparably quick access to the resonator and is favorable for readout resonators.
If $\kappa_{\mathrm{r,e}} < \kappa_{\mathrm{r,i}}$, the resonator is *undercoupled* such that the internal losses dominate the quality factor. As $\kappa_{\mathrm{r,i}}$ is typically minimzed for minimal energy loss to the environment, the resonator is weakly coupled to the transmission line in this case. A low overall linewidth κ_{r} and high quality factor Q are important for storage resonators with long decay times $\propto \kappa_{\mathrm{r}}^{-1}$.

2.5.2 Mean Photon Number

As any driven harmonic oscillator, a CPWR follows a Lorentzian response close to resonance (ch. 4.2.5 of Ref. [68]). This also holds for the mean photon number $\langle n_{\mathrm{ph}} \rangle$ occupying the resonator [69]

$$\langle n_{\mathrm{ph}} \rangle = \frac{2P_{\mathrm{appl}}}{\hbar\omega\left[\kappa_{\mathrm{r}}^2 + 4(\omega - \omega_{\mathrm{r}})^2\right]} \Lambda \kappa_{\mathrm{r,e}}. \tag{2.44}$$

Here, P_{appl} is the power microwave with frequency ω at the output of the microwave signal source, Λ the attenuation of the measurement setup to the resonator and $\hbar$ the reduced Planck constant. With eq. 2.44, the total effective attentuation of the setup, including cable losses, can be calibrated. The photon number occupation of a resonator is non-trivial, however it is an important quantity for experiments in the Jaynes-Cummings regime. If $\langle n_{\mathrm{ph}} \rangle$ exceeds a critical value given by [69]

$$\langle n_{\mathrm{crit}} \rangle = \frac{\delta^2}{4g^2}, \tag{2.45}$$

the dispersive regime discussed in sec. 2.3.3 becomes invalid and the measurements can no longer be considered as *non-demolition*. In the equation, δ denotes the detuning and g the coupling strength between resonator and qubit. Therefore, a power calibration needs to be conducted to probe the resonator within the dispersive regime.

2.6 Surface Acoustic Wave Resonators

For the transition from circuit quantum electrodynamics to quantum acoustodynamics, an additional harmonic oscillator is introduced: the surface acoustic wave resonator (SAWR). A SAWR consists of at least one interdigitated transducer (IDT) and two reflectors [18]. The case for a 1-port SAWR is shown in fig. 2.11a). The IDT injects/absorbs SAWs in the cavity formed by the two reflectors. The SAWs propagte freely along the IDT-reflector spacing d_{s} and

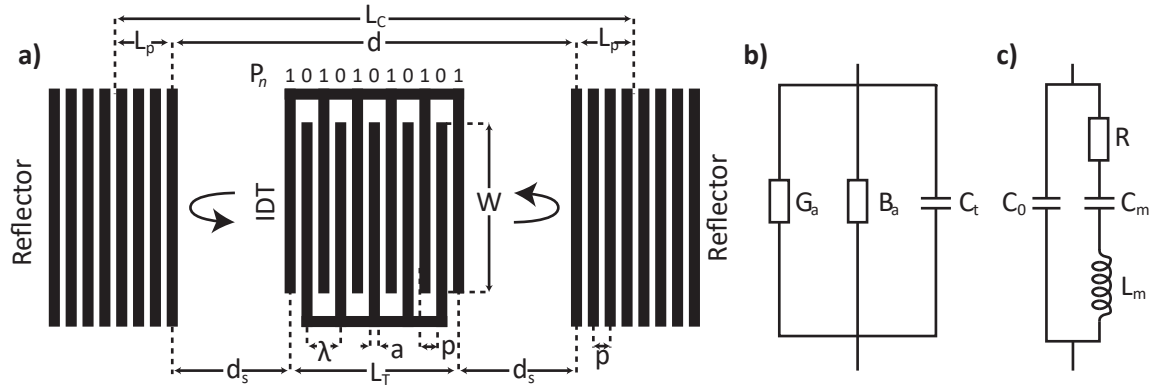

Figure 2.11: **a)** Scheme of a 1-port surface acoustice wave resonator (SAWR). All design lengths d_s, L_T and d use the center of the involved element's first electrode as reference points as shown in the scheme. **b)** Equivalent circuit model of an interdigitated transducer consisting of an acoustic conductance and suscpetance G_a and B_a as well as a geometric capacitance C_t induced by the transducer fingers. **c)** Butterworth-van Dyke equivalent circuit of a 1-port SAWR with a geometric capacitance in the left branch and a RLC-circuit in the right branch covering the influence of SAWs.

are effectively confined to a cavity length L_C. In this section, we will introduce IDTs for the generation of SAWs and discuss their frequency response depending on the geometry. This is of major importance to cover a large frequency range of creatable SAWs. Furthermore, we will introduce gratings as Bragg reflectors for SAWs and derive their behavior. Finally, with these elements, we will be ready to discuss the expected response of a 1-port SAWR when probing with microwaves.

2.6.1 Interdigitated Transducers

The most common way to create SAWs are interdigitated transducers (IDTs) on a piezoelectric substrate. There are different implementations of IDTs. The "single-electrode" transducer as shown in fig. 2.11a) consists of metal fingers alternately connected to signal and ground of an electrical microwave line. This defines the polarity pattern P_n = 1,0,1,0,1..., where "1" denotes a connection of the electrode to the signal line and "0" to ground. An important design parameter is the metallization ratio $\eta = a/p$ with a being the width of the metal strips and p the pitch of the strips. A metallization ratio of $\eta = 0.5$ simplifies the analysis of the IDT's behavior. More complex IDT designs exist, for example a double-electrode IDT with a polarity pattern P_n = 1,1,0,0,1,1,0,0,.... Those show different response functions and can offer advantages like lower reflection or improved directionality [18]. However, since the fundamental wavelength is geometrically constrained by the repetition length of the periodic finger arrangement, single-electrode transducer allow for the smallest wavelengths at a given structure size, which might be limited by fabrication constraints. The fundamental wavelength of the emitted SAW of such a single-eletrode transducer λ_IDT with a 50% metallization ratio is given by

$$\lambda_\mathrm{IDT} = 4a. \tag{2.46}$$

For a single-electrode IDT with a $\eta = 50\%$, the acoustic potential at a fixed position, e.g. immediately outside of the transducer, is given by [18, 70]

$$\Phi_\mathrm{a}(\omega) = VE(\eta, \omega)A(\omega) \tag{2.47}$$

where V is the applied voltage and $E(\eta, \omega)$ the so-called element-factor describing the response of a single, delta-like transducer electrode. N_t is the number of fingers in the transducer, P_n either 0 (finger connected to ground) or 1(finger connected to signal), $k = 2\pi/\lambda = \omega/v_\mathrm{p}$ the wavenumber, v_p the phase velocity of the SAW and x_n the position of the finger with respect to the reference port. The array factor $A(\omega)$ accounts for the geometric transduction properties of the IDT. Introducing the number of fingers N_t and analogously the amount of finger pairs $N_\mathrm{p} = \lfloor N_\mathrm{t}/2 \rfloor$ as well as the pitch $p = 2a$ between the array factor $A(\omega)$ is defined as

$$A(\omega) = \sum_{n=1}^{N_\mathrm{t}} P_n e^{-ikx_n} = \sum_{m=1}^{N_\mathrm{p}} \left(e^{-2ikp}\right)^m = \frac{\sin(N_\mathrm{p}kp)}{\sin(kp)} e^{-ikp(N_\mathrm{p}+1)}. \tag{2.48}$$

The first transformation of the sum uses the known values of P_n. For a uniform transducer as seen in fig. 2.11a), they are 1 for odd and 0 for even electrode numbers. It is assumed that the electrodes are delta-like with $x_n = np$, therefore only summands with $x_m = (2m-1)p$ for $m \in \mathbb{N}$ and m counting signal-ground electrode pairs N_p contribute to the sum. For a resonant IDT response, the wavelength, i.e. spatial periodicity, has to equal the distance between two fingers with the same polarity which is $2p$. We now note two things:

- $kp = \frac{\omega}{v_\mathrm{p}} 2a = \omega\pi \frac{\lambda_\mathrm{c}}{2\pi v_\mathrm{p}} = \pi \frac{\omega}{\omega_\mathrm{c}}$ with $\omega_\mathrm{c} = k_\mathrm{c} v_\mathrm{p}$ and $k_\mathrm{c} = \frac{2\pi}{\lambda_\mathrm{c}} = \frac{2\pi}{4a}$,
- $|\sin(x + n\pi)| = |\sin(x)|$ with $n \in \mathbb{N}$.

Introducing $\theta = kp - \pi = \pi\left(\frac{\omega}{\omega_\mathrm{c}} - 1\right)$, we can now make use of the small angle approximation $\sin(x) \approx x$ for $x \approx 0$. Taking the absolute value of $A(\omega)$, we find for frequencies close to the center frequency of the IDT ω_c, i.e. $\theta \approx 0$ the array factor to be approximated by

$$\begin{aligned} |A(\omega)| &= \left|\frac{\sin\left(N_\mathrm{p}(\theta+\pi)\right)}{\sin(\theta+\pi)}\right| = \left|\frac{\sin\left(N_\mathrm{p}\theta\right)}{\sin\theta}\right| \approx \left|\frac{\sin(N_\mathrm{p}\theta)}{\theta}\right| \\ &= N_\mathrm{p}\left|\frac{\sin(N_\mathrm{p}\theta)}{N_\mathrm{p}\theta}\right|. \end{aligned} \tag{2.49}$$

The response of an IDT is governed by the acoustic conductance $G_\mathrm{a}(\omega)$. Close to resonance, it is given by [18]

$$G_\mathrm{a}(\omega) \approx G_\mathrm{a}(\omega_\mathrm{c}) \left(\frac{\sin(N_\mathrm{p}\theta)}{N_\mathrm{p}\theta}\right)^2 \propto A^2(\omega). \tag{2.50}$$

The acoustic conductance has multiple frequency-dependent contributions, but the array factor $A(\omega)$ usually dominates the IDT response close to resonance. The acoustic conductance on resonance $G_\mathrm{a}(\omega_\mathrm{c})$ is given by eq. 2.53. Therefore, the response of an IDT close to resonance is proportional to a sinc^2-function of the number of finger pairs and the frequency detuning. It is exemplarily shown for a center frequency of $\omega_\mathrm{c}/2\pi = 5\mathrm{GHz}$ and $N_\mathrm{p} = 5$ in fig. 2.12a). An important measure is the bandwidth of the IDT spectrum. The resonance condition is given

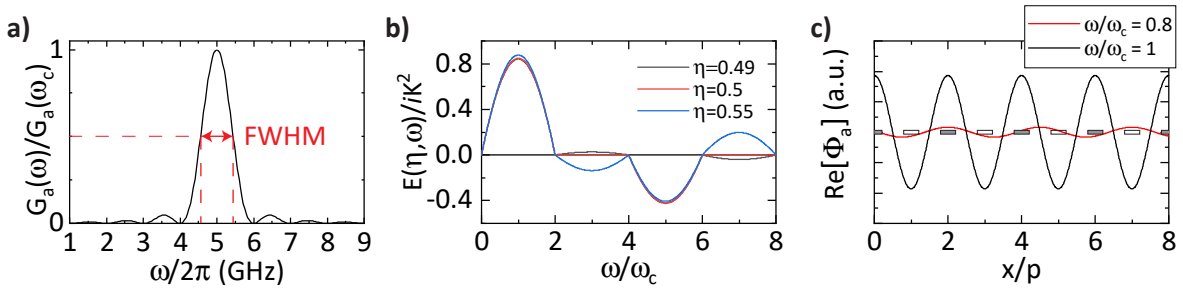

Figure 2.12: **a)** Acoustic conductance of an IDT with $f_c = \omega_c/2\pi = 5\,\mathrm{GHz}$ and $N_p = 5$. Smaller N_p lead to broader array factors and therefore a larger frequency range addressable by the IDT. **b)** Element factor $E(\eta, \omega)$ for different metallization ratios η obtained from a quasi-static approximation. The element factor vanishes for even harmonics of the fundamental IDT mode and also for the third harmonic if $\eta = 0.5$. **c)** Acoustic potential Φ_a over the range of an IDT with pitch p. The IDT electrodes are schemtically shown via rectangles, a voltage is applied to the fingers connected to signal (grey). On resonance (black), the acoustic potenial is maximal at the electrodes, allowing efficient SAW generation. Off-resonant (red), the amplitude of the potential is smaller and the periodicity of the potential does not match the IDT pitch. Therefore, SAW generation is suppressed.

by $N_p\theta = 0$, i.e. the maximum of the acoustic conductance is reached. With $\theta = kp - \pi$ and $k = \omega/v_p$ the center of the fundamental band is at $\omega_c/2\pi = v_p/4a = v_p/\lambda$. With $\mathrm{sinc}^2(Nx) = 1/2$ for $x = 1.39/N$ it follows that the acoustic conductance reaches the half maximum value at $\theta = \pi\left(\frac{\omega_{1/2}}{\omega_c} - 1\right) = 1.39$ leading to:

$$\frac{\omega_{1/2}}{\omega_c} = \frac{f_{1/2}}{f_c} = 1 + \frac{1.39}{N_p\pi}, \tag{2.51}$$

where $f = \omega/2\pi$ is the natural frequency. Thereby, the full-width at half-maximum (FWHM) ν_{IDT} of an IDT with $N_p = 5$ can be calculated as

$$\nu_{IDT} = 2\left|f_{1/2} - f_c\right| \approx 0.18 f_c. \tag{2.52}$$

For the case of $f_c = 5\,\mathrm{GHz}$ as shown in fig. 2.12a) this results in $\nu_{IDT} = 0.9\,\mathrm{GHz}$. The FWHM scales reciprocally with the number of finger pairs so that less electrodes increase the range of frequencies that the IDT can interact with from a geometrical point of view.

Additionally to excitations at the fundamental resonance frequency imposed by the IDT geometry, the acoustic conductance has maxima for higher harmonics $\omega = n\omega_c$ [18]. However, one has to discuss the element factor of a single electrode to determine whether the IDT supports higher harmonics. The element factor $E(\eta, \omega)$ is derived by a quasi-static approximation that can be found in chapter 5 of Ref. [18], the result is shown in fig. 2.12. The strongest coupling is to the fundamental mode, and all even harmonics vanish. This is due to the corresponding wavelength as for even harmonics all IDT fingers would have to be on the same electric potential. However, this would contradict the very mechanism of generating SAWs via alternating potential differences.

Interestingly, the model predicts no coupling to the third harmonic for a 50% metallization ratio $\eta = 0.5$. A Lamb's integral model however predicts some coupling [71] and third harmonics have also been measured [44]. Already slight deviations of η allow for coupling to the second mode. The fifth harmonic is more pronounced than the third. Since the element factor scales linearly with the electromechanical coupling coefficient K^2 it is beneficial to use strong piezoelectric materials for generating SAWs.
The resulting acoustic potential (eq. 2.47) is shown in fig. 2.12c) over the spatial extension of a 11-finger IDT, illustrated by boxes in the figure. The applied signal is a constant voltage on the signal electrodes (grey). On resonance (black curve), i.e. $\omega = \omega_c$, the acoustic potential has the same periodicity as the IDT and a maximal amplitude, therefore SAWs can be generated efficiently. Off-resonance however, the amplitude of the potential is smaller and the periodicity does not match the pitch p. Therefore, the generation of SAWs is suppressed.
The response of an IDT can also be derived via an equivalent circuit model as shown in fig. 2.11b). It consists of an acoustic conductance $G(\omega)$ and susceptance $B(\omega)$ as well as a geometrical capacitance of the transducer $C_t = WN_p\epsilon_\infty$. W is the overlap of signal and ground fingers and ϵ_∞ is a material parameter. Typical values for various substrates can be found in Ref. [18] in table 4.2. It can be show that close to the fundamental resonance $G_a(\omega)$ and $B_a(\omega)$ can be approximated as [26]

$$G_a(\omega) \approx G_a(\omega_c) \left(\frac{\sin(N_p\theta)}{N_p\theta} \right)^2, \tag{2.53}$$

$$B_a(\omega) \approx G_a(\omega_c) \left(\frac{\sin(2N_p\theta) - 2N_p\theta}{2(N_p\theta)^2} \right). \tag{2.54}$$

The acoustic conductance $G_a(\omega)$ can be seen as the ability to convert electrical power into mechanical waves, so the result has the same form as the model above. For the maximum acoustic conductance $G_a(\omega_c) \approx 1.3K^2N_p^2\omega_c WC_s$ holds [26, 72]. Here, C_s is an equivalent dielectric constant of the material introduced when deriving a Transmission-Line Model for SAWs in [73]. At least for LNO, this is the same value as ϵ_∞.

2.6.2 Gratings

Apart from IDTs to control the generation of SAWs, mirror-equivalents are needed to form a resonator with SAWs. The concept of Bragg reflectors will be introduced here starting with an infinitely long grating before discussing important criteria for finite gratings. The grating consists of shorted or open parallel metal strips with a pitch p or grooves in the piezoelectric substrate and can work as a reflector for SAWs. The basic idea of a grating as reflector is that each individual strip of the periodic pattern reflects a little bit of the incident wave due to a change in the mechanical environment, but the summation over all strips leads to a constructive interference of the reflected waves if the condition $p \approx n\lambda/2$ with n integer is met.

2.6.2.1 Infinitely long gratings

For the following derivation, we use the reflective array method following Ref. [18]. Here, waves are described by an effective wavenumber k_e propagating through the grating. Transmissions

(or reflections) of each single electrode strip are added up and give rise to a grating mode with wavenumber γ for which all transmitted (or reflected) waves interfere constructively. This method assumes an infinite amount of equally spaced grating electrodes $N_g \to \infty$. However in practice high reflective gratings with a total reflection coefficient of $|\Gamma| \to 1$ are the closest one can get to the theory. The method defines equaly distanced ports with pitch p between the electrodes (dashed lines in fig. 2.13a)). The amplitude A of waves traveling towards the electrode between two ports are labeled with i (incident), outgoing waves with t (transmitted). Using the reflective array method, the relation between the transmitted amplitude $A_{t,2}$ through a single electrode from port 1 to port 2, see fig. 2.13a), can be expressed in terms of the incident wave amplitudes $A_{i,1}$ and $A_{i,2}$ as [18]

$$A_{t,2} = A_{i,1} t_s \exp(-ik_e p) + A_{i,2} r_s \exp(-ik_e p). \tag{2.55}$$

$t_s \lessapprox 1$ is the transmission coefficient for an individual strip, while r_s is the corresponding reflection coefficient fulfilling $t_s^2 + r_s^2 = 1$. We make the assumption of t_s to be real, this can always be achieved by compensating any non-zero phase of t_s with a change of the effective wavenumber. This gives then rise to a change in the effective wave velocity $v_e = \omega/k_e$ in the grating. Note, that the frequency of the wave ω stays unchanged. From this ansatz one can derive the relation of the collective grating mode γ to the effective wavenumber k_e as [18]

$$\cos(\gamma p) = \frac{\cos(k_e p)}{t_s}. \tag{2.56}$$

Equivalently to the discussion above the wavenumber can be expressed in terms of frequencies

$$k_e p = \frac{\omega}{v_e} p = \pi \frac{\omega}{\omega_c},$$

where $\omega_c = \pi v_e / p$ represents the center frequency at which the grating is most efficient. Due to the different dispersion relation this does not necessarily need to coincide with the center frequency of an IDT with the same pitch. For practical purposes, this is not critical as long the bandwidth of the IDT is large enough to ensure overlap with the grating center frequency. For the discussion of eq. 2.56 it is more intuitive to stay in the spatial expression in terms of k_e and γ.

For the reflective array method, the wave is only defined at the ports. This spatial discreteness leads to Brillouin zones in the dispersion relation, equivalently to the Brillouin zones of the phonon dispersion in bulk materials (c.f. ch. 5.2 of Ref [41]). It is therefore sufficient to look at the solutions in the first Brillouin zone with $-1 < \gamma p/\pi \leq 1$. Panel b) in fig. 2.13 shows the real and imaginary part of the grating mode wavenumber γ in the first Brillouin zones as a function of the effective wavenumber of the traveling wave k_e, which is assumed to be real in the absence of losses. As $t_s \lessapprox 1$, eq. 2.56 yields $\gamma \approx k_e$ for almost all wavenumbers k_e, i.e. as long as $\cos(k_e p)/t_s \leq 1$. Therefore, the resulting mode in the grating is a travelling wave passing through the grating. Here, the solid lines and dashed lines show the same solution but with propagation in opposite directions. However if $k_e p \approx n\pi$ with $n \in \mathbb{N}$ (see right panel in fig. 2.13b)), the right-hand side of eq. 2.56 is larger than unity, leading to a purely imaginary γ. In this regime,

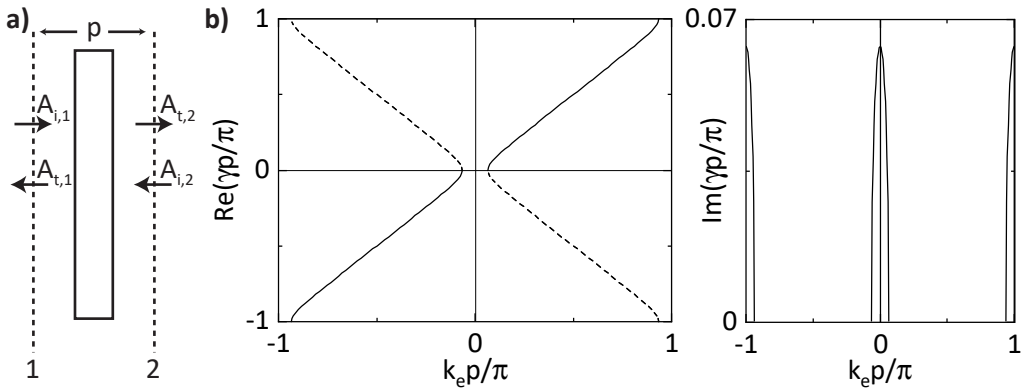

Figure 2.13: **a)** Scheme of transmission and reflection nomenclature on a single electrode. Waves are labeled as incident or transmitted. With this ansatz the waves are only defined at the ports 1 and 2. Similar to phonons in bulk materials, this discreteness in the spatial confinement leads to Brillouin zones in the dispersion relation. **b)** Dispersion relation of the grating for $t_s = 0.98$. Off resonance grating modes are very similar to free modes, close to the resonance $kp \approx n\pi$ the wavenumber in the grating is imaginary and thus the wave is attenuated and reflected. Figure b) adapted from [18].

the traveling wave is attenuated and reflected, yielding a stop band with a bandwidth Δf of [18]

$$\frac{\Delta f}{f_c} \approx \frac{2\,|r_s|}{\pi}. \tag{2.57}$$

$f_c = \omega_c/2\pi$ is the center frequency of the first stop band expressed as natural frequency. Stop bands occur for any integer multiple of ω_c. With the assumption of a constant effective velocity v_e, they all have the same width as given in eq. 2.57. The single electrode reflectivity r_s is dependent on the substrate, the metal, the electrical contact of the strips and the ratio of the strip height to the wavelength $\lambda = 2p$ of the wave in the grating.

2.6.2.2 Finite gratings

While the above description gives a nice understanding of the behavior of stop bands, we now want to briefly discuss the total reflection coefficient of a finite grating with $N_g \in \mathbb{N}$ and its expected behavior. With a P-matrix formulation (see Appendix D of Ref. [18] for details) the reflection coefficient $|\Gamma|$ can be shown to be

$$\frac{1}{|\Gamma|^2} = 1 + \left|\frac{t_s}{r_s}\right|^2 \frac{\sin^2 \gamma p}{\sin^2 N_g \gamma p}. \tag{2.58}$$

From the equation, it is obvious that the reflection coefficient cannot exceed unity. Furthermore the $\sin^2$-functions in the formula lead to an oscillating behavior. At the center of the first stop band, i.e. when $\gamma p = \pi$, the reflection coefficient is given by

$$|\Gamma| \approx \tanh(N_g\,|r_s|). \tag{2.59}$$

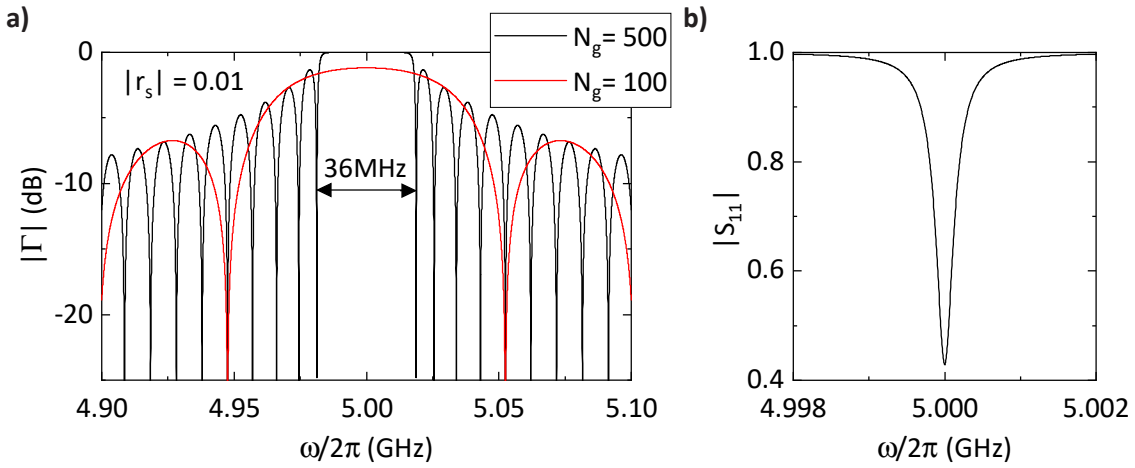

Figure 2.14: **a)** Reflection coefficient $|\Gamma|$ in dependence of frequency for a single electrode reflectivity $|r_\mathrm{s}| = 1\%$. For high reflective gratings $N_\mathrm{g}\,|r_\mathrm{s}| > 2.5$ the stop band is almost rectangular, weakly reflecting gratings show a sinc-dependence. The width of the stop band is given by eq. 2.57. **b)** Exemplary reflection coefficient amplitude of eq. 2.63 with $f_\mathrm{r} = 5\,\mathrm{GHz}$, $Q_\mathrm{e} = 5 \times 10^4$ and $Q_\mathrm{i} = 2 \times 10^4$. At resonance, the reflection coefficient is minimal since microwaves can excite SAWs occupying the Fabry-Perot resonator mode. This also leads to a phase shift in the reflection spectrum.

For $N_\mathrm{g}\,|r_\mathrm{s}| > 2.5$ more than 99% of the wave is reflected. The frequency dependence of $|\Gamma|$ in the vicinity of a center frequency $\omega_\mathrm{c}/2\pi = 5\,\mathrm{GHz}$ is shown in fig. 2.14a). $|\Gamma|$ is calculated with a single-strip reflection coefficient $|r_\mathrm{s}| = 1\%$ for a weakly reflecting ($N_\mathrm{g} = 100$) and a strongly reflecting ($N_\mathrm{g} = 500$) grating. For the high-reflectivity grating the stop band has a rectangular form with a width of 36 MHz in accordance with eq. 2.57. Outside of the stop band the reflection coefficient is highly dependent on the frequency and suppressed. The weakly reflecting grating has no stop band with a uniform reflection coefficient but a broad range of frequencies with a approximately constant $|\Gamma|$.

2.6.3 1-port SAW Resonator

2.6.3.1 SAWR as a Fabry-Perot Resonator

As opposed to CPWRs discussed in sec. 2.5 where we investigate the fundamental resonance, i.e. the wavelength λ fulfills $\lambda = 4L$ for a resonator with length L, SAWRs are operated in a regime where $\lambda \ll L_\mathrm{C}$ as shown in fig. 2.11a). Similar to optical cavities [74], a SAWR can host multiple resonances with a spacing of the free-spectral range [29]

$$\nu_\mathrm{FSR} = v_\mathrm{p}/2L_\mathrm{C}. \tag{2.60}$$

A non-trivial dispersion relation for the phase velocity v_p can lead to a frequency-dependent FSR. Furthermore, the effective cavity length L_C is a combination of the reflector-reflector spacing d

and the penetration depth L_p of the SAWs [19]

$$L_\mathrm{C} = d + 2L_\mathrm{p}. \tag{2.61}$$

This penetration depth is a consequence of the small single-strip reflectivity as this allows the SAW to penetrate the mirror before being completely reflected. In the limit of strong-reflecting grating $N_\mathrm{g}\,|r_\mathrm{s}| \gg 1$, the penetration depth can be shown to be [18]

$$L_\mathrm{p} = \frac{a}{|r_\mathrm{s}|}. \tag{2.62}$$

2.6.3.2 Electrical Response of 1-port SAWRs

The 1-port resonator can be modeled by an equivalent circuit known as the Butterworth-van Dyke circuit [18]. It is schematically shown in fig. 2.11c). The circuit consists of two branches. The right branch accounts for the motional inductance and capacitance L_m and C_m as well as a resistance R for non-unity grating reflections. The left branch is a simple capacitance C_0, which can be approximated by the transducer capacitance C_t [18]. From the Butterworth-van Dyke equivalent, the scattering parameter S_{11} can be calculated in terms of internal and external quality factors Q_e and Q_i close to a resonance f_r [19]

$$S_{11}(f) = \frac{(Q_\mathrm{e} - Q_\mathrm{i})/Q_\mathrm{e} + 2iQ_\mathrm{i}(f - f_\mathrm{r})/f}{(Q_\mathrm{e} + Q_\mathrm{i})/Q_\mathrm{e} + 2iQ_\mathrm{i}(f - f_\mathrm{r})/f}. \tag{2.63}$$

An exemplary spectrum with resonance frequency $f_\mathrm{r} = 5\,\mathrm{GHz}$ and quality factors $Q_\mathrm{e} = 5 \times 10^4$ and $Q_\mathrm{i} = 2 \times 10^4$ is shown in fig. 2.14b). The absolute value of the scattering parameter $|S_{11}|$ has a minimum for $f = f_\mathrm{r}$. The spectrum can be understood qualitatively by considering the energy coupled into the system. When the resonance criteria of the cavity are met, standing waves can form. This requires energy from the driving microwaves. Therefore, less signal is reflected. If no standing waves form, i.e. $f \neq f_\mathrm{r}$, no energy is stored in form of a resonator mode. However, the actually measured back-scattering has an additional attenuation from the microwave cables δ, picks up a phase θ from traveling and there might be a constant offset $I_\mathrm{c} + iQ_\mathrm{c}$ due to microwave power that is reflected without undergoing the transition to a SAW and back. The final formula is then given by [75]

$$S_{11,\mathrm{meas}}(f) = \delta \times S_{11}(f)e^{i\theta} + (I_\mathrm{c} + iQ_\mathrm{c}). \tag{2.64}$$

Chapter 3

Design & Fabrication

In this chapter, we will detail the design and fabrication process used for the devices investigated in this thesis. Both cQED and SAW devices are based on (nano-)structured aluminum films created with standard thin film fabrication techniques like electron beam lithography (EBL) and electron beam evaporation. We will only provide a broad overview of the individual process steps and refer the reader to Ref. [57] for a detailed explanation. Step-by-step instructions along with process parameters can be found in the appendix B.

3.1 Design

The physical properties of circuit elements such as resonance frequency, impedance and coupling strength can be adjusted by changing the geometry of the elements. In this section, we will briefly discuss the design parameters and the chosen values for our cQED and SAW samples.

3.1.1 cQED Sample Design

A typical layout used for cQED measurements is shown in fig. 2.10a). A coplanar waveguide resonator (CPWR, green in the figure) is coupled to a microwave transmission line (vertical, red in the figure) and a Xmon qubit (capacitor colored blue). The resonator is only operated in the fundamental mode, i.e. as a $\lambda/4$ resonator. Important design parameters are the resonator and transmission line impedance as well as the eigenfrequency of both the resonator and the qubit. Additionally, the coupling between transmission/resonator and resonator/qubit can be adjusted by design.

3.1.1.1 CPW Resonator Design

To avoid reflection at interfaces between different circuit elements, the impedance Z of all circuit elements has to be matched. Typically, the common impedance is $Z = 50\Omega$. The exact calculation of the CPW impedance is not straight forward and will be omitted here, a detailed description with calculations for finite substrate thicknesses can be found in Ref. [76]. In the limit of infinite substrate thickness, the impedance equation simplifies to

$$Z = \frac{30\pi}{\sqrt{\epsilon_{\mathrm{r,eff}}}} \frac{K(k_0')}{K(k_0)}. \tag{3.1}$$

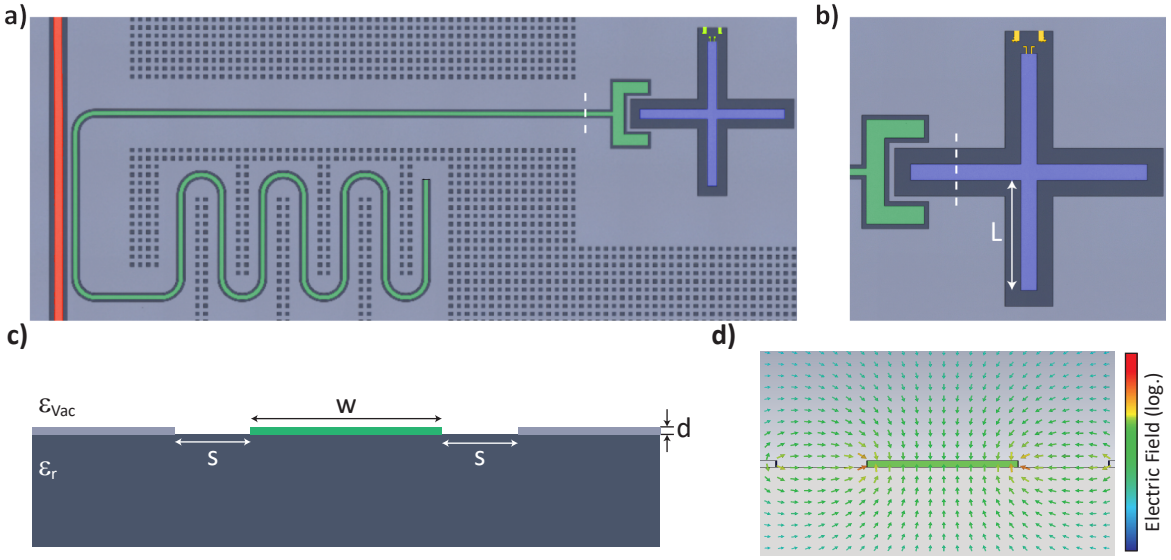

Figure 3.1: **a)** Optical micrograph of a sample section used for cQED experiments. A $\lambda/4$ coplanar waveguide (CWP) resonator (green) is coupled to a CPW transmission line (red) and a Xmon qubit (shunt capacitor colored blue). **b)** Zoom into the Xmon capacitor of panel a). The capacitor is cross-shaped. While the left arm is capacitively coupled to the readout resonator, the upper arm connects capacitor and ground through a dc-SQUID (not shown). Hooks (yellow) on the capacitor arm and ground plane help to establish contact between the single-layer metal and the subsequently fabricated dc-SQUID. The remaining capacitor arms with length L can be used to coupled to other circuit elements. **c)** Cross-section of the scheme in a) and b) along the dashed line, respectively. The signal line of the CPWR/the capacitor of the Xmon has a width w and is embedded by two ground planes (grey) with a gap s, the metal thickness is d. **d)** Electric field distribution of a superconducting CPWR (green in a)) on silicon simulated with CST Microwave Studio. The electric fieldlines, indicated by arrows, are present in both the surrounding vacuum on top and the substrate at the bottom in approximately equal parts.

Here, $K(k_0)$ and $K(k_0')$ are elliptical integrals of $k_0 = w/(w+2s)$ and $k_0' = \sqrt{1-k_0^2}$. The resonator width is denominated w, the gap to the ground plane s. In this approximation, Z stays constant for constant k_0. Therefore, a fixed ratio s/w allows for different resonator widths with approximately the same impedance. For our CPW resonators, we use $w = 10\,\mu\text{m}$ and $s = 6\,\mu\text{m}$. The transmission line is designed with $w = 20\,\mu\text{m}$ and $s = 12\,\mu\text{m}$. The effective dielectric constant $\epsilon_{\text{r,eff}}$ for an electromagnetic wave in the resonator is approximately [76]

$$\epsilon_{\text{r,eff}} = \frac{\epsilon_{\text{r}} + 1}{2}, \tag{3.2}$$

with ϵ_{r} being the dielectric constant of the substrate (e.g. $\epsilon_{\text{r}} = 11.9$ for silicon) and the $\epsilon_{\text{vac}} = 1$. The formula can be understood by looking at the electric field distribution in fig. 2.10d). This simulation was done with CST Microwave Studio. The field appears to be approximately symmetrically split in a part within the substrate and a part in the surrounding vaccum. The simulation yields an effective dielectric constant of $\epsilon_{\text{r,eff}} = 6.1$ which is close to eq. 3.2.

The effective dielectric constant together with the length l of the resonator determines its fundamental resonance frequency

$$\omega_\mathrm{r} = 2\pi \frac{c}{\sqrt{\epsilon_{\mathrm{r,eff}}}} \frac{1}{4l}, \tag{3.3}$$

where c is the speed of light in vacuum. For the used readout resonator in sec. 5.1 with a length around $l = 4\,\mathrm{mm}$, a CST simulation yields a resonance frequency of $\omega_\mathrm{r}/2\pi = 7.7\,\mathrm{GHz}$.

The external loss rate for the current design (fig. 2.10a)) with a coupling length of 400 µm, the ring-up time can be estimated[1] $\tau = 0.5\,\mu\mathrm{s}$.

3.1.1.2 Coupling Capacitance

Following eq. 2.25, the capacitance between the resonator and qubit C_g is the most easily accessible design parameter to adjust the coupling strength g. Increasing the capacitance, i.e. designing a larger overlap of the resonator with the qubit, increases the coupling strength. Finite element simulations with CST Microwave Studio[2] determine a coupling capacitance of $C_\mathrm{g} = 80\,\mathrm{fF}$ and a shunt capacitance $C_\mathrm{S} = 200\,\mathrm{fF}$. Assuming a typical transmon energy ratio $E_\mathrm{J}/E_\mathrm{C} \approx 50$ [55], eq. 2.25 leads to a coupling strength of $g/2\pi = 500\,\mathrm{MHz}$ for a resonator at eigenfrequency $\omega_\mathrm{r}/2\pi = 7\,\mathrm{GHz}$. However, for a reliable estimation of the coupling strength, the Josephson and charging energy E_J and E_C of the Josephson junctions have to be known exactly for the used qubit. Also, $C_\Sigma = C_\mathrm{S} + C_\mathrm{J}$ was assumed to be $C_\Sigma \approx C_\mathrm{S}$ for the calculation due to a lack of knowledge on the Josephson capacitance C_J. Without further measurements, an exact prediction of the coupling strength remains inaccessible.

3.1.1.3 Xmon Capacitor

The shunt capacitance C_S is an easily accessible design feature to change the effective ratio of Josephson and charging energy $E_\mathrm{J}/E_\mathrm{C}$ as $E_\mathrm{C} = e^2/2C_\Sigma$ with $C_\Sigma = C_\mathrm{S} + C_\mathrm{J}$. The X-shaped shunt capacitance is given by [78]

$$C_\mathrm{S} = 8L\epsilon_0 \left(1 + \epsilon_\mathrm{s}\right) \frac{K(k)}{K\left(\sqrt{1-k^2}\right)}, \tag{3.4}$$

where L is the length of a capacitor arm, K the complete elliptical integral and $k = w/(w+2s)$ with w as the arm width and s the gap to ground. Calculating the capacitance for our design ($L = 165\,\mu\mathrm{m}$, $w = s = 24\,\mu\mathrm{m}$) yields $C_\mathrm{S} = 92\,\mathrm{fF}$. This does not match a CST Microwave Studio simulation which results in $C_\mathrm{S} = 196\,\mathrm{fF}$. For future designs, this has to be investigated more closely as knowledge of C_S and the coupling capacitance C_g (also available from simulations) allows control over the qubit-resonator coupling strength g via eq. 2.25. However, to accurately predict the coupling strength, also the junction properties have to be known exactly. With future samples, DC-measurements of Josephson junctions will be implemented at mK-temperatures in order to investigate the critical current I_C and the capacitance C_J [79] to determine the Josephson and charging energy E_J and E_C.

[1] The calculation was done with a script to be found at https://smm.misis.ru/CPW-resonator-coupling/ following Ref. [77].

[2] Website: https://www.3ds.com/products-services/simulia/products/cst-studio-suite/

3.1.1.4 Josephson Junctions

For the cQED device investigated in this thesis, we use a "T-junction"-pattern [58, 78] which will be discussed further in sec. 3.2.2. The relevant design parameter is the Josephson junction area. For the presented data in sec. 5.1, Josephson junctions with a designed area $A = 170 \times 170\,\mathrm{nm}^2$ are used. With the junction area A, one can directly influence the anharmonicity $\alpha = -E_\mathrm{C}/\hbar$. When approximating the junction as a plate capacitor with AlO_x as insulator, we find $E_\mathrm{C} \propto 1/A$. Therefore, smaller junctions increase the anharmonicity and allow for qubit pulses with a larger bandwidth while still selecting only the $|g\rangle \rightarrow |e\rangle$-transition. However, the transmon regime $E_\mathrm{J}/E_\mathrm{C} \gg 1$ should not be left. A common trade-off is $E_\mathrm{J}/E_\mathrm{C} \simeq 50$ [55]. As mentioned previously, future measurements should allow for more control over the system with information on E_J and E_C gained in DC-measurements. Two Josephson junctions in parallel form a dc-SQUID. Therefore, the qubit is tunable by applying an external magnetic flux, see eq. 2.26. We design the dc-SQUID with an effective SQUID-area of $300\,\mu\mathrm{m}^2$, which has been used for past experiments [80].

3.1.2 Surface Acoustic Wave Elements

Surface acoustic wave resonators (SAWRs) consist of two basic circuit elements: interdigitated transducers (IDT) and Bragg reflectors. In this section, we will discuss important design parameters, mainly the impedance of an IDT and the optimal spacing of the reflectors for standing wave formation in the cavity.

3.1.2.1 Interdigitated Transducers

The fundamental SAW wavelength imposed by the IDT geometry is given by eq. 2.46. We design our samples with an electrode width of 183 nm. The resulting frequency of the SAW is $f = v_\mathrm{p}/\lambda_\mathrm{IDT}$ with the phase velocity v_p of the substrate. Hence, we expect a center frequency $f_\mathrm{IDT} \approx 5.2\,\mathrm{GHz}$ on the LNO/SiO_x/Si tri-stack with $v_\mathrm{p} = 3800\,\mathrm{m/s}$ (see fig. 2.4 and Ref. [46]). This value is only given as an approximation since the velocity under metallized surfaces differs from the free-space velocity following eq. 2.13. Additionally, a discrepancy can be seen between experimental data and simulations in fig. 2.4. However, we design the IDT to emit SAWs in a very broad frequency range by using only few electrode pairs, $N_\mathrm{p} = 5$. In eq. 2.52, we calculated the FWHM of the IDT frequency response to 0.9 GHz. To this end, the presumably narrow stop band of the Bragg reflectors (sec. 2.6.2.2) lies within the frequency range of the IDT.

To reduce backscattered signal by impedance mismatch of the IDT to the CPW transmission line, the impedance of the IDT has to be designed to $50\,\Omega$. Therefore, the equivalent circuit model depicted in fig. 2.11b) is investigated.

In good approximation, the only relevant part of the admittance $Y = G_\mathrm{a}(\omega) + iB_\mathrm{a}(\omega) + i\omega C_\mathrm{t}$ for impedance matching is the third summand. This can be argued by the following calculation: At the center frequency of the IDT f_IDT, the acoustic susceptance is $B_\mathrm{a}(f_\mathrm{IDT}) = 0$ [18] and we furthermore assume typical values for our designs with $K^2 = 5.4\,\%$ [40], $N_\mathrm{p} = 5$, $\omega_\mathrm{IDT}/2\pi = 5\,\mathrm{GHz}$, $W = 250\,\mu\mathrm{m}$ and $C_\mathrm{s} = 5.0\,\mathrm{pF/cm}$ for 128°Y-X bulk LNO[3] [18], $G_\mathrm{a}(\omega_\mathrm{c}) \approx 6.9 \times 10^{-3}\,1/\Omega$ (c.f. fig.

[3] C_s is the nomenclature following Ref. [73], in Ref. [18] this parameter is denoted as ϵ_∞.

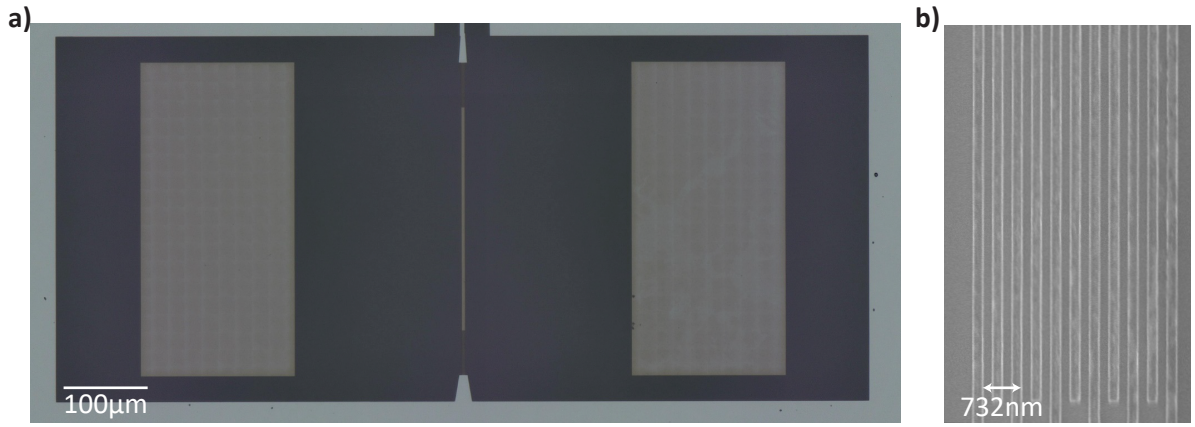

Figure 3.2: **a)** Optical micrograph of a 1-port SAWR as used for the experiments in this thesis. An IDT with 5 finger pairs is centered in a cavity formed by two Bragg reflectors with 500 single electrodes each. **b)** Zoom into the IDT of panel a). The electrodes are alternately connected to signal and ground. The width of a single electrode as well as the spacing between two electrodes is 183nm by design.

2.11a) for parameter definition). The capacitance can be calculated by elliptic integrals with eq. 22 of Ref. [81]. This leads to an admittance of $Y_\mathrm{t} = i\omega_\mathrm{c} C_\mathrm{t} = 1.6 \times 10^{-2}/\Omega$. The impedance Z is defined as the inverse of the admittance, so the absolute value is given by

$$|Z(\omega_\mathrm{c})| = \left| \frac{1}{G_\mathrm{a}(\omega_\mathrm{c}) + i\omega_\mathrm{c} C_\mathrm{t}} \right| = \begin{cases} 49.9\Omega & G_\mathrm{a} \text{ ignored,} \\ 47.2\Omega & G_\mathrm{a} \text{ included.} \end{cases}$$

The reason why we choose to ignore $G_\mathrm{a}(\omega_\mathrm{c})$ is the absence of knowledge about K^2 and C_s for our thin-film substrate. We expect the parameters to not change drastically compared to bulk LNO and hence a non-significant influence of $G_\mathrm{a}(\omega_\mathrm{c})$ on the impedance. Hence, it would be unreasonable to include the acoustic conductance G_a in the impedance calculation with guessed parameters.

3.1.3 SAW Resonator Design

A typical 1-port SAW resonator (SAWR) is shown in fig. 3.2a) and schematically in fig. 2.11a). It consists of an IDT and two gratings forming a cavity. All our designs use the same pitch p for both the gratings and the IDT despite the possible slight deviation of center frequencies. Panel b) in fig. 3.2 displays a magnified section of the IDT shown in panel a), the electrode width $a = 183\mathrm{nm}$ and pitch $p = 2a$ correspond to to a fundamental wavelength $\lambda_\mathrm{IDT} = 732\mathrm{nm}$ and center frequency $f_\mathrm{IDT} = v_\mathrm{p}/\lambda_\mathrm{IDT} \approx 5.2\mathrm{GHz}$ assuimg a phase velocity of $v_\mathrm{p} \approx 3800\mathrm{m/s}$ [46]. Note that the phase velocity is determined using a numerical simulation. The large bandwidth of the IDT of 0.9GHz allows excitations of wide variety of frequencies in the SAWR and it is therefore not crucial to tune the IDT frequency to the narrow stop band of the gratings (Bragg mirrors)

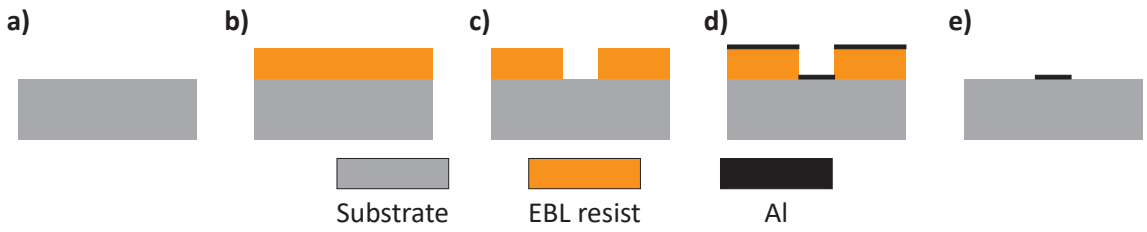

Figure 3.3: Standard electron beam lithography (EBL) and evaporation process. **a)** The cleaned substrate is **b)** spin coated with EBL resist and **c)** structured with electron beam exposure and chemical development. **d)** A homemade electron beam evaporation system is used to cover the sample with aluminium. **e)** Excess material is removed with a lift-off step.

calculated in sec. 2.6.2.2. For optimal transduction and standing wave formation, the conditions

$$d = \left(2n + \frac{1}{2}\right)\frac{\lambda_{\mathrm{IDT}}}{2} \tag{3.5}$$

$$d_{\mathrm{s}} = m\frac{\lambda_{\mathrm{IDT}}}{2} + \frac{a}{2} \tag{3.6}$$

with $m, n \in \mathbb{N}$ have to be fulfilled [75, 82]. As illustrated in fig. 2.11a), d is the distance between the mirrors, d_{s} the distance between the IDT and a mirror and L_{T} the width of the whole IDT. The distances d_{s}, L_{T} and d are measured from the center of the first strip of the respective resonator or IDT. The fundamental wavelength of the IDT is $\lambda_{\mathrm{IDT}} = 4a$ with the single electrode width a. Eq. 3.5 guarantees constructive interference of the wave after one round-trip while eq. 3.6 is experimentally found as the optimal distance between transducer and grating for maximal coupling [82]. While eqs. 3.5 and 3.6 hold for a single electrode reflectivity r_{s} with $\mathrm{Im}(r_{\mathrm{s}}) > 0$, they are a different for negative signs of the reflection coefficient [75, 82].
For the fabricated device , we use $a = 183\,\mathrm{nm}$ leading to $\lambda_{\mathrm{IDT}} = 732\,\mathrm{nm}$. Furthermore, we design $d = 399.855\,\mu\mathrm{m}$ ($n = 546$), $d_{\mathrm{s}} = 198.097\,\mu\mathrm{m}$ ($m = 541$) and $L_{\mathrm{T}} = 3.66\,\mu\mathrm{m}$. With an estimated phase velocity of $v_{\mathrm{p}} = 3800\,\mathrm{m/s}$ and single electrode reflectivity $|r_{\mathrm{s}}| = 1\%$, we find a center frequency $f_{\mathrm{c}} = 5.2\,\mathrm{GHz}$ with FWHM $\nu_{\mathrm{IDT}} = 0.9\,\mathrm{GHz}$ (eq. 2.51), a grating stop band width $\Delta f = 33\,\mathrm{MHz}$ (eq. 2.57) and a free spectral range $\nu_{\mathrm{FSR}} = 4.3\,\mathrm{MHz}$ (eqs. 2.60-2.62) of the cavity.

3.2 Fabrication

3.2.1 General Fabrication Process

Fig. 3.3a) shows the workflow of a standard EBL process. As substrates, we use commercially available Silicon (100) wafers with $\rho > 10\,\mathrm{k\Omega cm}$ for cQED chips. For SAW devices, we use a stack of silicon($350\,\mu\mathrm{m}$), silicon oxide($2\,\mu\mathrm{m}$) and lithium niobate 128°-Y-X-cut($500\,\mathrm{nm}$). The substrate is cleaned (a)) and spin coated with a positive electron beam lithography resist (b)). Afterwards, the device layout is transferred into the resist using EBL. Subsequently, the exposed areas of the resist are removed by immersing the sample in a suitable developer (c)). Next, Al is evaporated onto the sample with a homemade electron beam evaporation system with a rate of $10\,\mathrm{Å/s}$ (d)). The excess Al and resist are removed with a lift-off step in warm acetone (e)).

This general fabrication process is used for both cQED and SAW samples. The details on resist stack-ups, exposure dose and development differ depending on the substrate and the fabricated structure and will be disussed in the following.

3.2.2 cQED Device Fabrication

The fabrication of the circuit QED part of the devices, requires a precision fabrication of a superconducting qubit and a superconducting resonator. In particular, these two circuit elements can be categorized into resonant microwave structures based on single-layer superconductors and Josephson junctions, which require a three-layer process. Naturally, the precision fabrication of the two categories follow different optimization strategies, which are not necessarily compatible with each other. First, for the single-layer microwave circuit elements, i.e. the CPW tranmission lines, resonators, capacitors and ground planes (see fig. 3.1a)) we use the fabrication process discussed in sec. 3.2.1. A detailed fabrication recipe can be found in appendix B.1. To mitigate the problem of a non-continuous film at the edge of the initially deposited single layer structure, we introduced corrogated structures at the end of the qubits, which will host the dc-SQUID in the next step. This improved the issue of a non-continuous ruptured film of the dc-SQUID Al layers, as multiple walls, with varying orientation on the chip increase the chance of a partially horizontal coverage of the walls with the Al layers of the subsequent evaporation steps.
In a second step, we manufacture the dc-SQUID such that it shorts the Xmon capacitance to ground. We use a shadow evaporation technique using Dolan bridges [83]. For this method, a suspended resist strip (fig. 3.4a)) with widths $w_1 = w_2 = 170\,\mathrm{nm}$ and $w_2 = 170\,\mathrm{nm}$ is used as cover for certain areas of the substrate when evaporating Al from different angles. A fabricated dc-SQUID is shown in fig. 3.4d) colored red. For the realization of a suspended resist bridge, we use a double-layer resist with two different exposure doses. In particular, the lower resist has a lower exposure dose, while the top layer resist has a higher one. In the subsequent development process, we use two different developers to specifically remove exposed regions in the top and bottom resist, respectively. Crucially, the developer for the lower layer does not address the top resist.
As mentioned in sec. 3.1.1.4, we use "T-junctions" for our cQED devices [58, 78] (see fig. 3.4a)) compared to earlier work at the WMI [57, 80], where the junctions were based on a nose-type design. The advantage of the "T-junction" is that the Josephson junction dimension solely depends on the widths w_1 and w_2 of the pattern and does not rely on exact control over the angle α for the shadow evaporation. In addition, the "T"-shape acts as a stress relief to elongate the Dolan bridge, presumably increasing the stability [78].
Fig. 3.4a) shows schematic 3D- and top-down views of the sample during the aluminium evaporation. The exposed and developed resist (orange) forms a bridge, additionally undercuts are created along narrow structures in the pattern to ease the lift-off step. The first evaporation (left, blue) is done with an angle of $\alpha = 55°$ with respect to the surface normal leading to an effective shift s of the pattern on the substrate by $s = h\tan(\alpha)$ where h_b is the height of the bottom resist layer. Typical values for the used resist system (appendix B) are $h_\mathrm{b} \approx 700\,\mathrm{nm}$ for the bottom resist and $h_\mathrm{t} \approx 100\,\mathrm{nm}$ for the top resist. This results in $s \approx 1\,\mu\mathrm{m}$. Afterwards, the Al is oxidized *in-situ* to create an isolating AlO_x-layer. The thickness of the aluminium oxide

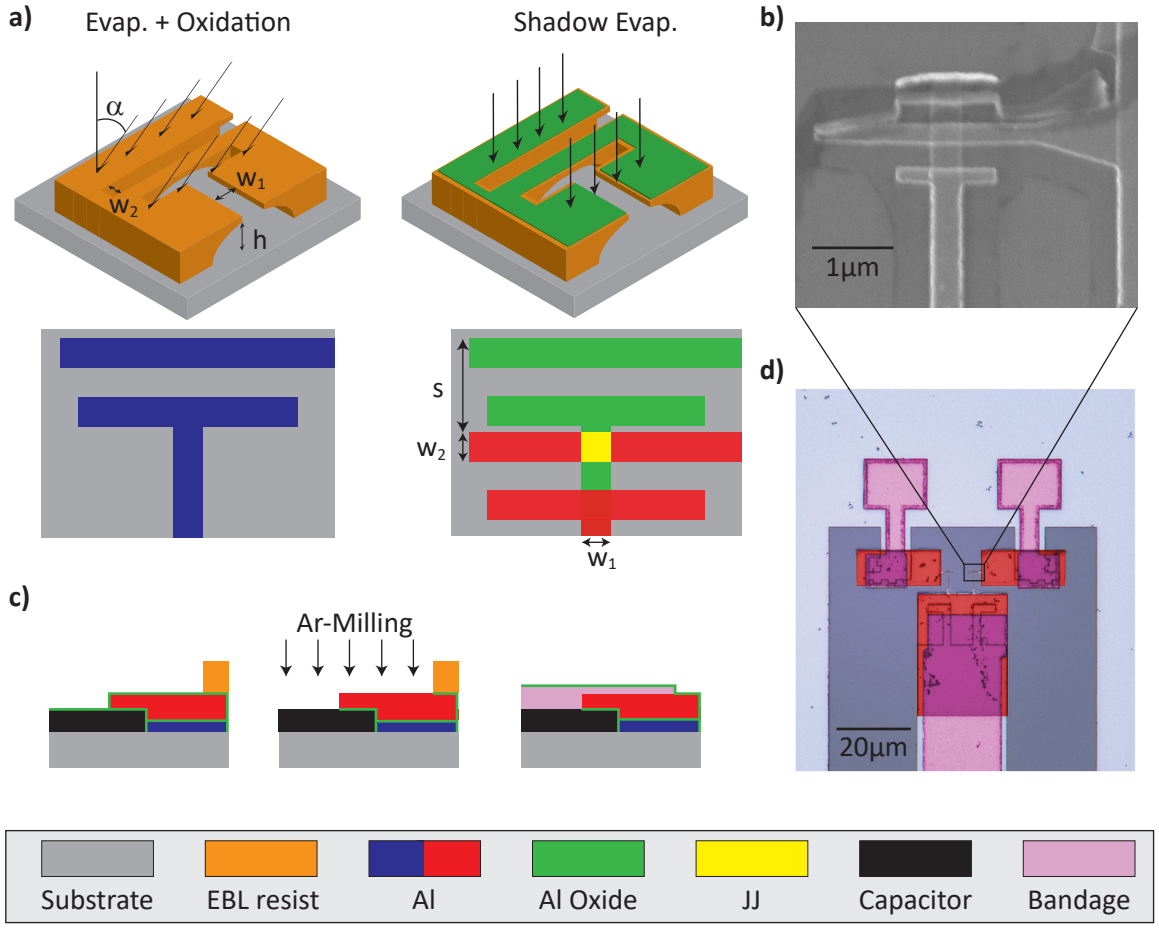

Figure 3.4: Fabrication scheme for Xmon qubits with a 3-step bandage process. **a)** Visualization of a Dolan-bridge shadow evaporation with oxidation. The first layer of Al is deposited under an angle of $\alpha = 55°$ w.r.t. the substrate normal (left). Subsequently, an oxidation process fully oxidizes the surface of the deposited Al (not shown). Lastly, a second layer of Al is deposited parallel to the surface normal (right), forming a Josephson junction (JJ) at the $Al/AlO_x/Al$ interface shown in yellow. The JJ dimensions solely depend on the widths w_1 and w_2 of the electrodes. **b)** Scanning electron microscope image of a Josephson junction. For the shown junction, a lift-off error occured as the horizontal electrode of the first evaporation step stuck to the resist and was not removed during the lift-off. **c)** Schematic fabrication procedure for the creation of bandages. Left: cross-section of the substrate-metal stack after the deposition of the dc-SQUID and EBL patterning of the bandage structure. No galvanic contact is established between the capacitor metal (black) and the dc-SQUID (blue/red) due to the oxidation of the capacitor in ambient conditions. Center: Argon-ion-milling is used to physically remove the exposed oxide layer of the capacitor and dc-SQUID in the bandage pattern. Right: An *in-situ* deposition of Al (magenta) provides galvanic contact between capacitor and dc-SQUID. **d)** Optical micrograph of a dc-SQUID with bandages. Black spots are resist residues which need further optimization to be completely removed. Hooks on the capacitor have been introduced to prevent edge discontinuations.

(green) is crucial for the critical current density characterizing the Josephson energy E_J. However, it is hard to estimate the exact thickness due to the statistical nature of the oxidation process [57]. Finally, a second layer of Al (red) is deposited without tilting the substrate. By carefully choosing the right spatial dimensions of the structures, a Josephson junction is created by the $Al/AlO_x/Al$ interface between the two deposited Al layers (yellow, lower right panel). In fig. 3.4b) a scanning electron microscope image of a Josephson junction can be seen. The size of the junction SEM micrography in the panel b) of fig. 3.4 is $300 \times 200\,nm^2$, for the measurements presented in sec. 5.1 however we use a different junction size of $170 \times 170\,nm^2$ to decrease the qubit eigenfrequency to a more beneficial value. As illustrated in the lower left panel of fig. 3.4a), an additional horizontal electrode (green) remains unconnected during the first angled shadow evaporation. This electrode is displaced by the effective shift $s \approx 1\,\mu m$ with respect to the resist structure in the top EBL resist. Therefore, an undercut of depth s would be necessary such that the electrode can stick to the substrate. This is usually not the case in the fabricated structures. Therefore, we try to remove the excess electrode by creating a small enough undercut such that the electrode is evaporated onto the resist wall but not onto the substrate. During the lift-off of the junction on display however, this electrode was not removed successfully. The reason is probably that part of the evaporated Al covers the substrate and sticks to it during the lift-off. This might also explain the "tilted" appearance of the electrode. To this end, we did not manage to reproducibly remove the electrode with the current fabrication parameters, so further optimization is needed here. The remaining electrode does not impair the basic functioning of the qubit but might reduce the coherence.

After the definition and the realization of the single-layer circuit elements, naturally an oxide layer with a thickness of 1 to 10 nm forms on the aluminum, as it is exposed to ambient conditions [84]. This prevents galvanic contact between the SQUID, which is created in the second, multi-layer fabrication step with the previously deposited single-layer elements (fig. 3.4c), left). Therefore, an argon-ion-milling step is incorporated into the fabricaton procedure to ensure galvanic contact by removing the oxide layer. Instead of milling *in-situ* before the evaporation of the dc-SQUID [58], we follow the approach of Dunsworth et. al [85] in order to avoid damaging the silicon substrate during the milling process. This bandaging process is illustrated in fig. 3.4c). In a third additional lithography, we define a bandage that connects the capacitor/ground plane (black) from the first fabrication step with the dc-SQUID (red & blue). Subsequently, the oxide layer is physically milled with argon ions and a bandage layer of Al is deposited (magenta).
The fabricated structure in fig. 3.4d) is the dc-SQUID of the investigated qubit in section 5.1. The dc-SQUID shorting the capacitor to ground is colored red, the bandage providing galvanic contact is colored magenta.
In the following, we discuss the fabricated structure and possible future optimization of the fabrication. Especially in the bandage regions, but also close to the junctions, there is a lot of resist residue visible. Resist residue can be a source of decoherence in superconducting qubits. This can be overcome by descuming [86], i.e. a very weak O_2 ashing process, before evaporating. Also, further optimization of the resist stack, exposure dose and development can reduce the remaining resist spots. Additionally, the outline of the bandage layer - especially at the top in panel d) of fig. 3.4 - is clearly visible in a dark color. We interpret these features to show cross-linked

resist covered with Al. The bandaging process was done in a sputter deposition chamber because the argon-ion-gun in the evaporation system was not strong enough to remove the oxide layer. There are two possible explanations for the cross-link: The sample could have been heated too much during the deposition process or the undercut resist at the edge broke. We introduced an undercut for the bandage structure to ease the lift-off. Future improvement is mainly expected by moving the deposition process to a commercial evaporation system (PLASSYS). The machine allows an *in-situ* descuming process as well as argon-ion-milling. Therefore, all deposition steps can be done in the same system. Especially, we expect a large improvement in the bandage quality by avoiding a sputter chamber that is also used for the deposition of AlN, a piezoelectric.

3.2.3 SAW Device Fabrication

Samples for SAW experiments are fabricated following the scheme in fig. 3.3. Additionally to the EBL resist, a conductive resist is required when working with an insulating substrate material such as bulk LNO. Otherwise, electrons accumulate around the point of incident during exposure and lead to an over-exposition of the resist. In contrast, when working with thin-film LNO on a 2µm SiO_x layer on a Si substrate however, the conductivity of the bulk silicon substrate is sufficiently large to prevent charging effects and therefore we chose a single layer positive EBL resist PMMA/MA(33%) (AR-P 617.08). The devices are fabricated following the scheme in fig. 3.3. The detailed fabrication parameters can be found in appendix B.2.
The surface acoustic wave resonators require the fabrication of two end mirrors, which are realized in the form of Bragg mirrors. However, the exposure dose required for the definition of these structures has a non-trivial spatial distribution due to the effect of amount of back-scattered electrons, which also depend on exposed areas in close proximity. This so-called proximity effect represents a challenge for the fabrication of this mirrors, however, as we detail in sec. 3.3. The usage of a proximity effect correction software can account for this challenge and compensate for this effect by spatially adjusting the exposure dose.

3.3 Proximity Effect Correction with BEAMER

Electron beam lithography uses accelerated electrons to change the chemical structure of the resist. By confining the electron beam to spot sizes of a few tens of nanometers, extremely small structures can be fabricated. However, the so-called proximity effect has a large influence on the achievable resolution [87]. Proximity effect (PE) is created by backscattered electrons in the substrate. Since this backscattering can lead to electron trajectories in all directions, the PE is responsible for exposure away from the point of beam incidence. Effectively, the exposure dose at a certain point is therefore increased by the PE contribution from all surrounding exposed points. This causes a dose dependence on the position in the pattern: Points surrounded by other exposed regions are subjected to more dose than points at the edges or corners of structures. Especially for SAW Bragg mirrors consisting of narrow strips with a length of $\sim 350\,\mu m$, a width of $\sim 200\,nm$ and similar spacing, this effect can influence the fabricated structure significantly. Exposing the whole mirror with the same dose would therefore lead to an underexposure of the edges in the case when the dose is optimized for a well-defined center of the mirror while

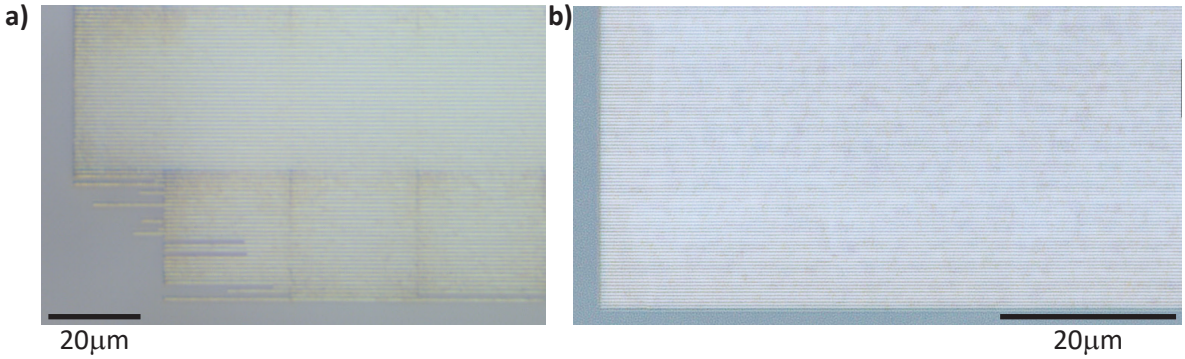

Figure 3.5: Optical micrograph of fabricated Bragg mirrors without (**a)**) and with (**b)**) proximity effect correction via BEAMER and TRACER. In **a)**, the dose was optimized for the center of the Bragg mirror. Due to the lack of proximity exposure, the edges of the mirror are underdeveloped, visible by the darker color of the electrodes which is most likely due to resist residues. In the corners, the underexposition is so significant that the resist is not developed. Therefore, the electrodes are completely removed during the lift-off. Image **b)** was taken for the same layout with a proximity effect corrected electron beam lithography. Here, the exposure dose is enhanced at the edges and corners to cope for the missing proximity effect by neighboring structures. The effective dose is the same for all electrodes wherefore the edges and corners are fully developed.

well-defined edges would require an overexposition of the center. An example of this issue can be seen in fig. 3.5a). Here, the corner of the structure is heavily underexposed such that the resist is not fully removed in the following development. Therefore, the Al cannot stick to the substrate and is removed in the lift-off step. Furthermore, a color gradient is visible from the edges towards the inner part of the SAW mirror. We assume that there is more resist residue at the edges due to the decreased exposure dose.

BEAMER and TRACER are software packages by GenISys GmbH[4] to account for backscattering and perform a proximity effect correction (PEC). Based on a Monte-Carlo simulation of the electron scattering processes in the resist and substrate (see fig. 3.6a)), a point spread function (PSF) for a specific substrate-resist stack-up is generated (panel b)). Here, the accumulated energy deposited in the resist is expressed as a function of distance from the beam incident point. With this information, PEC can be applied to any exposure pattern, accounting for back-scattering and (if known) beam broadening. Areas with high density patterns receive a reduction in dose while isolated structures will have an increased exposure dose assigned. The optimization goal of the software is to accurately imprint the pattern in the resist. Using this software package, we were able to improve the fabrication of SAW Bragg reflectors as shown in fig. 3.5b). The exposure dose for regions close to the edges and corners of the structure was enhanced such that the effective dose (including backscattering) is equal at any point in the pattern.

[4]Website: https://www.genisys-gmbh.com/

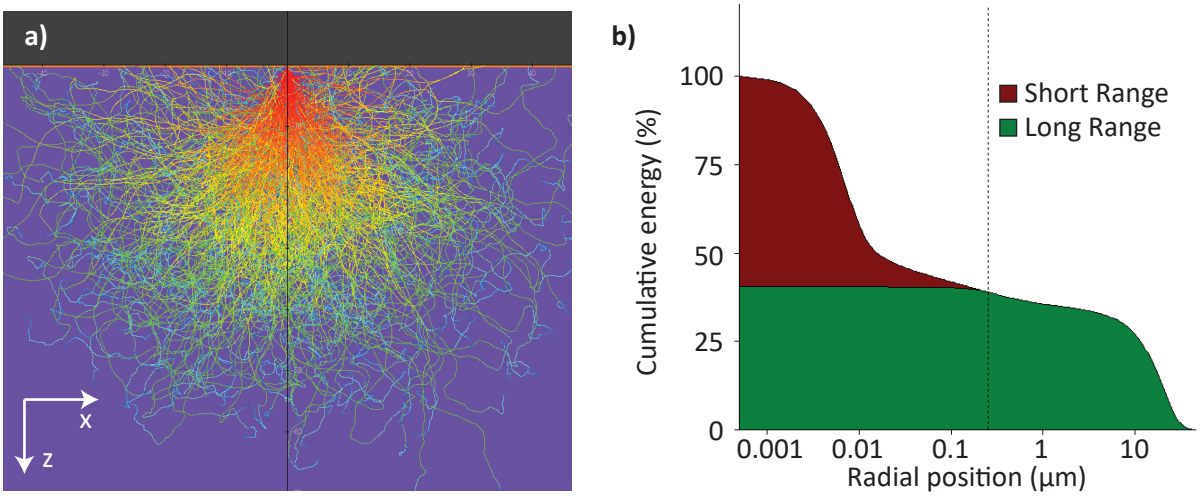

Figure 3.6: **a)** Cross-section of a TRACER point spread function (PSF) simulation. The substrate (purple), the resist (orange) and the acceleration voltage of the lithography system are defined by the user. The path of incident electrons (colored lines) is then simulated with a Monte-Carlo simulation and the effective energy deposited in the resist at each distance from the incident point is stored. **b)** 2D-PSF of the shown tracer simulation. The PSF is a radial cross-section of the deposited energy in the xy-layer at half the depth z of the resist. At the point of incident, the energy is normalized to 100%. TRACER then calculates the relative deposited energy with respect to the distance of the beam incident. For distances larger than 30 µm, the resist is not affected by the exposure. With this PSF, BEAMER can adapt the exposure dose for a given pattern such that the same amount of energy is deposited anywhere in the structures.

Chapter 4

Measurement Setup

All presented measurements were performed in a commercial TRITON400 dilution refrigerator by Oxford Instruments with a working temperature of 90 mK. The measurement techniques for cQED and SAW measurements are very similar and only differ in minor aspects. In order to avoid unnecessary repetitions, we therefore describe the setup employed for the cQED measurements in sec. 4.1 and then discuss the differences for the SAW setup in sec. 4.2. In order to protect the flux-tunable transmon qubits for our cQED experiments against flux noise, we place the sample with its packaging inside a (superconducting) aluminum shield.

4.1 cQED Measurement Setup

This section is structured as follows: we start with a discussion about the continuous wave excitation and spectroscopy experiments in the frequency domain. Then, we continue with the setup used for time domain measurement.

4.1.1 Frequency Domain Measurements

For the initial spectroscopy of the microwave resonator coupled to a superconducting qubit, we employ continuous wave excitation scemes combined with microwave transmission experiments.

A schematic drawing of the whole setup is shown in fig. 4.1. As microwave spectroscopy techniques typically employ (at least) two microwave tones, we use two separated input lines. One input line is dedicated for the spectroscopy of the microwave resonator (blue) and a second one to excite the qubit (magenta). The used devices are synchronized to the internal 10 MHz clock of the vector network analyzer (VNA) and connected to a local network which allows remote control via LabView.

As discussed in sec. 2.3.3, we need to extract information about the readout resonator which we probe with a VNA [88]. This device allows us to determine the absorption line of the resonator and hereby its resonance frequency, linewidth and absorption properties. The nature of the experiments requires that we minimize the amount of thermal (microwave) noise photons interacting with the investigated device. To this end, we place microwave attenuators at the different temperature stages of the dilution refrigerator. For the given line attenuation (see fig. 4.1) of the input line to the microwave resonator, we expect with this configuration $\mathcal{O}\left(10^{-2}\right)$ residual thermal noise photons at $\omega_\mathrm{r}/2\pi = 7.2\,\mathrm{GHz}$ [89]. The nominal attenuation values shown in fig. 4.1 sum up to $-52\,\mathrm{dB}$. In addition, we have $-9.9\,\mathrm{dB}$ due to losses of the microwave lines[1].

[1] This values originates from a calibration done prior to this thesis, see sec. 6.5 of Ref. [80].

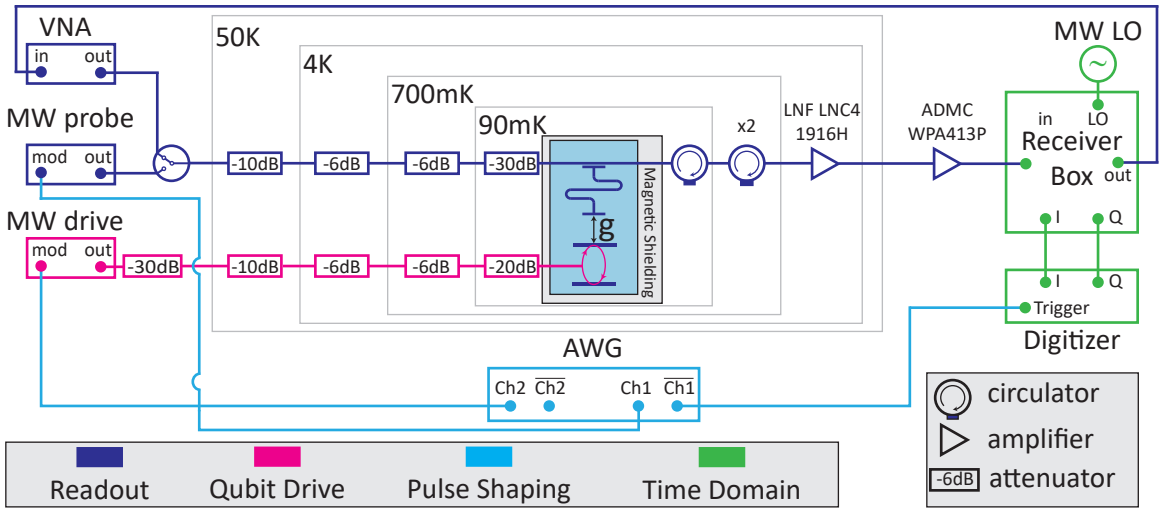

Figure 4.1: Measurement setup for cQED measurements. The sample is placed in a dilution refrigerator operating at 90 mK and connected via microwave lines to the lab environment. Different parts of the setup are color coded. All instruments are synchronized to the internal 10 MHz clock of the VNA.

As we will see in sec. 5.1.3, the attenuation is higher than expected. After interacting with the resonator-qubit system, the signal passes three circulators to insulate the sample from thermal noise via the output line. Subsequently, the signal is amplified by a cryogenic HEMT-amplifier with a gain of 42 dB when operating at 4K. At room temperature, the signal is further amplified prior entering the “receiver box", which allows to transmit the signal, as used in the continuous wave experiments or to downconvert the signal to an intermediate frequency as discussed in sec. 4.1.2. The VNA then measures phase-sensitive information about the transmitted microwave signal in the form of the complex scattering parameters S_{21}.

In order to manipulate the qubit state with microwaves, we apply drive pulses via the “Qubit Drive” path. To this end, we employ a microwave vector signal generator with a frequency range from 10 MHz to 12.75 GHz which is connected to the antenna line of the inspected qubit. The qubit state can be read out via the readout resonator which is capacitively coupled to the qubit. For the readout, the probe signal is attenuated throughout the different temperature stages to minimize thermal noise.

4.1.2 Time Domain Measurement

For time domain measurements, we utilize the specialized setup built by Stefan Weichselbaumer in Ref. [90]. We will provide an overview of the setup and point out notable differences in this section. For further technical details we refer the reader to the corresponding chapter in Ref. [90]. For a detailed description of time domain measurements with superconducting qubits, we refer the reader to Ref. [57].

Additionally to the “Readout” and “Qubit Drive” paths, we introduce a path “Pulse Shaping” for triggering drive and readout pulses. The core element is an arbitrary waveform generator (AWG) with two output channels and corresponding inverse channels, indicated by bars over the

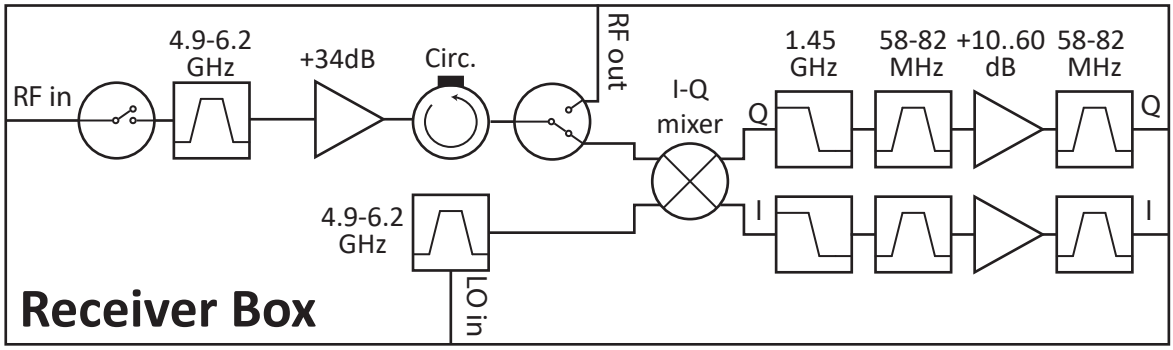

Figure 4.2: Schematics of the receiver box for microwave down-conversion. The signal is IQ-mixed with a local oscillator to an intermediate frequency (IF) of 62.5 MHz for digitization. The bandpass filters at the input of the RF and LO signal can be exchanged to cover the investigated frequency regime.

label in fig. 4.1.

For the time domain experiments, we use a pulsed excitation scheme of the readout and qubit excitation input lines. The details of the connection scheme are presented in Fig 4.1. After the continuous wave characterization of the coupled resonator-qubit system, we have determined the frequency of the microwave resonator ω_r and the frequency of the qubit ω_q. In detail, we configure the microwave source exciting the resonator to operate in pulse-modulation mode and set its frequency to ω_r. Channel 1 of the AWG then controls the amplitude of the microwave radiation with an on-off ratio of 80 dB [91] using a TTL control signal. The inverse voltage pulse is sent to the trigger of the digitizer card starting the acquisition if the card is armed.
To perform controlled qubit manipulation, we employ a vector source modulated by channel 2 of the AWG. The vector source can take an IQ-signal as modulation input. Therefore, elaborate pulse shaping with sideband mixing of a carrier signal is made possible (see Ref. [90] for details). However, in our experiments, we set the internal local oscillator of the vector source to the desired output frequency, e.g. ω_q for resonant drive, and feed the I-channel of the modulation input with a simple rectangular pulse with typical lengths on the order of tens to hundreds nanoseconds. This allows us to exploit the large modulation bandwidth of the vector source to achieve much faster rise times (1 GHz bandwidth [92]) than achievable with common pulse-modulated signal generators. A disadvantage of the modulation technique in the form we implement here is the so-called leak through, which is resonant with the qubit and hence also has the ability to excite or disturb it. However, the IQ-mixer in the used vector source has an on-off ratio of > 45 dB, so leaking signals can be neglected after the additional attenuation in the cryostat.

For the experiments in the time domain mode, we configure the receiver box to downconvert the microwave signals to an intermediate frequency, which are subsequently digitized with a fast data acquisition card. The schematic of the receiver box wiring is shown in fig. 4.2. It was built in the scope of Ref. [90] and slightly adapted for our measurements by changing filters to suitable frequency ranges. The pin switch at the input port of the signal path is not used in our experiments and remains permanently closed at all times of the measurement. Following a bandpass filter, that is chosen individually for the measurement to cover the frequency range of

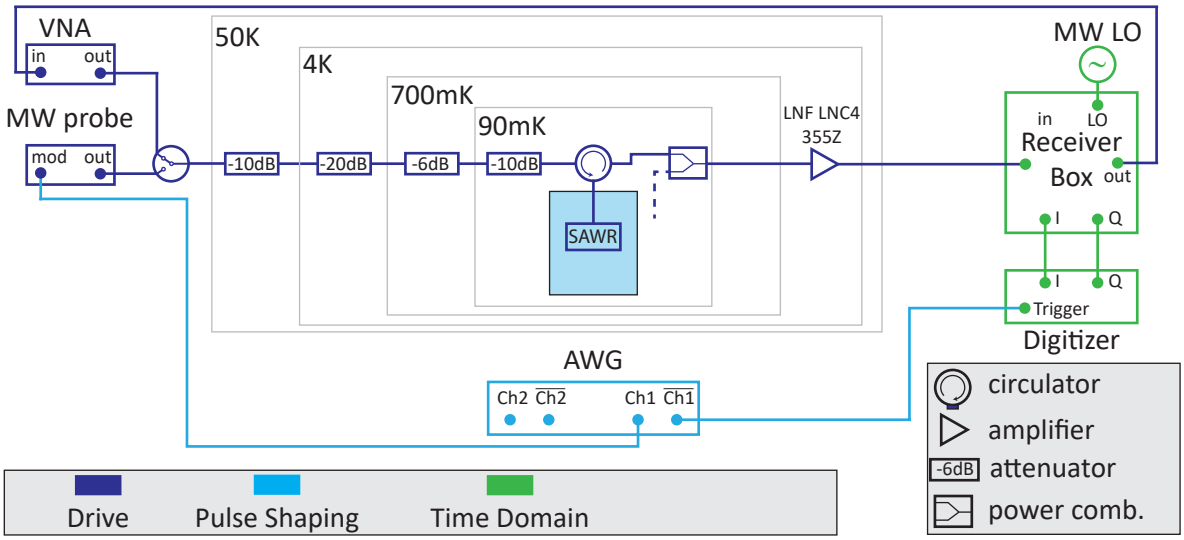

Figure 4.3: Measurement setup for SAW measurements. Our SAW one-port resonators are measured in reflection using a circulator to seperate incoming from outgoing signals. A power combiner is used to enable measurement of two different structures.

interest, a microwave amplifier with nominally 34dB gain increases the signal strength of the readout tone at frequency ω_r. A circulator is used to protect the amplifier from backscattered microwaves. Subsequently, a microwave switch directs the signal to an IQ-mixer. Alternatively, as for the frequency domain measurements, the switch can be set to output the amplified signal directly. A strong local oscillator with 15dBm and a frequency $\omega_\mathrm{LO}/2\pi = \omega_\mathrm{r}/2\pi - 62.5\,\mathrm{MHz}$, where $\omega_\mathrm{IF}/2\pi = 62.5\,\mathrm{MHz}$ is the so-called intermediate frequency (IF), is mixed onto the incoming signal. This projects the in-phase (I) and quadrature (Q) information onto signals with frequencies $\omega_\mathrm{r} - \omega_\mathrm{LO} = \omega_\mathrm{IF}$ and $\omega_\mathrm{r} + \omega_\mathrm{LO}$. The up-converted signal and broadband noise are suppressed by the following lowpass and bandpass filters while the signal at ω_IF is amplified by a FEMTO DHPVA-200 Voltage-Amplifier with a variable gain from 10 to 60dB before reaching the output ports of the box. The down-converted I- and Q-signals are fed to a Spectrum M4i.4451-x8 digitizer card with a sampling rate of 500MSamples/s and 14 bit resolution. If the trigger channel of the card receives a pulse by the AWG, the data acquisition starts. Since the card has the option to record pre-trigger data, timing of the microwave signal and the recording is not crucial as long as any potential delays remain constant. The I- and Q-signals are digitized and recorded by a measurement computer. The data is then demodulated with ω_IF using a software tool[2] introduced in Ref. [90]. The in-phase and quadrature information reveal the magnitude $A = \sqrt{I^2 + Q^2}$ and phase $\phi = \arg(I + iQ)$ of the probe signal. The interpretation of the data is discussed in sec. 5.1.

4.2 SAW Measurement Setup

Fig. 4.3 shows the setup for SAW measurements which almost identical to fig. 4.1. A different input line is used, such that the attenuation differs from cQED experiments. We drive the

[2] Available at https://gitlab.com/stwe/echo-demodulator

one-port SAW resonator with a microwave source and measure the reflected signal. To separate signal reflected elsewhere along the way from signal reflected by the investigated structure, we use a circulator directing the microwave to a dedicated output line. A power combiner allows the measurement of two different structures with the same output line. Apart from that, all data processing is handled as described in sec. 4.1.2.

Chapter 5

Experimental Results

For quantum acoustodynamic experiments, the superconducting Xmon qubit coherently couples to single phonons of the SAW resonator. Within this scheme, qubit states can be mapped to the slow traveling acoustic waves and interfere with the (in the meantime coherently manipulated) qubit at a later point in time. Here, the main difference to the system where a superconducting qubit interacts with a superconducting resonator is the travel time or retardation typically coming along with the acoustic wave resonator. For successful experiments, one requirement is a sufficiently long qubit coherence time to map a quantum state onto a phonon and interfere with this state after a typical transit time of the phonon on the order of 100 ns to 1 us [30]. One of the technical requirement is to adjust the resonance frequency of the SAW resonator to the properties of the qubits. For both systems, established concepts to realize GHz circuit elements exist and we therefore will tailor both the qubit and the SAW resonator to operate in this frequency regime. The fundamental SAWR frequency is determined by the single electrode width, exemplarily an electrode width of $a \approx 180\,\mathrm{nm}$ leads to a SAW resonator frequency of to approx. 5 GHz. Within this chapter, we first present results about the superconducting qubit followed by a discussion about the properties of the investigated SAW resonator.

5.1 Experimental Results of the Coupled Transmon-Microwave Resonator Device

In the following, we characterize a transmon qubit designed and fabricated as described in sec. 3.2.2. Starting with an analysis of the readout resonator, we gain insight into its resonance frequency ω_r, coupling rates κ_r as well as the flux-current dependence of the coil mounted to the sample. Following these single-tone experiments, we conduct two-tone spectroscopy to gain insight on the qubit frequency ω_q, its coupling strength g to the resonator, anharmonicity α and intrinsic dephasing rate γ_ϕ. Furthermore, we use the photon-number dependent frequency of the transmon qubit to perform an accurate power calibration of the readout and drive tones, extracting the total attenuation of the microwave setup. Lastly, time domain spectroscopy is conducted to gain information about relevant qubit timescales T_1, T_2 and T_ϕ.

5.1.1 Single-Tone Spectroscopy

We start by characterizing the readout resonator with a continuous wave transmission measurement. As shown in fig. 2.10, the investigated sample consists of a microwave transmission line

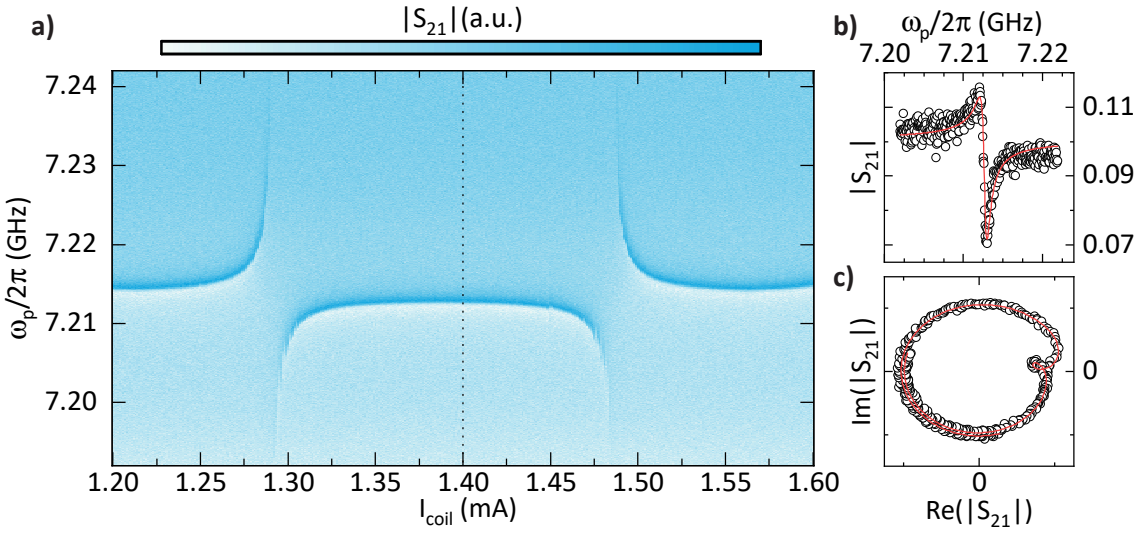

Figure 5.1: Characterization of the resonant interaction between microwave resonator and qubit. **a)** Linear port-to-port microwave transmission S_{21} through the sample transmission line as a function of the applied coil current I_{coil}. Avoided crossings are visible around $I_{\mathrm{coil}} = 1.28\,\mathrm{mA}$ and $I_{\mathrm{coil}} = 1.48\,\mathrm{mA}$ where the transmon becomes resonant with the microwave resonator, i.e. $\omega_{\mathrm{q}} = \omega_{\mathrm{r}}$. **b)** Frequency dependent microwave transmission magnitude $|S_{21}|$ and **c)** real part of $|S_{21}|$ versus imaginary part of $|S_{21}|$ at fixed coil current $I = 1.40\,\mathrm{mA}$ (dashed line in a)). Solid lines are fits to the data according to Ref. [93]. From the fits we extract $\omega_{\mathrm{r}}/2\pi = 7.213\,\mathrm{GHz}$, $Q = 8155$ and $Q_{\mathrm{int}} = 10182$.

coupled to a $\lambda/4$ microwave resonators. For this notch-port coupling, the transmitted signal $|S_{21}|$ shows an absorption dip at the resonance frequency ω_{r} of the resonator. The general response of a harmonic oscillator is Lorentzian [94]. However, a more complex behavior can be observed in microwave circuits with nonideal impedance matching [95]. Moreover, to identify a functioning resonator-qubit pair, we measure the frequency dependent microwave transmission as function of the current through the coil which is mounted on top of the sample box. The magnetic field, which is generated by this coil changes the magnetic flux through the dc-SQUID of the Xmon and hereby tunes its resonance frequency $\omega_{\mathrm{q}}(\Phi)$ in a periodic fashion according to eq. 2.26. As discussed in section 2.3, we expect a level repulsion of the resonance feature of the resonator and the transition frequency of the qubit in the limit of the strong coupling regime, which manifests itself as an anticrossing in the absorption function of the superconducting resonator. We observe this avoided crossing as regular pattern when analyzing the microwave transmission signal as function of the coil current I_{coil} and probe frequency ω_{p}. Fig. 5.1a) shows two anticrossings in the absorption spectrum of the readout resonator. The port-to-port transmission parameter $|S_{21}|$ of the microwave signal is colorscaled. We do not account for the total attenuation and amplification of the signal in the circuitry, for data analysis purposes, the signal is either normalized or scaling factors in the fitting functions account for offsets. The shown spectrum is mainly composed out of the transmission function of the microwave resonator, whose resonance frequency is independent of the applied magnetic field. The resonator becomes resonant with the transition frequency of the qubit at 1.28 mA and 1.48 mA resulting in the mentioned anticrossing. In the magnetic field

of coil currents of $1.2 - 1.25\,\mathrm{mA}$, $1.32 - 1.45\,\mathrm{mA}$ and $1.51 - 1.6\,\mathrm{mA}$, the microwave resonator shows a nearly constant resonance frequency. However, the resonance frequency is reduced in the middle section due to the dispersive shift originating from the resonant coupling with the qubit. For example, at a coil current of $1.4\,\mathrm{mA}$, we observe a notch-type resonance feature attributed to the microwave resonator at $7.21\,\mathrm{GHz}$.

At these large qubit-resonator detunings, we can determine the resonator characteristics (see figs. 5.1b) and c)). These panels show the frequency dependence microwave transmission magnitude and the real part versus the imaginary part of the transmission at a fixed coil current $I = 1.40\,\mathrm{mA}$. Fitting the data with a "circle-fit" algorithm detailed in Ref. [93] and openly available[1], we find the resonance frequency at $\omega_\mathrm{r}/2\pi = 7.213\,\mathrm{GHz}$. Simulations of this circuit layout with CST Microwave Studio predict a resonance frequency of $7.7\,\mathrm{GHz}$. The 5% deviation in the resonance frequency is attributed oxides on the substrate- and metal-interfaces changing the effective dielectric constant. Additionally, the fit determines a total quality factor (loss rate) of $Q = 8155 \pm 345$ ($\kappa_\mathrm{r} = (885 \pm 38)\,\mathrm{kHz}$). The external and internal quality factors (loss rates) are $Q_\mathrm{e} = 40949 \pm 889$ ($\kappa_\mathrm{r,e} = (176 \pm 37)\,\mathrm{kHz}$) and $Q_\mathrm{i} = 10182 \pm 528$ ($\kappa_\mathrm{r,i} = (708 \pm 2)\,\mathrm{kHz}$). Due to the relation of the coupling rates $\kappa_\mathrm{r,i} > \kappa_\mathrm{r,e}$, the resonator is dominated by internal losses and comparably weakly coupled to the transmission line. Typically, a readout resonator should have its dominant loss channel to the transmission line such that $\kappa_\mathrm{r,e} \gg \kappa_\mathrm{r,i}$. Therefore, for future samples the external coupling strength should be increased, e.g. by decreasing the distance of the transmission line and the resonator line and elongating the coupling length. Additionally, better internal quality factors should be achieved by surface treatment to increase the quality of metal/substrate- and substrate/air-interfaces [96] and switching the fabrication procedure to a substractive etch process rather then a lift-off process to improve the metal edge quality [57].

5.1.2 Two-Tone Spectroscopy

With knowledge of the readout resonator we can start to characterize the qubit coupled to it. For two-tone measurements we send a continuous microwave tone through the transmission line probing the resonator at its resonance frequency ω_r. This resonance frequency was determined without any excitation of the qubit and low probe tone powers of $P_\mathrm{appl,RO} = -50\,\mathrm{dBm}$ corresponding to a mean photon occupation number of the resonator of less than 15 photons (c.f. 5.1.3) such that the qubit was in state $|g\rangle$. As discussed in sec. 2.3.3, the qubit state dependent frequency shift of the resonator 2χ will lead to a change in the transmission amplitude of the probe tone when the qubit is in the excited state as visualized in fig. 2.5c). Therefore, we can utilize this dispersive shift when exciting the qubit with a second microwave tone. When we measure the dispersive shift, here in terms of a change in the resonator transmission, as function of the qubit excitation frequency ω_d and the coil current I_coil, we can determine the dispersion of the qubit frequency (see fig. 5.2a)). We identify the dark blue regions in the spectrum with resonant qubit transitions, leading to a change in the probe tone transmission. In panel b), we extract the drive frequencies at which the qubit is excited. At most coil currents, we find two transition frequencies. Following the spectrum in fig. 2.6c), we identify the higher frequency with the qubit frequency ω_q. The lower frequency can be attributed to a single photon of the two-photon

[1] GitHub: https://github.com/sebastianprobst/resonator_tools.

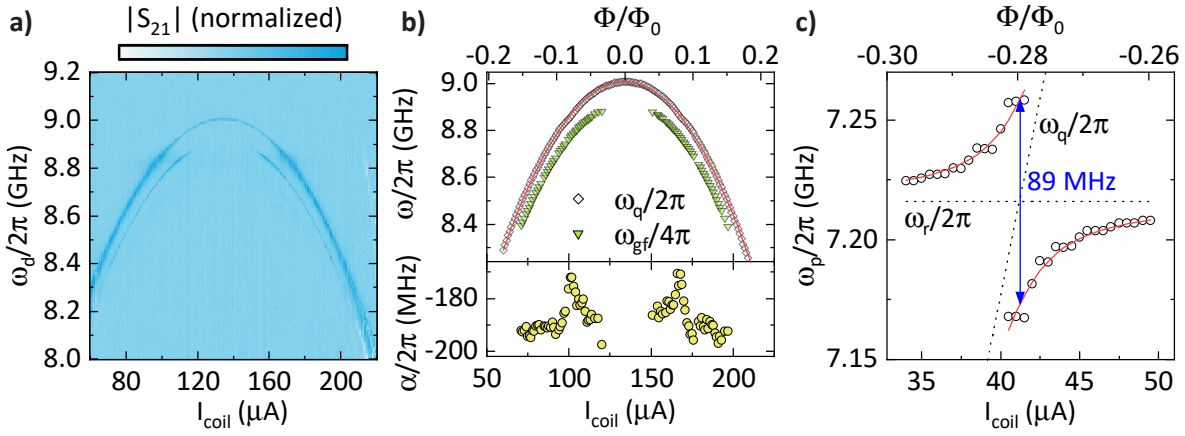

Figure 5.2: Two-tone spectroscopy of the flux-tunable Xmon. **a)** Microwave transmission $|S_{21}|$ measured at the resonator resonance frequency ω_r as a function of applied coil current and qubit drive frequency. Changes in the transmission are caused by a qubit-state dependent shift of the resonance frequency (dispersive shift). The dark blue signatures can be associated with excited qubit states. **b)** Qubit resonance frequencies as a function of coil current/bias flux extracted from a) using Lorentzian fits. We have identified two transitions, the qubit transition $|g\rangle \rightarrow |e\rangle$ at ω_q and the two-photon process $|g\rangle \rightarrow |f\rangle$. The latter is visible at the frequency of single photon at $\omega_\mathrm{gf}/2$ in the spectrum. The red line is a fit of eq. 2.26 to the transition frequency ω_q. The lower panel shows the anharmonicity α at each coil current where both transitions are visible. A slight deviation at $I_\mathrm{coil} = 100\,\mu\mathrm{A}$ and $170\,\mu\mathrm{A}$ is visible. To obtain the overall anharmonicity, we average over all values. **c)** Detailed avoided crossing of the single-tone experiment in fig. 5.1a). With the fit parameters from panel b), we can calculate the qubit frequency in the anticrossing (dashed line $\omega_\mathrm{q}/2\pi$). Fitting eq. 2.20 to the dressed states reveals good agreement of the resonant Jaynes-Cummings model with the measurement. From the fit, we extract a resonator-qubit coupling rate of $g/\pi = 89\,\mathrm{MHz}$, which is the energy splitting of the dressed states at $\omega_\mathrm{q} = \omega_\mathrm{r}$.

process driving the transition $|g\rangle \rightarrow |f\rangle$. This transition has a energy gap $\omega_\mathrm{gf} < 2\omega_\mathrm{q}$ due to the negative anharmonicity of the transmon, therefore the frequency of a single photon contributing is $\omega_\mathrm{gf}/2 < \omega_\mathrm{q}$. By fitting eq. 2.26 to the curve of ω_q, we find a maximum qubit frequency of $\omega_{\mathrm{q},0}/2\pi = (9.010 \pm 0.001)\,\mathrm{GHz}$ and a periodic tuning of the qubit frequency with $I = 414\,\mu\mathrm{A}$. Using the known SQUID-area $300\,\mu\mathrm{m}^2$, we can determine the applied external magnetic flied bias of the coil to $112\,\mathrm{mT/A}$. The difference in frequency between the qubit frequency ω_q and the two-photon process ω_gf gives information about the anharmonicity $\alpha = \omega_\mathrm{gf}/2 - \omega_\mathrm{ge}$.The lower panel of fig. 5.2b) shows the anharmonicity for all coil currents with both visible transitions. A slight deviation at $I_\mathrm{coil} = 100\,\mu\mathrm{A}$ and $170\,\mu\mathrm{A}$ can be observed. Averaging over all flux points leads to $\alpha/2\pi = (-187 \pm 6)\,\mathrm{MHz}$. With knowledge of $\omega_\mathrm{q}(\Phi)$, it is additionally possible to extract the qubit-resonator coupling g from avoided crossings as in fig. 5.1a). For this we conveniently rewrite the transition energy $\omega_\mathrm{dressed} = E_{0,\pm}/\hbar - E_{0,\mathrm{g}}/\hbar$ from the Jaynes-Cummings ground state

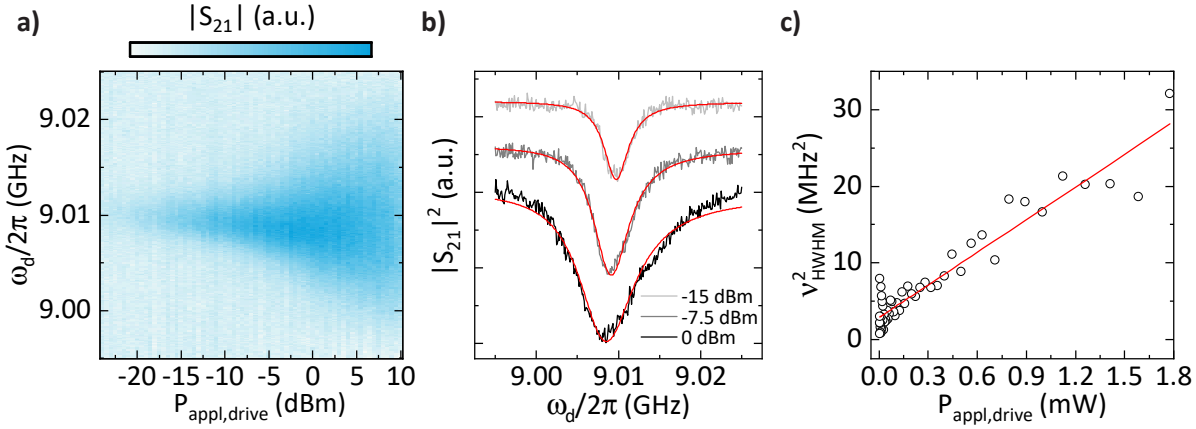

Figure 5.3: Drive-power dependence of the qubit linewidth. **a)** Normalized transmission magnitude $|S_{21}|$ of the probe tone ($\omega_{\text{probe}} = \omega_{\text{r}}$) as a function of drive tone power and frequency. **b)** Slices of the squared normalized transmission magnitude $|S_{21}|^2$ at different drive powers with Lorentzian fits (eq. 5.4). The individual slices are shifted vertically for better visibility. **c)** Power-dependent qubit linewidth extracted from Lorentzian fits in b). The red line is a linear fit yielding an extrapolated qubit linewidth at zero drive power of $\gamma_{\text{q}}/2\pi = 1.70\,\text{MHz}$.

$|0, g\rangle$ in eq. 2.21 to the dressed states $|0, \pm\rangle$ in eq. 2.20 as

$$\omega_{\text{dressed}} = \frac{1}{2}(\omega_{\text{r}} + \omega_{\text{q}}(\Phi)) \pm \frac{1}{2}\sqrt{4g^2 + \delta^2} \tag{5.1}$$

Fitting eq. 5.1 to the dressed state frequencies in the anticrossing of fig. 5.1a) (see panel c) of fig. 5.2) with known $\omega_{\text{q}}(\Phi)$ and ω_{r} (dashed lines) reveals a coupling strength $g/2\pi = (44.4 \pm 0.9)\,\text{MHz}$.

Additionally to the anharmonicity and the coupling strength to the resonator, the internal linewidth γ_{q} is an important qubit parameter as it is directly related to the dephasing rate [23]. Fig. 5.3a) shows the normalized transmission data of the probe tone probing the microwave resonator at resonance ω_{r} in dependence of the applied qubit drive power and frequency for continuous qubit drive. The drive frequency range, in which a qubit response is visible in the drive tone, broadens with increasing power. The probability P_{e} of finding the qubit in the excited state has a Lorentzian shape [23]

$$P_{\text{e}} = \frac{1}{2}\frac{\Omega_{\text{R}}^2}{\gamma_1\gamma_2 + \delta\omega^2\gamma_1/\gamma_2 + \Omega_{\text{R}}^2}, \tag{5.2}$$

where Ω_{R} is the Rabi frequency, γ_1 and γ_2 are the decay and decoherence rates of the qubit and $\delta\omega = \omega_{\text{d}} - \omega_{\text{q}}$ is the drive tone detuning. The FWHM of this Lorentzian is given by the qubit linewidth

$$\gamma_2 = 2\sqrt{\gamma_2^2 + \Omega_{\text{R}}^2\gamma_2/\gamma_1}. \tag{5.3}$$

Therefore, the intrinsic decoherence rate γ_2 is given by the linear extrapolation of the square of the half-width at half-maximum (HWHM, equals FWHM/2) ν_{HWHM}^2. In order to extract the linewidth of the qubit response, we fit a well-establish Lorentzian function [97] to the readout spectrum at various powers in fig. 5.3a). The used Lorentzian function additionally accounts for

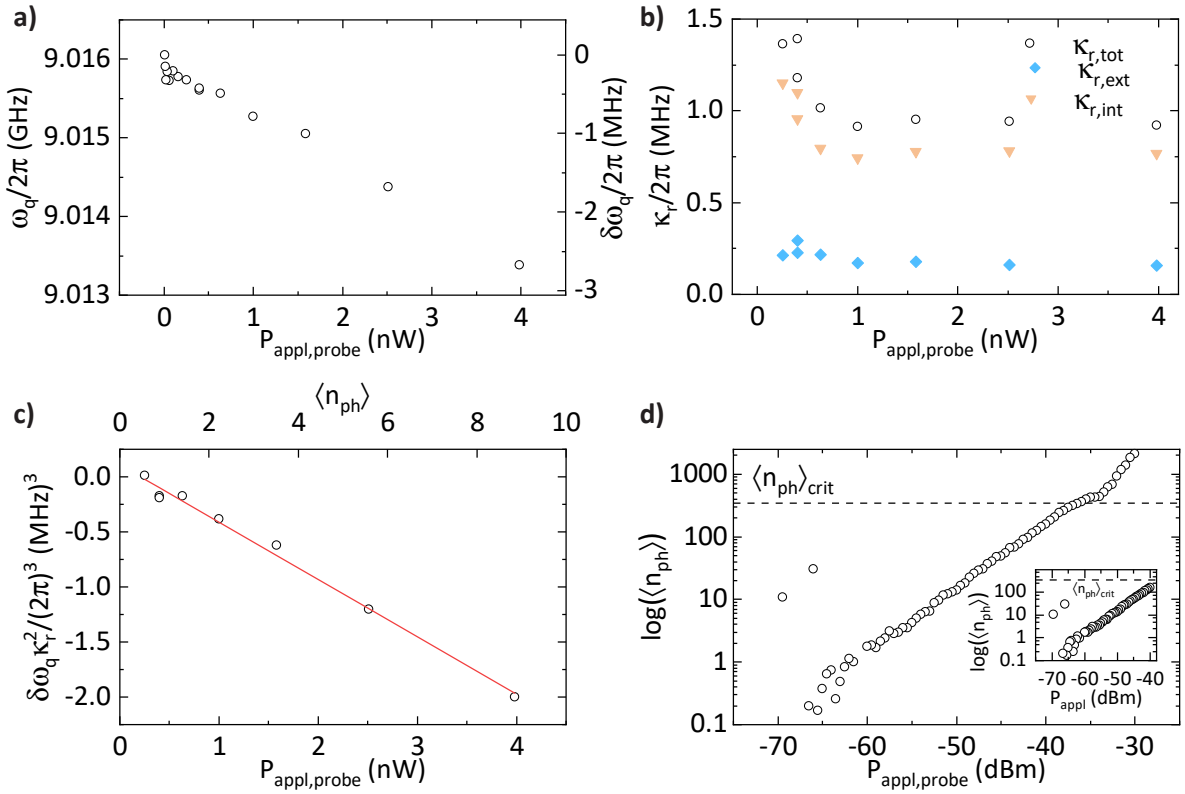

Figure 5.4: **a)** Qubit frequency ω_q and change of qubit frequency $\delta\omega_q = \omega_q(P) - \omega_q(P \to 0)$ as a function of the applied probe tone power $P_{appl,probe}$ at the microwave source output. Higher probe powers, i.e. more photons in the readout resonator, lead to a lower transition frequency due to the AC-Stark shift. **b)** Loss rates of the readout resonator depending on the power. For low probe powers unsaturated two-level systems lead to increased losses. $\kappa_{r,e}$ is roughly constant as expected. **c)** Linear fit to $\delta\omega_q\kappa_r^2$. With known α, δ, g and $\kappa_{r,e}$ the attenuation $\Lambda = -76.2$dB can be extracted. **d)** Calibrated average photon number $\langle n_{ph} \rangle$ in the readout resonator. Above $\langle n_{ph} \rangle_{crit}$ the dispersive regime breaks down. Inset shows photon numbers for lower powers.

a complex background and is given by [97]

$$|S_{21}|^2 = 1 - \left| ic_1 + \frac{\sqrt{\gamma_{q,ext}\gamma_q}/2}{\gamma_q/2 + i(\omega_d - \omega_q)} \right|^2 + c_2, \tag{5.4}$$

and exemplary fits are shown in fig. 5.3b). For high powers, the qubit linewidth is dominated by power broadening while for low powers it converges towards its intrinsic linewidth $\gamma_q = 2\gamma_2$. A linear fit to ν^2_{HWHM} in fig. 5.3c) determines the decoherence rate γ_2 of the qubit to $\gamma_2/2\pi = (1.70 \pm 0.10)$MHz equaling $T_2 = 2\pi/\gamma_2 = (588 \pm 35)$ns. Since $\gamma_q = 2\gamma_2$ for negligible power broadening, this means that we are in the strong coupling regime where $g > \kappa_r, \gamma_q$.

5.1.3 Photon Number Calibration

As the effective coupling strength between the qubit and the resonator scales with the photon number via $g_{\mathrm{eff}} = g\sqrt{n+1}$, we have to discuss the influence of a large photon number in the resonator. During derivation of eq. 2.22, we expanded the exact Jaynes-Cummings Hamiltonian of eq. 2.17 in terms of g/δ. As a result, we find a resonator dependent pull of the qubit frequency when rearranging eq. 2.22 to

$$\hat{H}_{\mathrm{JC}}/\hbar = \omega_{\mathrm{r}}\hat{a}^{\dagger}\hat{a} + \frac{1}{2}\left[\omega_{\mathrm{q}} + 2\chi\left(\hat{a}^{\dagger}\hat{a} + \frac{1}{2}\right)\right]\hat{\sigma}_{\mathrm{z}}. \tag{5.5}$$

With this form, we find the qubit to undergo an AC-Stark shift of $2\chi\langle n_{\mathrm{ph}}\rangle$ caused by the mean photon occupation $\langle n_{\mathrm{ph}}\rangle$ of the readout resonator. Additionally, the photon number statistics of the occupancy $\hat{a}^{\dagger}\hat{a}$ lead to an inhomogeneous line broadening of the qubit [23]. Therefore, a photon number calibration is needed to have insight on the resonator occupancy depending on the probe power. As the photon number in a microwave resonator is given by eq. 2.44, this can be challenging due to insufficient knowledge of the exact attenuation Λ from the microwave source to the sample and the external coupling rate κ_{ext} of the resonator to the transmission line [69]. However, we can make use of the AC-Stark shift of the qubit to quantify the photon number with the following measurements.

Depending on the probe tone power at the microwave source output, we measure the resonant qubit frequency and the linewidth of the readout resonator (fig. 5.4a) and b)). For higher readout powers we see a decrease in the qubit frequency according to the AC-Stark shift for a transmon [69]

$$\delta\omega = 2\frac{g^2}{\delta}\frac{\alpha}{\alpha+\delta}\langle n_{\mathrm{r}}(\kappa)\rangle. \tag{5.6}$$

For this experiment, we configure the qubit at the so-called sweet spot ($I_{\mathrm{coil}} = 135\,\mu\mathrm{A}$, see fig. 5.2b)) which is in the dispersive regime with a qubit frequency $\omega_{\mathrm{q}}/2\pi \approx 9\,\mathrm{GHz}$ (see fig. 5.4a)), far detuned from the resonator frequency $\omega_{\mathrm{r}}/2\pi = 7.213\,\mathrm{GHz}$ with $\delta \approx 2\pi \times 1.8\,\mathrm{GHz} \gg g$. For a microwave resonator probed on resonance the average photon number is given by eq. 2.44

$$\langle n_{\mathrm{r}}\rangle = \frac{2P_{\mathrm{appl}}}{\hbar\omega_{\mathrm{r}}\kappa_{\mathrm{r}}^2}\Lambda\kappa_{\mathrm{r,e}}. \tag{5.7}$$

Λ denotes the attenuation from the signal source to the sample. As expected the internal loss rate $\kappa_{\mathrm{r,i}}$ increases with decreasing power as more two-level systems present on the sample are not saturated by the probe tone. We can now linearly fit the product $\delta\omega_{\mathrm{q}}\kappa_{\mathrm{r}}^2$ in panel c) using the data points where we know both $P_{\mathrm{appl,probe}}$ and $\kappa_{\mathrm{r,e}}$. The resulting slope can be used to extract $\Lambda = (-76.2 \pm 0.9)\,\mathrm{dB}$. The attenuation of the input line driving the microwave resonator is about 14 dB higher than expected from the total attenuation given by the attenuators placed in the system of $-52\,\mathrm{dB}$ and $-9.9\,\mathrm{dB}$ [80] cable losses. Most likely the attenuation in the cryostat is higher than recorded due to a wrongly labeled attenuator. With this constant value of Λ and a constant $\kappa_{\mathrm{r,e}}$ as visible in panel b) we can now state the average photon number depending on the probe power as shown in panel d). The critical photon number, above which the dispersive regime breaks down [69], $\langle n_{\mathrm{ph}}\rangle_{\mathrm{crit}} = \delta^2/2g^2 = 346$ is reached at about $P_{\mathrm{appl}} = -36\,\mathrm{dBm}$.

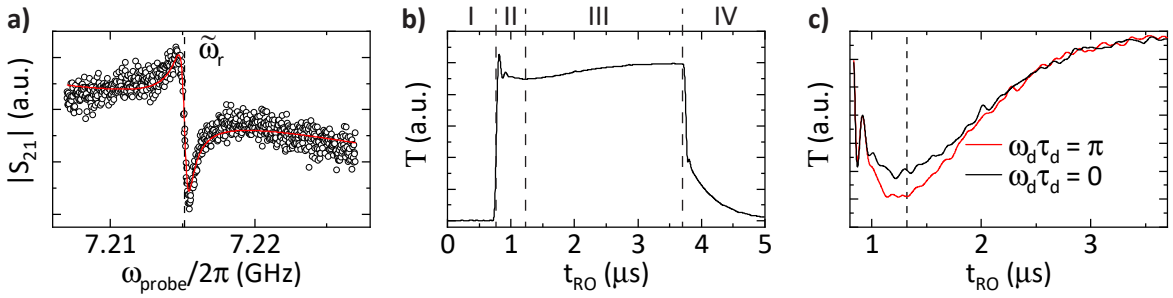

Figure 5.5: **a)** Transmitted microwave signal $|S_{21}|$ through the sample transmission line as a function of the probe tone frequency ω_{probe} around the resonance of a CPWR at resonance frequency $\widetilde{\omega}_{\text{r}}$. The red line is a complex lorentzian fit to the data. For time domain measurements, the response of the resonator at frequency $\widetilde{\omega}_{\text{r}}$ is measured and depends on the qubit state. **b)** Typical time trace of the transmitted signal T for a driven qubit measurement. The individual time sections I-IV are explained in the main text. All shown time-domain data is averaged over 10^6 single-shot measurements. **c)** Two time traces starting at the readout pulse onset are shown. The resonator response is different for measurements without qubit drive (black) versus a π-pulse drive (red) due to the dispersive shift.

5.1.4 Time Domain Measurements

In contrast to frequency spectroscopy time domain measurements capture the dynamics of the investigated system and allow for direct access to information such as lifetime T_1 and coherence time T_2. In this section we will investigate different pulse schemes shown in fig. 2.8d). All measurements shown are conducted using the setup discussed in sec. 4.1.2 and applying 8 dBm drive power and -40 dBm readout power, corresponding to an average photon number $\langle n_{\text{ph}} \rangle \approx 160$, with a pulsed readout scheme.

Driven Rabi oscillations with different pulse lengths and driving frequencies give information about the resonance frequency of the qubit as well as durations for π- and $\pi/2$-pulses needed to invert the qubit state or bring it to the equatorial plane of the Bloch sphere. This knowledge will be used for inversion measurements (allowing to extract T_1) and Ramsey/spin-echo protocols that reveal T_2.

5.1.4.1 Data Acquisition for Time Domain Measurements

We start by discussing the data acquisition and analysis for pulsed time domain measurements and mainly focus on the readout; the description of different pulse sequences can be found in 2.4.4. Applying a microwave pulse sequence leads to a rotation of the qubit state vector on the Bloch sphere. After the drive pulse manipulated the qubit state, we read the state in the computational basis $\{|e\rangle, |g\rangle\}$ via the readout resonator. This is done by probing the resonator at the resonance frequency $\widetilde{\omega}_{\text{r}} = \omega_{\text{r}} - \chi$ found with the qubit in the ground state $|g\rangle$. We use a complex Lorentzian fitting function integrated in the measurement software to extract the resonance frequency. Fig. 5.5a) shows the signal transmission as a function of frequency around the resonance frequency $\widetilde{\omega}_{\text{r}}$. The dashed line is the extracted frequency at which the

system will be probed for all time domain measurements[2]. Note, that the probe frequency is not at the minimal transmission but at a frequency with a very large slope in the transmission spectrum. Therefore, minimal shifts of the resonance frequency can be detected. If the qubit is in the excited state $|e\rangle$, the eigenfrequency of the AC-Stark shifted resonator differs from $\widetilde{\omega}_\mathrm{r}$ by 2χ (c.f. 2.4.4). This leads to a different amplitude of the resonator response and therefore a change in the transmission signal. In combination with fig. 2.5c), we expect a decrease in the transmission signal if the qubit is in state $|e\rangle$ for positive detuning $\delta > 0$. Since time domain measurements will be conducted with a heterodyne detection setup instead of a VNA measurement as in the frequency domain, we will denote the measured signal with T instead of S_{21}.

A typical time trace measured with the used setup is shown in fig. 5.5b). Each single time trace consist of around 10^6 averaged measurements. The timing between the applied readout pulse and the start of the data acquisition is set such that the digitizer card records a few hundred nanoseconds before reading out the qubit (region I). Following a quick initial signal transmitted through the chip (region II), the resonator starts to ring-up (region III). At the beginning of the ring-up, much of the signal is coupled into the resonator leading to a decreased transmission. On the timescale of its coupling to the transmission line $\kappa_\mathrm{r,e}$, the resonator is filled with photon and saturates. After the readout pulse ends, the ring-down behavior of the resonator can be ssen accordingly (region IV).
In panel c) of fig. 5.5, the ring-up of the resonator for a preceding π-pulse (red) and no drive pulse (black) is shown. Clearly, the response of the resonator depends on the qubit state: In comparison to the transmitted signal for no qubit drive (black, qubit in $|g\rangle$), a π-pulse (red, qubit in $|e\rangle$) leads to a stronger absorption of photons by the resonator. This matches the expected behavior as discussed for panel a). Since each trace is the average of many measurements - each measurement yielding either $|g\rangle$ or $|e\rangle$ for the qubit state - we can map the transmission amplitude to the probability of finding the qubit in the excited state. For our experiments, we fit the ring-up of the resonator with an exponential $\mathrm{T} \propto A\exp(-\kappa t_\mathrm{RO})$ beginning at the dashed line in c) and analyze the resulting amplitude A.

5.1.4.2 Rabi & Lifetime Measurements

In order to investigate the qubit dynamics for different excitation pulses, we perform Rabi sequences (fig. 2.8d)) with varying pulse durations τ_d and drive frequencies ω_d. Analyzing the resulating time traces in the previously described manner, we find oscillating transmission amplitudes as depicted in fig. 5.6 in the left panel. As the Rabi frequency $\Omega_\mathrm{R}^2 = \epsilon_\mathrm{d}^2 + \delta^2$ at which the qubit population oscillates scales with the detuning $\delta = \omega_\mathrm{d} - \omega_\mathrm{q}$ and the drive amplitude ϵ_d, a faster oscillation of the transmitted signal is visible for off-resonant drive. The resonance frequency of the qubit is found at the qubit drive frequency ω_d with the longest Rabi oscillation period such that $\omega_\mathrm{d}\tau_\mathrm{d} = (2n+1)\pi$, $n \in \mathbb{N}$ indicated by the dashed line. However, this is in contrast to the expected constant qubit frequency ω_q for which the line would be vertical (c.f. fig. 1 of Ref. [98]). Instead, we see an increasing qubit frequency as a function of the pulse length τ_d. We explain this behavior by a finite overlap t_o of the drive and readout pulse (fig. 5.6 right

[2]This calibration is done before each individual measurement to account for deviations.

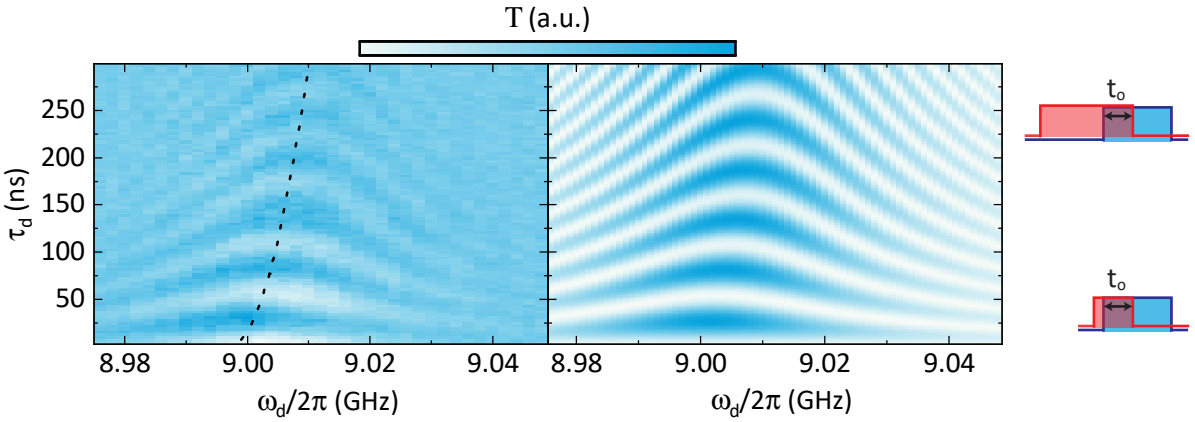

Figure 5.6: Left: Rabi measurements for different pulse lengths τ_d and drive frequencies ω_d. The color-coded transmission displays the probability of finding the qubit in the excited state. The dashed line indicates the qubit resonance frequency for different pulse lengths, a non-typical drift is visible. Middle: Numerical calculation of pulsed Rabi sequences with a finite overlap t_o of the drive and readout pulse to replicate the measurement. No loss is included. Right: Schematic pulse sequence to illustrate the overlap. For varying pulse length (red), the overlap stays constant due to the measurement setup. Timescales are not to scale.

schemes). For short τ_d, most of the drive pulse overlaps with the readout pulse such that the qubit frequency is strongly influenced by the ring-up of the resonator and the consequent AC-Stark shift $2\chi\langle n_\mathrm{ph}\rangle$. Since χ is negative for transmons (eq. 2.27), the qubit resonance frequency is effectively decreased. For longer drives, most of the qubit rotation takes place without any disturbance by the resonator leading to higher qubit frequency in the absence of an AC-Stark shift.

We verify this explanation by numerically solving the Schrodinger equation with a modified Rabi Hamiltonian in the rotating frame similar to eq. 2.32:

$$\widetilde{H}(t)/\hbar = \frac{1}{2}\begin{pmatrix} -\left(\omega_\mathrm{d} - \omega_\mathrm{q}(t)\right) & \epsilon_\mathrm{d} \\ \epsilon_\mathrm{d} & \left(\omega_\mathrm{d} - \omega_\mathrm{q}(t)\right) \end{pmatrix}. \tag{5.8}$$

Here, the qubit frequency $\omega_\mathrm{q}(t)$ is now time-dependent as the photon population of the resonator and therefore the AC-Stark shift on the qubit vary over time. Due to the pulse overlap the readout resonator will start to be populated for a time t_o before the drive pulse ends. The changing photon number[3] in the resonator results in a time-dependent AC-Stark shift of the qubit frequency. The numerical calculation shows the same behavior of a drifting qubit frequency as the measurement. Since there is no decoherence channel implemented the signal stays equally strong for longer pulse times. More information on the calculation can be found in appendix A.2.

By further investigation of panel a) we want to find the duration of a π-pulse on resonance. Due to the dispersive shift the signal T at the digitizer card is proportional to the probability P_e of finding the qubit in the excited state. We can therefore write the transmission similarly to eq.

[3]The applied readout power of $P_\mathrm{appl} = -40\,\mathrm{dBm}$ equals an average photon number of $\langle n_\mathrm{ph}\rangle = 160$.

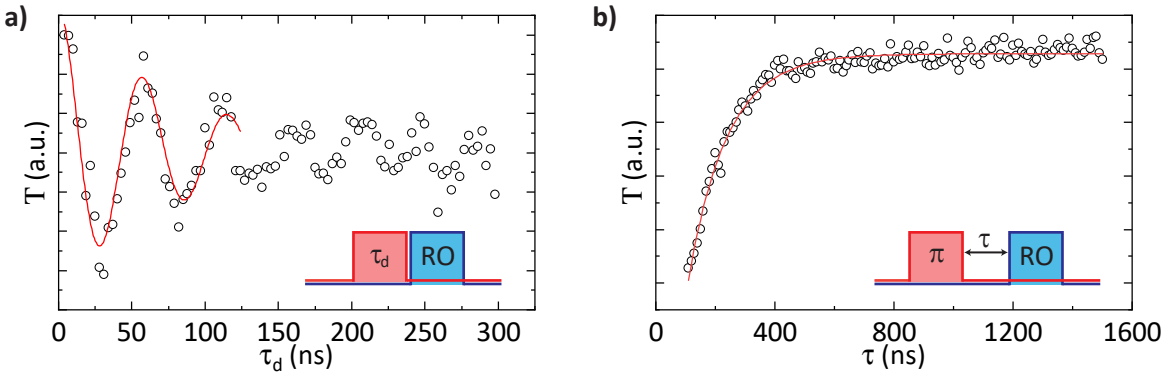

Figure 5.7: a) Time evolution of the transmitted signal at fixed drive frequency $\omega_d/2\pi = 9.000\,\mathrm{GHz}$ as a funtion of drive pulse length τ_d, corresponding to a slice along the dashed line in fig. 5.6a) and fit following eq. 5.9. The initial π-pulse of the Rabi sequence (inset) inverts the qubit state and therefore changes the signal T from maximal at $\tau_d = 0$ to minimal at $\tau_\pi = 28.9\,\mathrm{ns}$. **b)** Inversion recovery measurement. For longer wait times τ betwen π-pulse and readout (inset) the qubit relaxes to its ground state, increasing T. The exponential fit yields $T_1 = 129\,\mathrm{ns}$.

2.36 as

$$\mathrm{T} \propto \sin^2\left(\frac{\Omega_R \tau_d}{2}\right) \times \exp\left(-\gamma \tau_d\right), \tag{5.9}$$

with $\Omega_R = \sqrt{(\omega_d - \omega_q)^2 + \epsilon_d^2}$ being the Rabi frequency. To cope for the decreasing amplitude due to decoherence effects, we introduce an exponential factor with decay rate γ. Fitting this modified equation to a slice along the resonance frequency for short pulses ($\omega_d/2\pi = 9.000\,\mathrm{GHz}$) reveals the typical Rabi osciallation in fig. 5.7a). From the fit we find $\tau_\pi = \pi/\Omega_R = (28.9 \pm 0.4)\,\mathrm{ns}$. With known τ_π we can perform inversion recovery measurements. As drive frequency we select $\omega_d/2\pi = 9.012\,\mathrm{GHz}$ as this seems to be the qubit frequency for long drive pulses in fig. 5.6a) and therefore as previously discussed the resonance frequency in absence of an AC-Stark shift[4]. To minimize problems with overlapping pulses we start with a minimal pulse spacing τ (see fig. 5.7b) inset) of 110 ns after the pi pulse with $\tau_{\pi,\mathrm{used}} = 28\,\mathrm{ns}$. Note that the pulse is not exactly the same as extracted above due to an error at the time of the measurements. This does not influence the inversion measurement since the qubit decay will be exponential and therefore the rate of decay is not dependent on the initial state. The signal T shown in panel b) of fig. 5.7 is again proportional to P_e, an exponential fit leads to a qubit lifetime of $T_1 = (129 \pm 12)\,\mathrm{ns}$.

5.1.4.3 Ramsey & Spin-Echo Measurements

Additionally to the qubit lifetime T_1 we want to determine the decoherence time T_2. A detailed discussion of Ramsey and spin-echo sequences can be found in sec. 2.4.2.
We start with a Ramsey measurement following the pulse scheme in fig. 2.8d) and a pulse length of $\tau_{\pi/2} = 14\,\mathrm{ns}$. As discussed for the inversion measurement, perfect timing of the pulse length is not crucial since it will only affect the signal strength as two $\pi/2$-pulses might not lead to a

[4] Figure 5.6b) was recorded at a later point in time with a slightly different flux suchs that the resonance frequency here is also slightly different.

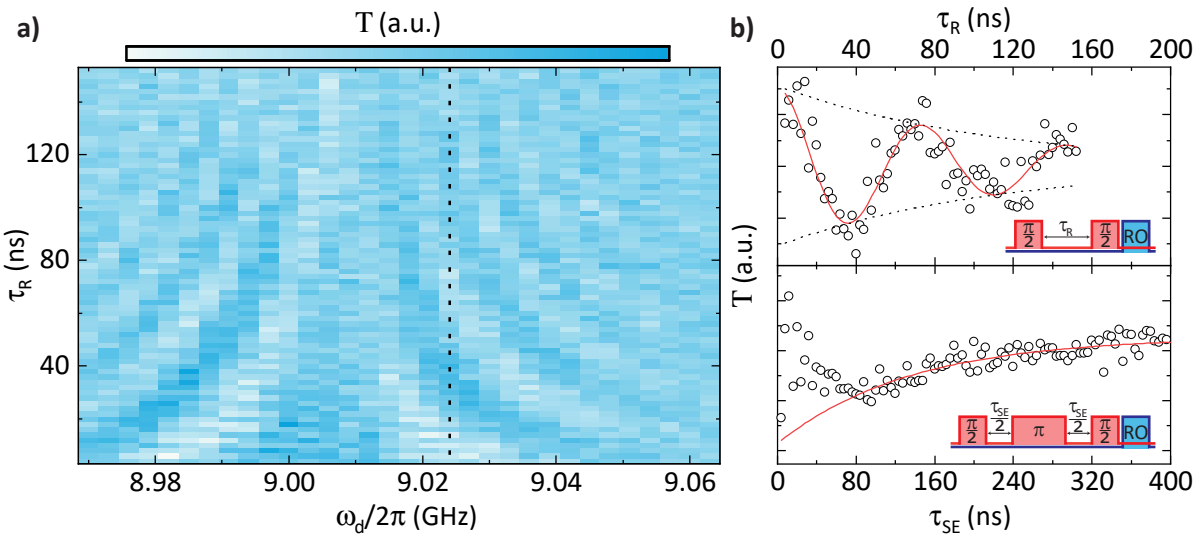

Figure 5.8: Measurements to determine T_2 and T_ϕ. **a)** Ramsey sequence with varying drive frequencies ω_d and pause lengths τ_R. Two $\pi/2$-pulses are seperated by τ_R. For off-resonant drives a beating in the qubit state probability is visible, its exponential decay reveals $T_{2,\mathrm{R}}$. **b)** Upper panel: Slice through a) along the dotted line. The beating in the transmission has a frequency $\Delta\omega = \omega_\mathrm{d} - \omega_\mathrm{q}$ and oscillates sinusoidally (red line fit). The dotted line fit is the enveloping exponential decay. Lower panel: Spin-Echo measurement as an alternative method to extract T_2. For data points for $\tau_\mathrm{SE} < 80\,\mathrm{ns}$ the main decoherence takes place during the drive pulses, they are therefore excluded from the fit. Insets show pulse sequences, pulse lengths are not to scale.

complete flip of the qubit state, but the decoherence mechanisms remain unaffected. Fig. 5.8a) shows Ramsey fringes by sweeping the wait time τ_R for different drive frequencies ω_d. After the first pulse the qubit starts rotating on the Bloch sphere around the z-axis with $\Delta\omega = \omega_\mathrm{d} - \omega_\mathrm{q}$ [49]. In the absence of decoherence the second drive pulse populates the excited or ground state for $\Delta\omega\tau_\mathrm{R} = n\pi$ with n even or odd, respectively. This oscillation can be seen in the upper panel of fig. 5.8b). Decoherence (and decay) mechanisms lead to a reduced probability of finding the qubit in the exited state, therefore an exponential decay indicated by the dotted lines is visible in the signal. The fit yields a detuning from the resonance frequency of $\Delta\omega/2\pi = (13.5 \pm 0.2)\,\mathrm{MHz}$ with $\omega_\mathrm{d} = 9.024\,\mathrm{GHz}$ resulting in $\omega_\mathrm{q} = 9.011\,\mathrm{GHz}$ which is close to the assumed resonance frequency for the previous inversion measurements. From the decay rate we can extract a Ramsey coherence time of $T_{2,\mathrm{R}} = (108 \pm 23)\,\mathrm{ns}$.

A better approach to get the true decoherence time T_2 is the spin-echo measurement as this sequences filters low-frequency noise by inverting the qubit state with a π-pulse after half the wait time $\tau_\mathrm{SE}/2$. For this measurement the qubit is driven on resonance. Since the sum of all pulses is a multiple of 2π the expected qubit state for $\tau_\mathrm{SE} = 0$ is $|g\rangle$ while for longer wait times the state should approach a mixed state $(|g\rangle\langle g| + |e\rangle\langle e|)/2$ due to dephasing.

As long as $\tau_\mathrm{SE} < 2\tau_\pi$ the main contribution to decoherence happens during the drive, which leads to a much more complex behavior, so we exclude these data points from the fit. Longer

Table 5.1: Important system parameters for the investigated qubit-resonator system.

System Parameter	Variable	Value
Resonator frequency	$\omega_r/2\pi$	7.213 GHz
Resonator loss rate	$\kappa_r/2\pi$	(885 ± 38) kHz
Coupling rate	$g/2\pi$	(44.4 ± 0.9) MHz
Qubit frequency	$\omega_q/2\pi$	(9.010 ± 0.001) GHz
Qubit linewidth	$\gamma_q/2\pi$	(3.40 ± 0.20) MHz
Anharmonicity	$\alpha/2\pi$	(-187 ± 6) MHz
Lifetime	T_1	(129 ± 12) ns
Ramsey coherence time	$T_{2,R}$	(186 ± 82) ns
Spin-echo time	$T_{2,SE}$	(133 ± 44) ns

pulses show an exponential change in transmission from low (equaling $|g\rangle$) to higher values of T. Fitting an exponential decay of form $\exp(-\tau_{SE}/T_{2,SE})$ to the data results in $T_{2,SE} = (133 \pm 44)$ ns.

The decoherence time T_2 is a combination of both qubit energy decay characterized by T_1 and pure dephasing on a timescale of T_ϕ

$$T_2^{-1} = (2T_1)^{-1} + T_\phi^{-1} \tag{5.10}$$

Our result corresponds to a limitation of the qubit coherence by dephasing as $T_2 \approx T_1$ is not limited by the lifetime. Following the discussion of the filter functions from Ramsey and spin-echo measurements in sec. 2.4.2, the result $T_{2,R} > T_{2,SE}$ suggests that there is a dominating high-frequency noise source for our measurement setup.

5.1.5 Discussion

All important figures of merit measured and calculated in this section can be found in table 5.1.

For a readout resonator the ideal case would be a higher external loss rate such that the ring-up time $\tau \propto \kappa^{-1}$ of the resonator is minimized. This could be achieved by further reducing the distance between the resonator and transmission line and increasing the coupling length.

We find a detuning of qubit and resonator $\delta = \omega_q - \omega_r \approx 2\pi \times 1.8\,\text{GHz} \gg g$ when working at the sweet spot such that we operate in the dispersive regime.

Furthermore, the system resides well in the strong coupling regime since $g > \kappa_r, \gamma_q$ such that we can observe the vacuum Rabi splitting of the dressed states $|g, 1\rangle$ and $|e, 0\rangle$ (fig. 5.2b). The coupling g between the qubit and readout resonator is on the order of magnitude that is expected from the design by simulations. For an exact prediction, we would need more information on the critical current I_c and capacitance C_J of the Josephson junctions due to the dependence of g on the Josephson energy E_J and charging energy E_C in eq. 2.25.

The value for the anharmonicity $\alpha/2\pi = -183$ MHz is typical for transmon qubits [69, 57]. We find a dispersive shift of $\chi/2\pi = 100$ kHz (eq. 2.27) per photon occupying the resonator at the working point at the maximum qubit frequency $\omega_q/2\pi = 9.01$ GHz.

Considering the linewidth κ_r of the resonator, the transmission through the transmission line does not change as drastically for a different qubit state as depicted in fig. 5.5a), however it is

enough to distinguish between different qubit states.

The dephasing rate measured from drive power broadening suggests a decoherence time of $T_2 = 2\pi/\gamma_2 = 590\,\text{ns}$. Time domain measurements, however, determine a maximum decoherence time $T_{2,\text{R}} = 186\,\text{ns}$ and a qubit lifetime $T_1 = 129\,\text{ns}$. The large discrepancy is unexpected, especially as the frequency domain measured T_2 does not follow $T_2 \leq 2T_1$. Additionally, the large uncertainty of the qubit lifetime and coherence time is most likely due to the long ring-up time of the readout resonator in comparison to the characterisitc qubit times, making precise measurements difficult. To this end, we cannot explain the deviation and further careful investigations are required to resolve this matter. The unfavorable readout resonator coupling might play a crucial role for time domain measurements, future adaptions to the sample design will focus on increasing the coupling rate and therefore decreasing the ring-up time of the resonator, making the time traces easier to evaluate. The ovservation that $T_{2,\text{R}} > T_{2,\text{SE}}$ suggests, that we have a dominant high-frequency noise present in our setup which seems to have a larger impact on dephasing mechanisms. This conclusion originates from the noise filter functions, which are related to the Ramsey and Hahn-echo sequence (see fig. 2.9).Dephasing can be caused by flux noise, i.e. a slight change in the transmon frequency. Earlier work [80] found that already slight detuning off the "sweet-spot", where the transmon frequency-flux relation has zero slope, can drastically decrease the coherence of the system. Further instabilities from current sources or imperfect magnetic shielding could strengthen the effect, however these effects can be ruled out for our measurement setup most likely.

Next, we identify some of the most likely detrimental effects on the qubit coherence and discuss possible remedies for the future. Residue resist at the junction area, as visible in fig. 3.4, can introduce additional two-level systems [86]. The qubit can interact with these, causing decoherence. Additionally, the Dolan bridges used to fabricate Josephson junctions are a bottleneck in the fabrication step. They are always at risk to leave resist residues and tend to undergo deviations in size. Futhermore, we currently have to use the SUPERBOWL-system, a magnetron-sputter chamber, to conduct the bandaging process described in sec. 3.2.2. Scanning electron microscope images show that the sputtered aluminum has a bigger grain size and worse cristallinity than evaporated Al. The system is also used to sputter AlN, a piezoelectric material that could cause conversion of electrical energy in the qubit to mechanical strain if deposited on the sample.

We are confident that all of the above issues can be resolved by transferring the fabrication process to the new evaporation system. The Plassys evaporation system enables an oxygen descuming in the load lock to clear small resist residues. Aditionally, the system allows for rotations along two axes, enabling the fabrication of patch-integrated cross-type bridges as demonstrated in Ref. [99] instead of Dolan bridges. Lastly, the evaporation system has a built-in argon-ion gun such that the bandaging process can be conducted in there as well, enabling the usage of a single evaporation system for all fabrication steps without the risk of contaminating the sample with spurious materials.

Lastly, no surface treatment has been performed on the investigated chip before fabricating the structures. This limits the film cristallinity due to native SiO_x on the wafer surface. Newly introduced cleaning steps like Piranha and HF-dips remove the oxide layer and lead to less losses at the interfaces of the substrate. These fabrication steps are well-established and known to decrease contaminants and oxides at the substrate surface [100, 101].

5.2 Surface Acoustic Wave Resonator Measurements

In this section, we will investigate a 1-port surface acoustic wave resonator (SAWR) on a thin-film lithium niobate substrate (TFLNO) consisting of LNO(500 nm)/SiO_x(2 µm)/Si(350 µm). The lithium niobate layer is a 128°-Y-X cut crystal. This substrate is of particular interest for our approach to cQAD for which we want to combine cQED and SAW elements on a single chip. Ultimately, a stack of silicon and lithium niobate should be used for our on-chip cQAD experiments. The goal is to fabricate SAW devices on the piezoelectric LNO thin-film while qubits will be fabricated on areas where the LNO thin-film has been removed. This provides a low-loss silicon substrate without negative influence of the piezoelectricity on the qubit coherence. Therefore, the behavior of SAWs on thin-film piezoelectric materials has to be understood and quantified. However, due to fabrication difficulties of the LNO/Si stack, we initially investigate the behavior of SAWs on thin-film LNO with the tri-stack consisting of lithium niobate and silicon with an intermediate silicon oxide layer.

5.2.1 Frequency Domain Measurements

5.2.1.1 Free Spectral Range & Single Electrode Reflectivity

We start the investigation of a SAWR depcited in fig. 3.2a) using continuous wave spectroscopy. Fig. 5.9 shows the microwave reflection $|S_{11}|$ as a function of frequency f at $T = 89\,\mathrm{mK}$ when probing the resonator using the setup depicted in fig. 4.3. The Figure shows areas of high reflection ($4.880 - 4.888\,\mathrm{GHz}$ and $4.916 - 4.920\,\mathrm{GHz}$) and low reflection ($4.889 - 4.913\,\mathrm{GHz}$) zones. Prominently, we note two sets of periodic dip pattern with a reduced reflection amplitude (marked with black and red arrows) and a clearly visible central peak signature at $4.902\,\mathrm{GHz}$. Following the discussion in sec. 2.6.3, such minima in the reflection spectrum are one characteristic resonance signature of surface acoustic wave resonators, as they can be associated with the multiple standing wave patterns which can be excited in the SAW resonator. Upon closer inspection, the dips appear to occur in pairs of two (blue dashed box), following two distinct periodicities. Similar double-dip features have been observed in SAWRs by other groups [19, 29] and have been attributed to longitudinal (black arrows) and transversal (red arrows) shear wave modes [29].However, plane longitudinal and transversal modes are not confined to the surface and cannot form SAWs. Therefore, the authors supposedly refer to Rayleigh waves as longitudinal modes and to shear-horizontal waves as transversal modes. Rayleigh and shear-horizontal waves consist of partial longitudinal and shear waves, allowing a confinement to the substrate surface. The phase velocity of shear-horizontal waves is the transversal sound velocity v_t of the substrate [18], therefore a shear-horizontal wave is always faster than a Rayleigh wave as $v_\mathrm{R} < v_\mathrm{t}$. As the frequency of a wave is propotional to the phase velocity, $f \propto v$, faster waves have a higher frequency than slower waves with the same wavelength. Therefore, we identify the higher of the two modes forming a pair (blue box, red arrow) with shear-horizontal waves and the lower mode (blue box, black arrow) with Rayleigh waves. Due to the Fabry-Perot-like nature of the resonator, dips assigned to specific propagation modes are expected to occur with a constant frequency periodicity, the free spectral range (FSR), denoted as ν. Although the vivid background complicates the identification of free spectral modes as some dips are possibly overlapping with

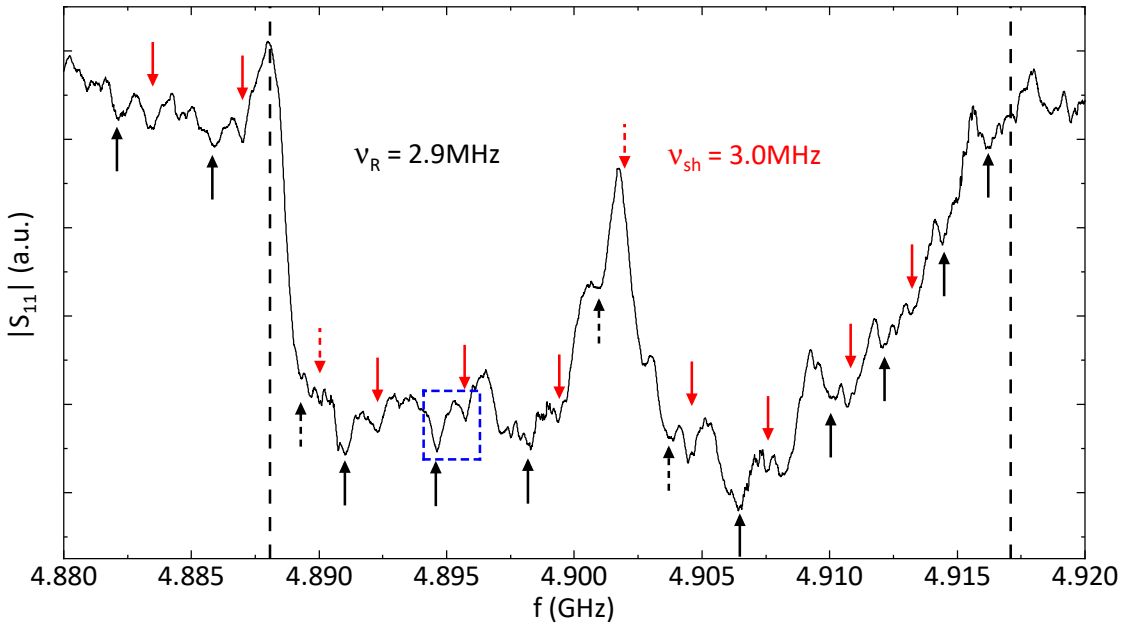

Figure 5.9: Reflection parameter $|S_{11}|$ of a 1-port surface acoustic wave resonator (SAWR) as a function of frequency f. The spectrum features many dips which can be identified as modes of the Fabry-Perot resonator with a free spectral range ν. Black/red solid arrows indicate Rayleigh/shear-horizontal wave modes, respectively. Some modes are not visible (dashed arrows) due to the complex microwave background. Over a range of 30 MHz, a significant decrease of the reflection is observed (dashed lines). This might indicate a grating stop band, allowing the formation of standing wave modes within the resonator.

different features, the approximate position of those absorption dips, extrapolated from the visible modes, is indicated by dashed arrows.

Taking only the identified dips (solid black and red arrows) into account, we linearly fit the frequency of the dips f_{res} as a function of the mode number n according to $f_{\mathrm{res}} = n\nu$. We find a free spectral range $\nu_{\mathrm{R}} = (2.9 \pm 0.1)\,\mathrm{MHz}$ for the Rayleigh waves and $\nu_{\mathrm{sh}} = 3.0\,\mathrm{MHz}$ for the shear-horizontal modes. The FSR of both modes is apparently equal within the uncertainty. For the following analysis, we focus on the more prominent peaks identified as Rayleigh waves. Combining the FSR and the numerically calculated phase velocity of SAWs at 5 GHz on the TFLNO substrate $v_{\mathrm{p}} = 3800\,\mathrm{m/s}$ [46], we can determine an effective cavity length of $L_{\mathrm{C}} = 655\,\mu\mathrm{m}$ using eq. 2.60. From this, we obtain a penetration depth of the SAW into the mirror grating of $L_{\mathrm{p}} = 128\,\mu\mathrm{m}$ (see eq. 2.61). Using eq. 2.62 and the designed electrode width $a = 183\,\mathrm{nm}$, we find a single electrode reflectivity of $|r_{\mathrm{s}}| = 0.14\,\%$.

According to earlier work at mK temperatures by Satzinger et. al on LNO [28], we expect a single electrode reflectivity of a few percent. However, our value is an order of magnitude less. In our experiment, the Bragg mirrors consist of $N_{\mathrm{g}} = 500$ grating lines. If the calculated single electrode reflectivity is correct, we therefore would not reach the high-reflectivity regime discussed in eq. 2.59 for which a strong stop band is visible with unity reflection.

These results are unexpected as it seems unlikely for the single electrode reflectivity to deviate by more than one order of magnitude compared to literature values (c.f. e.g. [28, 30]), given the relative simplicity of the grating structure and the similar substrate. The grating mirrors by Satzinger et al. [28] consists of 25 nm thick Al strips on bulk LNO, such that a comparison to our 100 nm Al on LNO/SiO_x/Si should be feasible. In fact, thicker electrodes should increase the reflectivity due to higher mass loading [18]. Apart from difference of the SAW device structure, we suspect that the spectral behavior of SAWs on TFLNO is quite different to that on bulk LNO. The SAW strains decay on the order of one wavelength ($\lambda_{IDT} = 732\,nm$) into the substrate. Therefore, the phase velocities of the SiO_x layer and probably of the silicon substrate have to be considered as well for the description of a SAW. While it might be possible that the multi-layer substrate changes the reflective behavior of the grating to such great extent, we want to verify this result and therefore compute the reflectivity with an alternative method in the following.

Instead of using the free spectral range to calculate the penetration depth into the mirror, we can use the spectral width of the grating stop band to extract the single electrode reflectivity. The spectrum in fig. 5.9 shows a distinct reduction in the scattering parameter $|S_{11}|$ of about 30 MHz (vertical dashed lines). As examplarily calculated in sec. 2.6.2.2, this is the expected width of a mirror stop band around 5 GHz. To this end however, we have no physical intuition why the reflection should be reduced in the stop band width. In the following, we continue the analysis under the assumption that this feature is indeed caused by a mirror stop band. Eq. 2.57 allows to relate the width of the of the stop band to the single strip reflectivity. Using this approach, we find a single strip reflectivity $|r_s| \approx 1\%$, which is in much better agreement with the reported values of a few percent in other experiments [29, 28, 30] on bulk LNO. With this reflectivity, the penetration depth should be $L_p = a/|r_s| = 18\,\mu m$, corresponding to a FSR $\nu = 4.36\,MHz$, about 50% higher than the experimentally observed value. Alternatively, the larger FSR could be the consequence of a decreased phase velocity of $v_p^* = 2\nu L_C = 2616\,m/s$. However, this value not only contradicts the numerical simulations of Ref. [46], but would also result in a much lower center frequency of the IDT response $f_c^* = v_p^*/\lambda_{IDT} = 3.6\,GHz$. This in turn would strongly suppress the excitation of SAWs at 5 GHz, contradicting our experimental observation.
Unfortunately, we therefore cannot present a consistent picture of the findings presented here.

5.2.1.2 SAW Resonator Quality Factor

By fitting the resonance signatures in the reflection spectrum to eq. 2.64, we can extract the quality factors of the cavity. As opposed to the fits for superconducting microwave resonators (sec. 5.1.1), we cannot use a "circle"-fit method for the SAWR. As illustrated in fig. 4.3, we measure the reflected signal by routing it to an output line via a microwave circulator. However, this alters the reflection coefficient in a way that prohibits the diameter correction method from correctly removing the complex measurement background [102]. We therefore use eqs. 2.63 and 2.64 to fit the region next to dips in the spectrum. Fig. 5.10a) shows the evaluated dips in the spectrum, the dashed boxes indicate pairs of dips from the previous discussion. In panel b), an exemplary fit with eq. 2.64 for dip 2 is shown when probing the system with a microwave

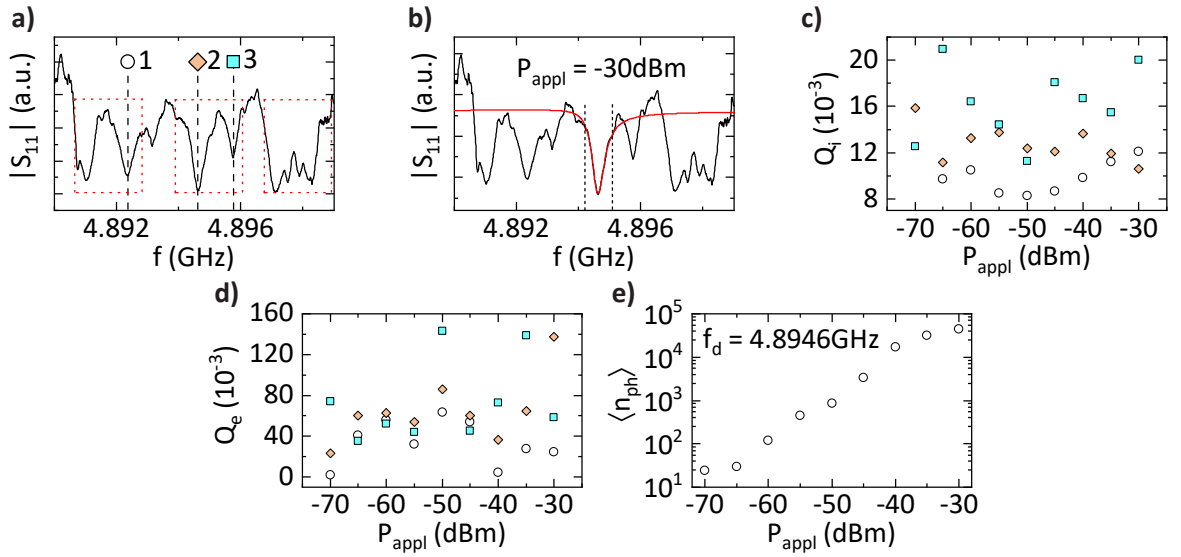

Figure 5.10: Detailed investigation of Fabry-Perot modes. **a)** Zoom into a part of the stop band in fig. 5.9. A double-peak pattern with a complex background is suspected and indicated by dashed boxes. Each mode pair consists of one Rayleigh and one shear-horizontal mode. **b)** Exemplary fit to a single mode with eq. 2.64. The dashed lines show the used data range to exclude the busy background for the fit. **c)** Internal and **d)** external quality factor of the modes as a function of the applied microwave power P_{appl}. The internal quality factor is approximately 1.5×10^4, the external quality factor around 5.0×10^4. For both quantities, a large spread is observed. No error bars are given as the fitting algorithm provides unreasonably large uncertainties. Presumably, the fitting algorithm is not stable enough. **e)** Average phonon number $\langle n_{\mathrm{ph}} \rangle$ in the SAWR depending on the drive power following eq. 2.44 for mode 2 in panel a). For the lowest drive power $P_{\mathrm{appl}} = -70\,\mathrm{dBm}$, the average phonon occupation is 24, so single phonon level is not reached.

power of $-30\,\mathrm{dBm}$ at the source output. We limit the fitting range to a narrow region around the dip minimum (dashed lines) to neglect the dominant background and surrounding dips. For regions outside the fitting range, the fit converges towards a constant maximal reflection value as one would expect for a single mode of the resonator as no energy can be stored in the mode. In panels c) and d), the extracted internal and external quality factors Q_{i} and Q_{e} of the dips labeled in a) are plotted as a function of the applied microwave power. We do not provide error bars as the uncertainties calculate by the fitting algorithm are unreasonable (several orders of magnitude larger). We presume that the algorithm is not very stable for the used fitting functions, improvements (e.g. different fitting algorithms) might be necessary for future evaluations. The internal quality factor for dips 1 and 2 deviate slightly from fit to fit in a range of $Q_{\mathrm{i}} = (8 - 12) \times 10^3$ and $Q_{\mathrm{i}} = (10 - 16) \times 10^3$, respectively. For dip 3, the fit result is not very consistent. This is probably due to the comparably small prominence of the peak in the spectrum. The external quality factors show a large spread around $Q_{\mathrm{e}} = 50 \times 10^3$, therefore the resonator is slightly undercoupled. Most microwave resonators based on superconducting thin films shown an increase in the internal quality factor Q_{i} for higher excitation powers due to saturation of two-level systems and therefore a decreasing resonator loss rate. In the conducted

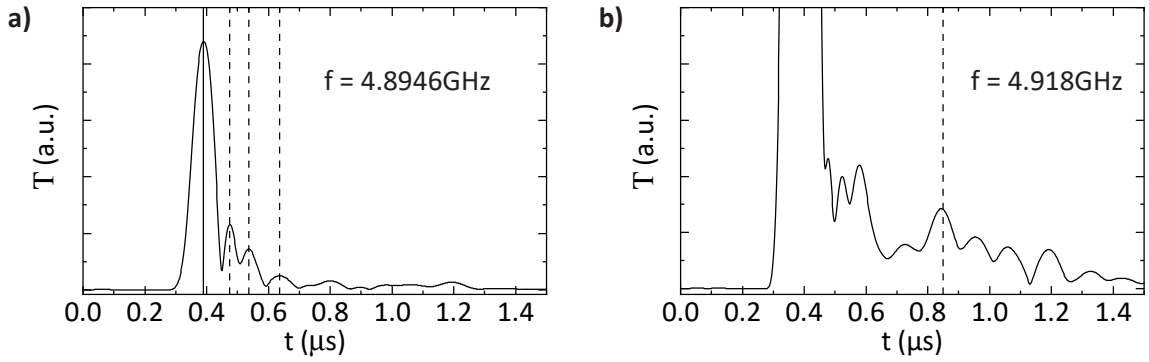

Figure 5.11: Traces of time domain measurements recording a pulsed excitation of the SAWR. Following a 100 ns excitation pulse on resonance with one of the previously identified SAW modes, the reflected microwave signal T is down-converted and digitized. The acquisition is started before the application of the pulse such that the pulse itself is included in the measurement. **a)** Time trace of the Rayleigh mode "2" in fig. 5.10a). The electromagnetically reflected microwave signal (solid vertical line) when applying the pulse is registered at $t = 0.38\,\mu s$ and visible as a large peak in the trace. subsequently, several peaks can be observed (dashed lines). The nature of these peaks is discussed in the main text. **b)** Time trace at $f = 4.918\,GHz$. At this frequency, a distinct peak is observable at $t = 0.85\,\mu s$, 470 ns after the excitation pulse. This might suggest a SAWR response from traveling SAWs transiting the IDT.

measurements, we do not observe a two-level system saturation of the internal quality factor Q_i as reported in Ref. [19]. However, comparing the effective power at the SAWR to Ref. [19] accounting for the attenuation (total $-55\,dB$ from fig. 4.3 with $-9\,dB$ added by microwave lines), one would expect at least to see the onset of the TLS saturation. With eq. 2.44, we can calculate the mean phonon occupancy of a SAW resonator (panel e)) to be $\langle n_{ph} \rangle \approx 24$ for $-70\,dBm$ drive power. For lower drive powers, the signal-to-noise ratio becomes too small to extract qualtiy factors, so no measurements were conducted at the single phonon level.

5.2.2 Time Domain Measurements

Due to the low propagation velocities of SAWs, this specific type of devices are especially suited to be investigated with time domain measurements as our setup (see fig. 4.3) is capable of digitizing the reflected microwave signal with 500 MSamples/s which corresponds to one sample per 2 ns. During this time, a SAW on the TFLNO ($v_p \approx 3800\,m/s$ at $f = 5\,GHz$) travels 7.6 µm. Compared to the effective cavity length of $L_C = 655\,\mu m$, we are able to resolve the propagation of wave packages by recording the electro-mechanical response of the IDT as reported in Ref. [70]. Ideally, such measurements can provide insight into the SAW dispersion as well as the attenuation within the SAWR. In this section, we begin with the investigation of the microwave response of the IDT after a short excitation pulse at various frequencies. Afterwards, we present data on the ring-down behavior of a SAWR after excitation into a steady state.

5.2.2.1 Short Excitation Pulse

A first measurement series is conducted with a drive frequency of $f = 4.8946\,\mathrm{GHz}$ corresponding to the Rayleigh mode labeled as "2" in the spectrum of fig. 5.10a). The SAWR is excited with a 100 ns pulse. Assuming a Gaussian envelope (time-bandwidth product 0.44, ch. 9.1 of[103]), this corresponds to a FWHM of 4.4 MHz in the frequency domain. Therefore, it also nearby resonances can be excited with the short pulse and might lead to contribution of different modes to the time trace. The reflected signal T is down-converted and digitally heterodyned[5] as described in sec. 4.1.2 with the setup shown in fig. 4.3. An exemplary resulting time trace is depicted in fig. 5.11a). Several peaks with decreasing amplitude are visible. The initial peak, marked by a solid vertical line, is the reflected electromagnetic signal, i.e. photons that were not converted into phonons via the IDT. The time offset is due to cable and circuit element delays as well as the recording start settings of the digitizer card. The microwave pulse injects SAWs which propagate through the resonator. After one round trip, i.e. being reflected once on the grating mirrors, the SAWs pass the IDT once more and create a microwave signal. This process repeats itself with each consecutive round trip and should result in a periodic train of signal peaks in the time spectrum spaced by the transit time $\tau = L_\mathrm{C}/v_\mathrm{g} \approx 170\,\mathrm{ns}$. Here, we assume a symmetric 1-port SAWR as used in the presented measurements, i.e. the IDT is centered between both mirror. Additionally, we assume a cavity length of $L_\mathrm{C} = 655\,\mu\mathrm{m}$ as determined in sec. 5.2.1 and a group velocity of $v_\mathrm{g} \approx 3800\,\mathrm{m/s}$ [46]. However, the time trace in fig. 5.11a) does not show peaks with a constant periodicity. The spacing between the electromagnetic reflection (solid line) and the following peaks (dashed lines) is 85 ns, 61 ns and 100 ns, respectively. In contrast to the data published by Manenti et al. [70], the decay in amplitude is much faster such that we only record four distinct peaks before no more response is clearly visible.

The non-equidistant spacing of the signals leaves room for interpretation of the physical meaning. We rule out asymmetry arguments of the SAWR as the IDT is exactly centered between the two mirrors. Therefore, SAWs traveling towards any of the two mirrors after injection will pass the IDT after reflection nominally at the same time.

A possible explanation for the non-periodic signal could be interference of at least two different kinds of SAWs with different group velocities and transit times. However, more peaks would be needed to verify this theory. Additionally to the varying time spacing, the peaks in the signal broaden with increasing time. This might suggest a dispersion of the SAW pulse.

All of the mentioned observations - interference of several modes, strong attenuation of SAWs and dephasing of the transit peaks - could indeed be a first hint towards the observation of a SAW response on the complex TFLNO substrate. As the penetration depth into the substrate of a SAW is approximately one wavelength $\lambda = 732\,\mathrm{nm}$, the SAW at least has contributions by the LNO and SiO_x, but maybe also slightly by the silicon substrate. To this end, the measurements cannot be sufficiently explained with the simple assumption of a single SAW mode following the same behavior as on a bulk substrate. We suspect the involvement of multiple SAWs modes due to the different dispersion in each layer of the TFLNO substrate.

Additionally, the line of argument above cannot explain that the peaks signatures do not

[5] We will label the reflected signal measured with the time domain setup as T to be consistent with the cQED time domain measurement notation.

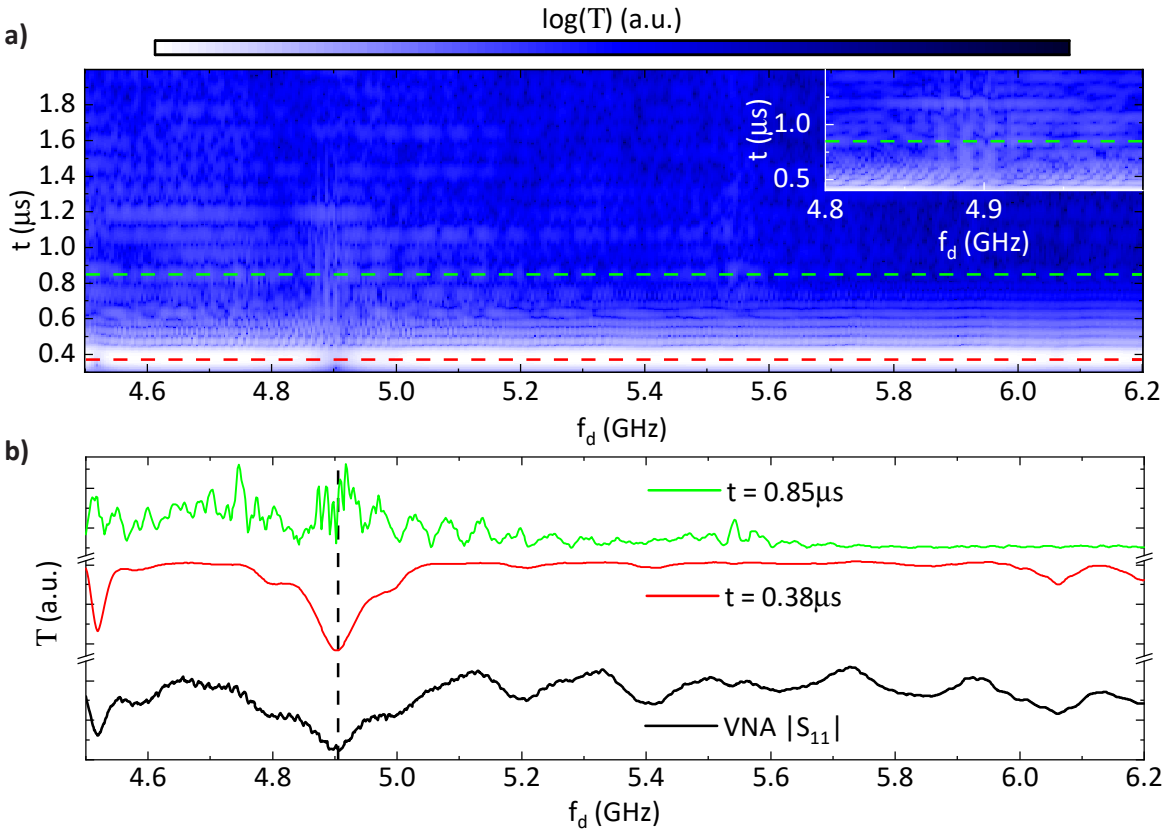

Figure 5.12: Time domain measurements for different microwave frequencies f. **a)** Logarithmic heatmap of the downconverted microwave reflection T at time t after a drive pulse at frequency f. The electromagnetic reflection of the 100 ns drive pulse is measured at $t = 0.38\,\mu s$ with a high amplitude (c.f. fig. 5.11). Afterwards, a ringing is observed for all frequenies, therefore ruling out the SAWR as its origin. Around the resonance frequency of the SAWR, signal is measured until almost 1 µs after the drive pulse. Since the signal is constrained to frequencies around the SAWR stop band, this signal might be related to reflected SAWs. Inset: Zoom into the region of interest. **b)** Reflected signal T as a function of drive frequency f for a fixed point in time (dashed lines in a)). A VNA spectrum (black) is given as reference. The electromagnetic reflection (red) shows a dip at the SAWR resonance frequency (dashed line). At $t = 0.85\,\mu s$, an oscillation in the signal amplitude (green) with decreasing amplitude away from the SAWR frequency is observed. A qualitative discussion of these features is provided in the main text.

coincide with the expected transit time of 170 ns. On average, the spacing is about half of the expected value. More drastically speaking, neither a doubling of the group velocity v_g nor a halving of the cavity length L_C appears reasonable. Therefore, it is possible that the peaks are in fact unrelated to the physics of the SAWR but instead correspond to an electromagnetical ringing of the measurement setup.

For some drive frequencies within the stop band, as exemplary shown in fig. 5.11b), a peak in the reflected signal can be observed at $t = 0.85\,\mu s$. This might hint towards a feature induced

by SAWs as we do not expect a sudden electromagnetic reflection 500 ns after the initial drive pulse. To evaluate these peaks further, analogous measurements were performed for a wide range of different drive frequencies f_d with the same pulse length of 100 ns. The data is shown as a color plot in fig. 5.12a). The transmission T is plotted logarithmically against the drive frequency f_d and time t to increase the visibility of small peaks. The strong electromagnetic pulse at $t = 0.38\,\mu\mathrm{s}$ is followed by several smaller peaks present at all drive frequencies. This supports the interpretation that the peaks are actually some sort of ringing induced by the measurement setup. If the signals were caused by the SAWR, a decay of the signal amplitude should occur when driving the resonator off-resonant, i.e. $> 100\,\mathrm{MHz}$ away from the IDT center frequency, due to a decreased IDT response (eq. 2.50) and mirror reflectivity eq. 2.58). Since this is not the case, a correlation with the SAWR can be ruled out.
The ringing behavior decays for $t > 0.7\,\mu\mathrm{s}$ in the measurement. However, for frequencies close to the SAWR resonance, peaks in the reflected signal can be observed for $t > 0.7\,\mu\mathrm{s}$ (c.f. inset of fig. 5.12a)). A peak in the reflected microwave pulse is visible for constant times throughout a narrow band of around 30 MHz in the range of 4.88 to 4.91 GHz, the frequency band which we have identified in fig. 5.9 as the stopband of the grating.. Moreover, the signal amplitude oscillates with respect to the drive frequency f_d. On the one hand, this could be interpreted as the resonator beating induced by off-resonant drive. However, the oscillation could also hint towards a stop band as discussed in the frequency spectrum in fig. 5.9. The stop band reflectivity, assuming strong reflectivity $N_\mathrm{g}\,|r_\mathrm{s}| \gg 1$, is unity for a frequency range of approx. 30 MHz with $|r_\mathrm{s}| \approx 1\%$ and a center frequency $f_\mathrm{c} = 5\,\mathrm{GHz}$. Outside of the stop band, the reflectivity exhibits a sinc-like oscillations which could explain the oscillation of the signal strength (see fig. 2.14). In fig. 5.12b), we further investigate this behavior as well as the frequency dependence of the electromagnetic peak at $t = 0.38\,\mu\mathrm{s}$. A VNA spectrum is shown for reference (black).

The initial peak at the time of the microwave excitation (red) has an amplitude minimum at the resonance frequency of the investigated SAWR (dashed line in panel b)). This minimum matches the center frequency of the IDT where microwaves can be most efficiently converted to SAWs such that the electromagnetic reflection is minimal at this drive frequency. However, the IDT frequency response should have a characteristic shape resulting from the IDT acoustic conductance as shown in fig. 2.12a). Due to the small amount of finger pairs ($N_\mathrm{p} = 5$), the IDT should create SAWs efficiently in a broad range of frequencies of approximately 0.9 GHz around the center frequency $f = 4.9\,\mathrm{GHz}$ following eq. 2.52. The width of the dips in fig. 5.12b) both from the VNA spectrum as well as the slice at $t = 0.38\,\mu\mathrm{s}$ in the time domain measurement have a FWHM of 80 MHz which is too narrow by one order of magnitude to be explained simply by of the dip via IDT characteristics.

The green dataset corresponds to the amplitude of the peak at $t = 0.85\,\mu\mathrm{s}$ for each time trace (green line in fig. 5.12a)). The peak has a time separation of approximately 470 ns from the microwave pulse and is pronounced for certain drive frequencies. With the quality factor $Q \approx 2 \times 10^4$ extracted in fig. 5.10c), we expect a decay rate of SAWs on the order of 4 µs, the observed feature could therefore very well originate from SAWs. The slice in the spectrum depicted in panel b) shows an oscillatory behavior in the peak amplitude that resembles the grating reflection coefficient in fig. 2.14. This might suggest a SAW response due to the frequency

dependent grating reflection outside the stop band, see fig. 2.14a). The recorded signal does not replicate the grating reflection curve directly as it is a convolution of the IDT response (i.e. the conductance) and the grating reflection. However, the oscillation period (approx. 50 MHz) matches neither the period of the grating reflectivity outside the stop band (approx. 10 MHz from fig. 2.14) nor the period of the IDT acoustic conductance (approx. 0.9 GHz from fig. 2.12a)). Also there is no clear stop band visible around the SAW response at $f_\mathrm{d} = 4.9\,\mathrm{GHz}$.
To this end, the origin of the spectrum signature at $t = 0.85\,\mu\mathrm{s}$ is not clear. The short 100 ns with a bandwidth of 4.4 MHz is broad enough to inject SAWs within multiple resonance dips (see fig. 5.9). Therefore, a variety of SAWs might interfere to produce the observed time traces. This might change the observed spectrum from the expectation of probing the grating reflection frequency dependence as shown in fig. 2.14a). Furthermore, multiple transits of the SAWs (transit time $\tau \approx 170\,\mathrm{ns}$)have occured at the investigated time, which is 470 ns after the pulse ejection. Multiple reflections, especially on the IDT consisting of 11 electrodes with a single electrode reflectivity of $|r_\mathrm{s}| \approx 1\%$ could also play a role for the spectrum as opposed to single transits, where the reflection at the IDT is usually negligible. For the description of the observed data, a more involved model accounting for multiple SAWs and multi-reflections has to be developed in future experiments.

5.2.2.2 Resonator Ring-Down

To access the resonator properties of the SAWR, we prepare the resonator in a steady-state using a long microwave pulse and investigate the SAWR ring-down behavior in this section. Fig. 5.13a) shows a single time trace of the microwave reflection during and after exciting the SAWR with a 5 µs-pulse at $f_\mathrm{d} = 4.8946\,\mathrm{GHz}$. At the onset of the microwave pulse ($t = 0.38\,\mu\mathrm{s}$), a sharp rise in the reflection T is visible, followed by a decaying ringing behavior (zoom in fig. 5.13b), left). At about $t = 2.5\,\mu\mathrm{s}$, the SAWR reaches its steady-state and thus the reflection stays constant. As soon as the microwave is switched off, the (electromagnetic) reflection decreases sharply. Following the abrupt change, an additional decaying ringing behavior can be observed (zoom in panel b), right).
Subsequently, this measurement is done for a range of drive frequencies f_d within the suspected stop band in fig. 5.9. We normalize the reflection T of each time trace to its steady-state amplitude during the drive, i.e. in the interval $t = 4.5$ to $5.0\,\mu\mathrm{s}$ (c.f. fig. 5.13a)).
Fig. 5.13c) shows the normalized reflection amplitude of previously investigated areas (time ranges in panel b)) in a color plot as a function of the drive frequency f_d and the time t. Both regions are depicted with the same color map for better comparison, however the amplitude ranges differ and are given in the respective panels. Additionally, the VNA spectrum of the devices response for the same frequency range is given for reference. The dashed line indicates the drive frequency for panels a) and b).
The microwave pulse is applied at $t = 0.38\,\mu\mathrm{s}$ and ends at $t = 5.38\,\mu\mathrm{s}$ for these measurements. For both the ring-up and -down traces, a peak in the reflection can be observed around $\Delta t = 170\,\mathrm{ns}$ (dashhed horizontal lines in the insets of fig. 5.13c)) after the microwave drive start and end, respectively, when driving the device with $f_\mathrm{d} = 4.891\,\mathrm{GHz}$ and $f_\mathrm{d} = 4.8946\,\mathrm{GHz}$. The VNA spectrum shows dips at these frequencies which we identified with SAWR Rayleigh modes in fig.

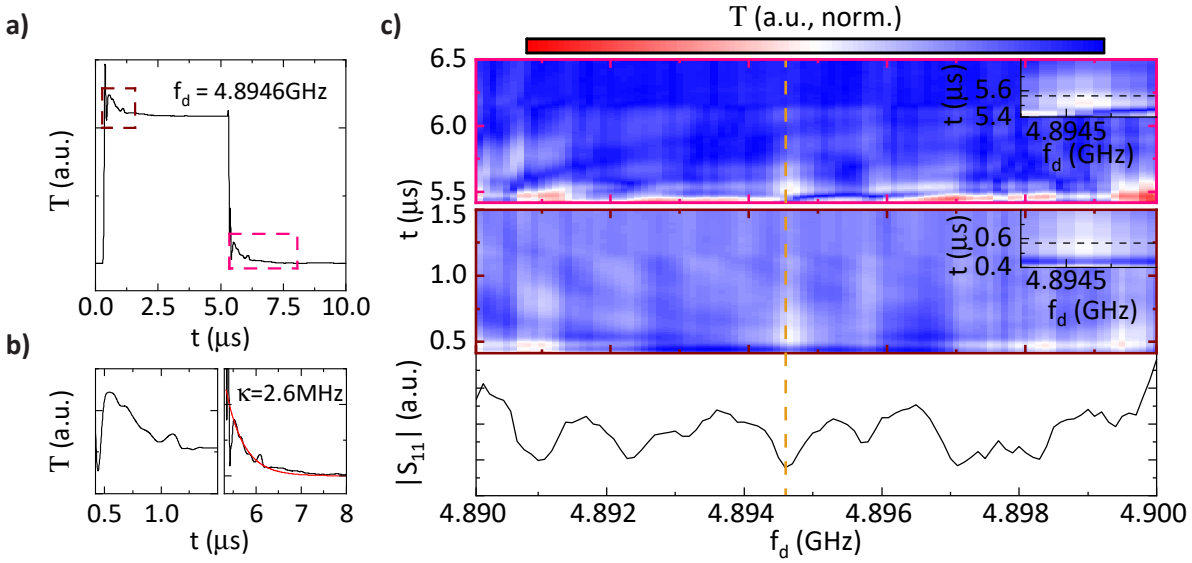

Figure 5.13: Time-domain analysis of the investigated SAWR with long drive pulses to reveal resonator characteristics. **a)** Time-resolved, downconverted microwave reflection during and after a 5µs drive pulse at a fixed frequency $f_\mathrm{d} = 4.8946\,\mathrm{GHz}$. The drive pulse starts at $t = 0.38\,\mu\mathrm{s}$. The resonator is populated during the pulse and reaches a steady state for $t > 3\,\mu\mathrm{s}$. After the pulse, a ring-down behavior can be observed. **b)** Zoom into the dashed boxes of a). The initial overshoot of the ring-up is most likely caused by the measurement electronics and cut away for the zoom. **c)** Frequency dependence of the ringing behavior. A VNA spectrum is given for reference. The heatmaps show the reflection amplitude T normalized to the steady-state amplitude of the populated resonator. For the ring-up (lower heatmap), amplitudes lower than the steady state are observerd and likely caused by electronic ringing. Insets: For both ring-up and -down, a peak is observed around 170ns after the microwave pulse is switched on/off, respectively (dashed line).

5.10a). This could indicate a response of the SAWR as this behavior is not observed for different driving frequencies.

The intuitive explanation for the ring-up feature is similar to the discussion in sec. 5.2.2.1: As the microwave pulse is applied, SAWs are injected in the resonator. Before a steady-state is reached and the standing waves are built up in the resonator, individual transits of the injected wave should be visible. The first transit of the injected SAWs therefore could change the reflection T after the transit time τ, when the resonator is not filled with standing wave-modes yet. The time difference between microwave pulse and peak Δt matches the transit time calculated in sec. 5.2.2.1 of $\tau = 170\,\mathrm{ns}$. This strengthens the conjecture of a visible SAWR mode.

The ring-down spectrum shows qualitatively the same behavior with peaks at the same frequency. Additionally, there is a peak around $f_\mathrm{d} = 4.900\,\mathrm{GHz}$ which does not appear in the ring-up spectrum. Again, the time difference of the peaks at the Rayleigh mode frequencies with respect to the end of the drive pulse ($t = 5.38\,\mu\mathrm{s}$) is around $\Delta t = 170\,\mathrm{ns}$, matching the transit time τ. For the ring-down, we would expect a superposition of the SAWR exponential decay and the measurement setup ringing. In the shown ring-down time trace (panel b) of fig. 5.13, right), a

distinction between the ringing and the decay is not possible. An exponential fit to the ring-down determines a decay rate of $\kappa/2\pi = 2.6\,\mathrm{MHz}$, corresponding to a quality factor of $Q = 1882$. This decay is therefore an order of magnitude faster than extracted from the fit in fig. 5.10b), which is unexpected. Most likely, the deviation from the expected SAWR ring-down is caused by the electric ringing.

5.2.3 Discussion

In this chapter we have analyzed a surface acoustic wave resonator on a LNO/SiO_x/Si multilayer substrate using frequency analysis as well as time-resolved reflection measurements. The frequency domain analysis suggests a complex Fabry-Perot behavior with multiple modes and resonances. Assuming a double-peak characteristic with free-spectral ranges of $\nu_\mathrm{R} = 2.9\,\mathrm{MHz}$ and $\nu_\mathrm{sh} = 3.0\,\mathrm{MHz}$ for Rayleigh and shear-horizontal modes as well as a speed of sound $v_\mathrm{p} = 3800\,\mathrm{m/s}$ [46], the effective cavity length $L_\mathrm{C} = 655\,\mu\mathrm{m}$ and single electrode reflectivity $|r_\mathrm{s}| = 0.14\%$ were determined. These results are not consistent with literature, e.g. Refs. [28, 29, 30] where $|r_\mathrm{s}|$ on bulk LNO is typically on the order of a few percent. On the other hand, if we assume a single electrode reflectivity as reported in literature, we would expect vastly different FSRs or phase velocities v_p. Further investigation is therefore necessary to understand the resonator behavior on this complex substrate. The internal quality factors of different modes were computed to $Q_\mathrm{i} = (8 - 16) \times 10^3$ with eq. 2.64. No power dependence was observable as the lowest applicable power with visible signal $P_\mathrm{appl} = -70\,\mathrm{dBm}$ equals a mean phonon occupation of $\langle n_\mathrm{ph} \rangle = 24$ according to eq. 2.44.

For time resolved characteristics, 100 ns-pulses were applied to the resonator in order to create a traveling SAW package and resolve its repeated propagation across the resonator and the IDT. As the corresponding bandwidth of the pulse is 4.4 MHz, nearby resonances could have been excited during the measurements, leading to contribution of multiple SAWs to the measured signal. For future experiments, the FSR of the cavity has to be increased to avoid this multi-excitation. In comparison to the expected transit time of $\tau = 170\,\mathrm{ns}$, the pulse is short, such that distinct transits should be visible. Similar experiments were conducted in Ref. [70] with 300 ns-pulses for $\tau = 330\,\mathrm{ns}$. Peaks could be observed in the time spectrum, however no discrete periodicity was found. The oscillating signal is most likely a consequence of the measurement electronics, further investigation should be able to verify this suggestion.
In experiments with long drive pulses, leading to a steady-state of the SAWR, a clear difference in the reflection amplitude was visible when driving the SAWR on- or off-resonance, respectively. For the resonant case, a peak appears in the spectrum around 170 ns after the start and end of the microwave drive pulse, matching the expected transit time τ. This feature is not observed for off-resonant drives. Therefore, this could indicate a distinct phononic respone of the resonator. However, the decay of the investigated SAWR mode after reaching a steady-state yields a quality factor of $Q = 1882$, an order of magnitude lower than expected from frequency domain measurements.

Overall, the measured characteristics do not show agreement with the assumptions of a simple Fabry-Perot cavity behavior on a bulk piezoelectric substrate. A possible explanation could be the complicated TFLNO substrate with three materials and therefore three different longitudinal and

transversal speeds of sound. As the SAW can have contributions from all substrates, this can lead to a complicated dispersion, comparable to an optical cavity with three different dielectrics along the propagation axis. In the long run, the TFLNO substrate will be replaced with a substrate consisting only of LNO and silicon. SAW devices have been fabricated with promising results on thin-film substrates with only one thin-film layer [104, 105, 106, 107] as opposed to our more complicated TFLNO stack with two thin-film layers. Therefore, less complex behavior can be expected for a single thin-film layer of LNO on silicon.

Chapter 6

Outlook & Summary

6.1 Future Prospects: On-Chip cQAD

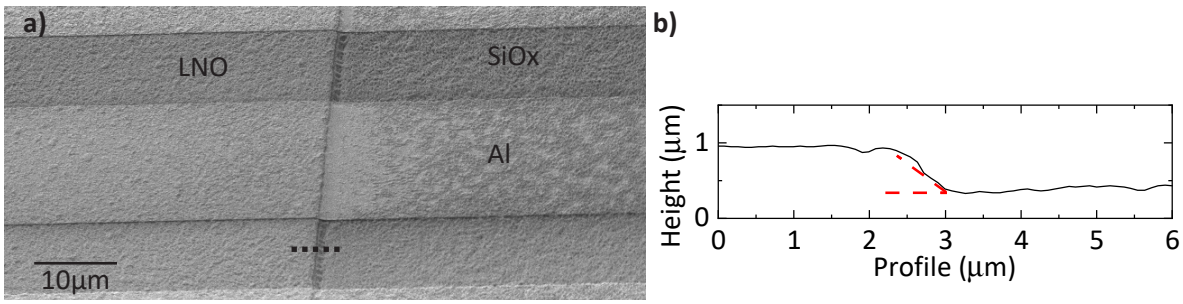

Figure 6.1: **a)** Scanning electron microscope image of a CPW bridging the height difference between areas with (left) and without (right) thin-film LNO. The CPW was only tested for ohmic contact, no microwave measurements were conducted. **b)** Profile of the "ramp" from the SiO_x surface to the thin-film LNO acquired by atomic force microscopy along the dashed line in a). The height difference of 500 nm is almost linearly surpassed on a length of 750 nm.

After the investigation of superconducting qubits on silicon and SAW devices on thin-film lithium niobate, we want to give a brief outlook on the next steps towards on-chip cQAD. Since piezoelectricity can limit the qubit coherence drastically, our approach is to remove the thin-film LNO on any part of the sample where no SAW devices are present. This however brings up the challenge of transitioning from the silicon substrate to the 500 nm high plateau of LNO with a continuous connection that supports a CPW transmission line. In this chapter, we briefly present the first attempts at realizing a "ramp" to bridge the gap between the two sample areas.

We fabricate the ramp formation with a RIE etch protocol using large gas flows of SF_6 and Ar following observations in Ref. [108]. The oversupply of SF_6 during the etch process leads to the formation of lithium fluoride (LiF) which is subsequently redeposited. The lithium fluoride acts as an inhibitor for the chemical etch process and is only removed by argon-ion bombardment. This effect is however weakened close to the sidewall, i.e. the edges of the thin-film LNO. Therefore, a ramp is formed by the LiF. To protect regions from the etch process, we use a thick (200 nm) Al etch mask[1] that is removed after the etching process with a chemical wet-etchant selective to Al. Fig. 6.1a) shows a scanning electron microscope image of a CPW on a ramp leading from an area

[1] The unetched LNO surface of the sample in 6.1a) is very rough as the etch mask was only 100 nm Al. Subsequent chips were fabricated with a thicker mask and did not show an increased roughness any more.

without thin-film LNO to an area where no LNO was removed. A smooth transition between the plateaus is visible. The CPW was successfully probed to show galvanic ohmic contact, however no microwave measurements were conducted. In panel b), an atomic force microscopy height profile of the ramp along the dashed line in panel a) is shown. The height difference of 500 nm is bridge almost linearly on a length scale of 750 nm. This equals a constant slope of 34°.

In future experiments, the etch process will be further optimized to deal with the rough surface created on the unprotected SiO_x/Si surface. Also the influence of the redeposited LiF on microwave transmission and coherence times has to be investigated.

6.2 Summary

The goal of this thesis was to pave the way for quantum acoustodynamic experiments at the WMI. To this end, fabrication and measurements of both circuit quantum electrodynamic and surface acoustic wave devices have been performed.

We established a scalable Xmon qubit fabrication process following Ref. [85] and conducted full qubit spectroscopy in the frequency and time domain. The results leave room for improvement, however a proof-of-concept of this fabrication method was provided and insight was gained for future improvements in the sample design and fabrication. By utilizing the findings of this thesis as well as new equipment to optimize the process, we are confident to reach the intended coherence times of few µs in the near future. In particular, the introduction of a sophisticated substrate cleaning likely provides a significant increase of the quality of our Xmon qubits.

With the BEAMER software package, we have introduced proximity effect correction into the electron beam lithography workflow for the fabrication of SAW devices in the gigahertz-regime, the second mandatory component for quantum acoustodynamic experiments.

We investigated a 1-port SAW resonator on a lithium niobate thin-film substrate potentially promising for on-chip QAD. Both frequency and time domain measurements were conducted. We performed measurements with short excitation pulses to gain information of the IDT behavior and track single wave packages transiting the IDT. Additionally, we investigated the resonator ring-up and -down behavior for long drive pulses that allow standing wave creation. The measurements revealed complex dynamics that differs significantly from the well-understood behavior of SAW resonators on bulk materials. SAWRs on multilayer substrates will therefore be subject to further research, where we plan to compare experimental data with finite element simulations. Additionally, reference samples of identical resonator structures on bulk lithium niobate will be fabricated in order to provide a baseline of experimental data that should help to distinguish between common SAWR signatures and features specific to multi-layer systems. Ultimately, a LNO/Si substrate will be studied and eventually replace the LNO/SiO_x/Si substrate once films of sufficiently high quality become more widely available.

Lastly, we demonstrated a promising proof-of-concept for combining both cQED and SAW elements on a single chip. To this end, we have constructed a RIE process that can selectively remove LNO from parts of the chip and at the same time form a “ramp” to smoothly bridge the height difference between cQED and SAW areas on the chip. This will enable us in the long-term to have full control over the positioning of cQED and SAW elements on our samples, allowing for much batter scalability compared to previous flip-chip assemblies.

Appendix A

Appendix: Theory

A.1 Rotating Frame and Optical Bloch Equations

In this section, we will derive the driven qubit Hamiltonian in the rotating frame $\widetilde{H}_{\mathrm{d,q}}$ in eq. 2.32 as well as the optical Bloch equation in eq. 2.37.

A.1.1 Driven Qubit in the Rotating Frame

Starting with the driven qubit Hamiltonian (eq. 2.31)

$$\hat{H}_{\mathrm{d,q}}/\hbar = \frac{\omega_{\mathrm{q}}}{2}\hat{\sigma}_{\mathrm{z}} + \frac{\epsilon_{\mathrm{d}}}{2}\left(e^{-i\omega_{\mathrm{d}}t} + e^{i\omega_{\mathrm{d}}t}\right)\left(\hat{\sigma}_{-} + \hat{\sigma}_{+}\right), \tag{A.1}$$

we find the differential equations for the time evolution of an arbitrary pure qubit state $|\psi(t)\rangle = a_{\mathrm{e}}(t)\,|e\rangle + a_{\mathrm{g}}(t)\,|g\rangle$ using the Schrödinger equation $i\hbar\frac{\mathrm{d}}{\mathrm{d}t}\,|\psi(t)\rangle = \hat{H}\,|\psi(t)\rangle$. The set of equations reads

$$i\frac{\mathrm{d}}{\mathrm{d}t}a_{\mathrm{e}}(t) = \frac{\omega_{\mathrm{q}}}{2}a_{\mathrm{e}}(t) + \frac{\epsilon_{\mathrm{d}}}{2}\left(e^{-i\omega_{\mathrm{d}}t} + e^{i\omega_{\mathrm{d}}t}\right)a_{\mathrm{g}}(t), \tag{A.2}$$

$$i\frac{\mathrm{d}}{\mathrm{d}t}a_{\mathrm{g}}(t) = \frac{\epsilon_{\mathrm{d}}}{2}\left(e^{-i\omega_{\mathrm{d}}t} + e^{i\omega_{\mathrm{d}}t}\right)a_{\mathrm{e}}(t) - \frac{\omega_{\mathrm{q}}}{2}a_{\mathrm{g}}(t). \tag{A.3}$$

To remove the explicit time dependence of eqs. A.2 and A.3, we switch to a *rotating frame* with an angular speed ω_{d} by making the replacements

$$b_{\mathrm{e}}(t) = e^{i\omega_{\mathrm{d}}t/2}a_{\mathrm{e}}(t), \tag{A.4}$$

$$b_{\mathrm{g}}(t) = e^{-i\omega_{\mathrm{d}}t/2}a_{\mathrm{g}}(t). \tag{A.5}$$

In the rotating frame, eqs. A.2 and A.3 simplify to

$$i\frac{\mathrm{d}}{\mathrm{d}t}b_{\mathrm{e}}(t) = \frac{\omega_{\mathrm{q}} - \omega_{\mathrm{d}}}{2}b_{\mathrm{e}}(t) + \frac{\epsilon_{\mathrm{d}}}{2}\left(1 + e^{2i\omega_{\mathrm{d}}t}\right)b_{\mathrm{g}}(t), \tag{A.6}$$

$$i\frac{\mathrm{d}}{\mathrm{d}t}b_{\mathrm{g}}(t) = \frac{\epsilon_{\mathrm{d}}}{2}\left(1 + e^{-2i\omega_{\mathrm{d}}t}\right)b_{\mathrm{e}}(t) - \frac{\omega_{\mathrm{q}} - \omega_{\mathrm{d}}}{2}b_{\mathrm{g}}(t). \tag{A.7}$$

The final simplification can be done by applying *rotating wave approximation* (RWA) [50, 59]. For this, we neglect terms that rotate very fast (here with $2\omega_{\mathrm{d}}$) and therefore average to zero quickly. Neglecting all terms with contributions $\propto 2\omega_{\mathrm{d}}$ in eqs. A.6 and A.7, we find

a explicitly time independent set of equations corresponding to the Hamiltonian in eq. 2.32

$$\widetilde{H}_{\mathrm{d,q}}/\hbar = \frac{1}{2}\left(-\Delta\omega\hat{\sigma}_{\mathrm{z}} + \epsilon_{\mathrm{d}}\hat{\sigma}_{\mathrm{x}}\right), \tag{A.8}$$

where $\Delta\omega = \omega_{\mathrm{d}} - \omega_{\mathrm{q}}$

A.1.2 Optical Bloch Equation

A visual representation of the Hamiltonian in eq. A.8 by rewriting the Hamiltonian to

$$\widetilde{H}_{\mathrm{d,q}} = \frac{\hbar}{2}\vec{\Omega}\cdot\vec{\sigma}, \tag{A.9}$$

where $\vec{\Omega} = (\epsilon_{\mathrm{d}}, 0, -\Delta\omega)$ is the rotation vector on the Bloch sphere and $\vec{\sigma} = (\sigma_{\mathrm{x}},\sigma_{\mathrm{y}},\sigma_{\mathrm{z}})$ is the Pauli matrix vector.
In sec. 2.4.2, we defined the state vector $\vec{r}$ of a qubit on the Bloch sphere in terms of its length r and two angles ϕ and θ. Another representation of the state vector is by using the expectation values along the x, y and z axes which can be calculated with the Pauli matrices as

$$\vec{r} = \begin{pmatrix} \langle\sigma_{\mathrm{x}}\rangle \\ \langle\sigma_{\mathrm{y}}\rangle \\ \langle\sigma_{\mathrm{z}}\rangle \end{pmatrix}. \tag{A.10}$$

Using the Ehrenfest theorem for operators [109]

$$\frac{\mathrm{d}}{\mathrm{d}t}\langle\hat{O}\rangle = \frac{i}{\hbar}\left\langle\left[\hat{H},\hat{O}\right]\right\rangle + \left\langle\frac{\partial\hat{O}}{\partial t}\right\rangle, \tag{A.11}$$

as well as the commutator relation for the Pauli matrices

$$[\sigma_i,\sigma_j] = 2i\epsilon_{ijk}\sigma_k, \tag{A.12}$$

where ϵ_{ijk} is the Levi-Civita symbol, we find the following relation for the time evolution of the Bloch state vector $\vec{r}$:

$$\begin{aligned}\frac{\mathrm{d}}{\mathrm{d}t}r_i = \frac{\mathrm{d}}{\mathrm{d}t}\langle\sigma_i\rangle = \frac{i}{\hbar}\left\langle\left[\widetilde{H}_{\mathrm{d,q}},\sigma_i\right]\right\rangle = \frac{i}{2}\sum_j \Omega_j\langle[\sigma_j,\sigma_i]\rangle = \frac{i}{2}\sum_{jk}\Omega_j\left(-2i\epsilon_{ijk}\langle\sigma_k\rangle\right) \\ = \left[\vec{\Omega}\times\langle\vec{\sigma}\rangle\right]_i.\end{aligned}$$

For the last step, we used the definition $\left[\vec{a}\times\vec{b}\right]_k = \epsilon_{ijk}a_ib_j$ and the permutation relation $\epsilon_{ijk} = \epsilon_{jki}$. In vector notation, this leads to eq. 2.37

$$\frac{\mathrm{d}}{\mathrm{d}t}\vec{r} = \vec{\Omega}\times\vec{r}. \tag{A.13}$$

A.2 Qubit Frequency Drift

In this section, we present the calculation for the numerical Rabi drive solution in fig. 5.6. For this calculation, we implement a finite overlap t_o of the drive and readout pulse as discussed in the main text (c.f. sec. 5.1.4.2). The starting point is the modified Hamiltonian for a driven qubit in the rotating frame, where the qubit frequency ω_q is time dependent (eq. 5.8):

$$\widetilde{H}(t)/\hbar = \frac{1}{2}\begin{pmatrix} -(\omega_\mathrm{d} - \omega_\mathrm{q}(t)) & \epsilon_\mathrm{d} \\ \epsilon_\mathrm{d} & (\omega_\mathrm{d} - \omega_\mathrm{q}(t)) \end{pmatrix}. \tag{A.14}$$

As above, ω_d and ϵ_d are the drive frequency and amplitude. With the Schrödinger equation, the set of differential equations after a RWA is similar to eqs. A.6 and A.7

$$\frac{\mathrm{d}}{\mathrm{d}t}b_\mathrm{e}(t) = \frac{\omega_\mathrm{q}(t) - \omega_\mathrm{d}}{2i}b_\mathrm{e}(t) + \frac{\epsilon_\mathrm{d}}{2i}b_\mathrm{g}(t), \tag{A.15}$$

$$\frac{\mathrm{d}}{\mathrm{d}t}b_\mathrm{g}(t) = \frac{\epsilon_\mathrm{d}}{2i}b_\mathrm{e}(t) - \frac{\omega_\mathrm{q}(t) - \omega_\mathrm{d}}{2i}b_\mathrm{g}(t). \tag{A.16}$$

Due to the coupling g between the qubit and the microwave resonator, the qubit frequency undergoes a dispersive shift of the form (eq. 2.23)

$$\omega_\mathrm{q}(t) = \omega_\mathrm{q}^{bare} + \left(2\chi\langle n_\mathrm{ph}\rangle(t) + \frac{1}{2}\right). \tag{A.17}$$

We denote the bare qubit frequency, i.e. the eigenfrequency of the qubit without any coupling to the environment or circuitry, as ω_q^{bare}. Crucially, the mean photon number in the readout resonator is time dependent in the case of overlapping pulses as the resonator is started to be filled with photons during part of the drive pulse. For the used toy model, we assume an exponential time dependence of the photon number

$$\langle n_\mathrm{ph}\rangle(t) = \begin{cases} A\left(e^{(t-\tau+t_\mathrm{o})/t_\mathrm{r}} - 1\right) & \text{for } t > \tau - t_\mathrm{o}, \\ 0 & \text{else}, \end{cases} \tag{A.18}$$

where A is an amplitude factor, t the time starting at the beginning of the drive pulse, τ is the drive pulse length, t_o is the overlap time and t_r the characteristic ring-up time of the resonator.

Numerically solving the set of differential equations A.15 and A.16 with initial values $b_\mathrm{e}(0) = 0$ and $b_\mathrm{g}(0) = 1$ leads to the pattern shown in fig. 5.6. The used parameters approximately representing the ring-up behavior (time and occupation) of the resonator as well as the measured Chevron pattern are $A = 160$, $t_\mathrm{o} = 200\,\mathrm{ns}$, $t_\mathrm{r} = 1\,\mu\mathrm{s}$ and $\epsilon_\mathrm{d} = 1.15 \times 10^8$. The qubit and resonator frequencies characteristics can be found in table 5.1.

Appendix B

Appendix: Fabrication

B.1 cQED Fabrication

The following is a detailed fabrication sequence for a 3-step bandaging process. The essential steps are described and illustrated in sec. 3.2.2.

Preparation and non-Josepheson Elements

1. Clean new Si chip by ultrasonic bath in technical acetone (room temp.), p.a. acetone (room temp.), p.a. acetone (70°C), IPA (70°C) and IPA (room temp.) for 2 minutes each, dry with N_2, ash 3 minutes with O_2, (optionally) briefly bake at 170-200°C.
2. Spin-coat chip with 60µl positive EBL resist PMMA/MA(33%) (AR-P 617.08) for 60s at 4000RPM. Bake at 170°C for 2 minutes.
3. Define alignment markers for subsequent fabrication steps by EBL ($6.5\,C/m^2$). Square with $10 \times 10\,\mu m^2$ (mp_sqr10) are typically used.
4. Develop in AR600-56 for 2 minutes (constant "8"-motion), rinse 2x in IPA, dry with N_2.
5. Evaporate Ti(6nm)/Au(24nm) onto sample.
6. Lift-off resist layer with excess metal in 70°C aceton. Soak sample for 12-15 minutes. Remove dissolved material with disposable pipette and transfer sample to new beaker. Repeat last step after 5 minutes until resist layer is gone. Optionally, use ultrasonic bath if material remains on the substrate. Rinse in p.a. acetone and IPA, dry with N_2.
7. Spin-coat chip with 60µl positive EBL resist PMMA/MA(33%) (AR-P 617.08) with 2-step programm[1] (5s at 500RPM, 60s at 8000RPM). Bake at 170°C for 2 minutes.
8. Define non-Josephson elements with EBL ($2.3\,C/m^2$). Use database with < 10nA for increased process speed, beam spotsize is not crucial.
9. Develop in AR600-56 for 2 minutes on the rotation plate (500RPM, hold sample with tweezers), rinse 2x in IPA, dry with N_2.
10. Evaporate Al(100nm).
11. Lift-off as in step 6. For ultrasonication: lowest power, only few seconds!

[1] This step is due to an error in the recipe, ideally, one would use 70s at 8000RPM. The exposure dose then might differ from the given values.

SQUID

1. Prebake sample 2 minutes at 170-200°C.
2. Spin-coat chip with 60µl positive EBL resist PMMA/MA(33%) (AR-P 617.08) for 120s at 2000RPM. Bake at 160°C for 10 minutes[2].
3. Spin-coat chip with 60µl positive EBL resist PMMA950K (AR-P 679.02) for 120s at 2000RPM. Bake at 160°C for 10 minutes[3].
4. Define SQUID. Exposure is done with a PEC corrected pattern[4] (base dose 6.75 C/m^2). Use lowest current database for minimum spot size and best precision.
5. Develop 30s in AR600-56 without moving, then immediately transfer to 4°C-cold IPA for 10 minutes. Do not rinse, immediately dry with N_2.
6. Evaporate 64nm Al 55° normal to the substrate surface. Oxidize for 100 minutes with oxide pressure 7.9×10^{-3} mbar (old evap system: VAT 15%, O_2 flowrate 8sccm). Evaporate 70nm Al 0° normal to the substrate surface. The 55°-rotation angle should be chosen in such a way that the Josephson junction is formed in the same way as depicted in fig. 3.4a).
7. Lift-off resist layer with excess metal in 70°C aceton. Soak sample for 12-15 minutes. Remove dissolved material with disposable pipette and transfer sample to new beaker. Repeat last step after 5 minutes until resist layer is gone. Do not use ultrasonic bath. Rinse in p.a. acetone and IPA, dry with N_2.

Bandage

1. Depending on time passed between SQUID lift-off and bandage fabrication, carefully clean sample (no ultrasonication!).
2. Prebake sample 2 minutes at 170°C.
3. Spin-coat chip with 60µl positive EBL resist PMMA600K (AR-P 699.04) for 60s at 4000RPM. Bake at 170°C for 5 minutes.
4. Spin-coat chip with 60µl positive EBL resist PMMA950K (AR-P 679.02) for 60s at 4000RPM. Bake at 170°C for 5 minutes.
5. Define bandages, exposure dose 1.2×5.8 C/m^2 for clearing, 1.0×5.8 C/m^2 for undercut.
6. Develop 120s in AR600-56 under constant "8"-shape movement.
7. Ar-ion mill bandage region with Kaufman & Robinson ion source type EH200HC, currently done in SUPERBOWL system, for 240s. Set parameters in table B.1.
8. Sputter 150nm Al with power 150W at set height 30mm.
9. Lift-off resist layer with excess metal in 70°C aceton. Soak sample for 12-15 minutes. Remove dissolved material with disposable pipette and transfer sample to new beaker. Repeat last step after 5 minutes until resist layer is gone. Do not use ultrasonic bath. Rinse in p.a. acetone and IPA, dry with N_2.
10. Ash 3 minutes with O_2.

[2] Recent developments in Quantum Computing group suggest a bake duration of 3 minutes.
[3] As above.
[4] The PEC corrected pattern for the SQUID was provided by GenISys in the scope of a BEAMER showcase.

Table B.1: Kaufman & Robinson ion source type EH200HC settings

Parameter	MFC1	MFC4	KC	EV	EA	DV	DA
Set	3sccm	10sccm	1.5A	120V	0.5A	100V	0.5A
Is	2.9sccm	10sccm	1.5A	54V	0.5A	100V	0.5A

B.2 SAW Devices

The following is a detailed fabrication sequence for the SAW devices on LNO(500nm)/SiOx(2µm)/Si(350µm).

1. Clean new Si chip by ultrasonic bath in technical acetone (room temp.), p.a. acetone (room temp.), p.a. acetone (70°C), IPA (70°C) and IPA (room temp.) for 2 minutes each, dry with N_2, ash 3 minutes with O_2, (optionally) briefly bake at 170-200°C.
2. Spin-coat chip with 60µl positive EBL resist PMMA/MA(33%) (AR-P 617.08) for 60s at 8000RPM. Bake at 170°C for 2 minutes.
3. Define SAW device with PEC corrected pattern, base dose 2.65C/m^2. Consider exposure dose from surrounding ground planes (dose multiplier 1.0) for the proximity effect!
4. Develop 120s in AR600-56 on the rotation plate (500RPM, hold sample with tweezers), rinse 2x in IPA, dry with N_2.
5. Evaporate 100nm Al.
6. Lift-off resist layer with excess metal in 70°C aceton. Soak sample for 12-15 minutes. Remove dissolved material with disposable pipette and transfer sample to new beaker. Repeat last step after 10 minutes until resist layer is gone. Optionally, carefully use ultrasonic bath if material remains on the substrate (lowest power, only for a few seconds, high risk of damaging structures). Rinse in p.a. acetone and IPA, dry with N_2.

Bibliography

[1] H. P. Specht *et al.*, "A single-atom quantum memory", *Nature*, vol. 473, no. 7346, pp. 190–193, May 2011. DOI: 10.1038/nature09997.

[2] M. Saffman, "Quantum computing with neutral atoms", *National Science Review*, vol. 6, no. 1, pp. 24–25, Jan. 1, 2019. DOI: 10.1093/nsr/nwy088.

[3] M. Greiner, O. Mandel, T. Esslinger, T. W. Hänsch, and I. Bloch, "Quantum phase transition from a superfluid to a Mott insulator in a gas of ultracold atoms", *Nature*, vol. 415, no. 6867, pp. 39–44, Jan. 2002. DOI: 10.1038/415039a.

[4] J. Simon, W. S. Bakr, R. Ma, M. E. Tai, P. M. Preiss, and M. Greiner, "Quantum simulation of antiferromagnetic spin chains in an optical lattice", *Nature*, vol. 472, no. 7343, pp. 307–312, Apr. 2011. DOI: 10.1038/nature09994.

[5] A. Wallraff *et al.*, "Strong coupling of a single photon to a superconducting qubit using circuit quantum electrodynamics", *Nature*, vol. 431, no. 7005, pp. 162–167, Sep. 2004. DOI: 10.1038/nature02851.

[6] T. Niemczyk *et al.*, "Circuit quantum electrodynamics in the ultrastrong-coupling regime", *Nature Physics*, vol. 6, no. 10, pp. 772–776, Oct. 2010. DOI: 10.1038/nphys1730.

[7] J. Chan *et al.*, "Laser cooling of a nanomechanical oscillator into its quantum ground state", *Nature*, vol. 478, no. 7367, pp. 89–92, Oct. 2011. DOI: 10.1038/nature10461.

[8] E. Verhagen, S. Deléglise, S. Weis, A. Schliesser, and T. J. Kippenberg, "Quantum-coherent coupling of a mechanical oscillator to an optical cavity mode", *Nature*, vol. 482, no. 7383, pp. 63–67, Feb. 2012. DOI: 10.1038/nature10787.

[9] T. Luschmann *et al.* "Mechanical frequency control in inductively coupled electromechanical systems". (Apr. 21, 2021), [Online]. Available: http://arxiv.org/abs/2104.10577.

[10] LIGO Scientific Collaboration and Virgo Collaboration *et al.*, "Observation of Gravitational Waves from a Binary Black Hole Merger", *Physical Review Letters*, vol. 116, no. 6, p. 061 102, Feb. 11, 2016. DOI: 10.1103/PhysRevLett.116.061102.

[11] M. Zhong *et al.*, "Optically addressable nuclear spins in a solid with a six-hour coherence time", *Nature*, vol. 517, no. 7533, pp. 177–180, Jan. 2015. DOI: 10.1038/nature14025.

[12] F. Arute *et al.*, "Quantum supremacy using a programmable superconducting processor", *Nature*, vol. 574, no. 7779, pp. 505–510, Oct. 2019. DOI: 10.1038/s41586-019-1666-5.

[13] M. Gong *et al.*, "Quantum walks on a programmable two-dimensional 62-qubit superconducting processor", *Science*, vol. 372, no. 6545, pp. 948–952, May 28, 2021. DOI: 10.1126/science.abg7812.

[14] E. Saglamyurek *et al.*, "Quantum storage of entangled telecom-wavelength photons in an erbium-doped optical fibre", *Nature Photonics*, vol. 9, no. 2, pp. 83–87, Feb. 2015. DOI: 10.1038/nphoton.2014.311.

[15] L. Weiss, A. Gritsch, B. Merkel, and A. Reiserer, "Erbium dopants in nanophotonic silicon waveguides", *Optica*, vol. 8, no. 1, pp. 40–41, Jan. 20, 2021. DOI: 10.1364/OPTICA.413330.

[16] L. Rayleigh, "On Waves Propagated along the Plane Surface of an Elastic Solid", *Proceedings of the London Mathematical Society*, vol. s1-17, no. 1, pp. 4–11, 1885. DOI: 10.1112/plms/s1-17.1.4.

[17] G. Macchiarella and G. Stracca, "SAW Devices for Telecommunications: Examples and Applications", in *1982 Ultrasonics Symposium*, Oct. 1982, pp. 247–251. DOI: 10.1109/ULTSYM.1982.197823.

[18] D. P. Morgan, *Surface Acoustic Wave Filters: With Applications to Electronic Communications and Signal Processing*, 2nd ed. Amsterdam ; London: Academic Press, 2007, 429 pp.

[19] R. Manenti, M. J. Peterer, A. Nersisyan, E. B. Magnusson, A. Patterson, and P. J. Leek, "Surface acoustic wave resonators in the quantum regime", *Physical Review B*, vol. 93, no. 4, p. 041 411, Jan. 15, 2016. DOI: 10.1103/PhysRevB.93.041411.

[20] U. Delić *et al.*, "Cooling of a levitated nanoparticle to the motional quantum ground state", *Science*, vol. 367, no. 6480, pp. 892–895, Feb. 21, 2020. DOI: 10.1126/science.aba3993.

[21] S. Kotler *et al.*, "Direct observation of deterministic macroscopic entanglement", *Science*, vol. 372, no. 6542, pp. 622–625, May 7, 2021. DOI: 10.1126/science.abf2998.

[22] A. Blais, R.-S. Huang, A. Wallraff, S. M. Girvin, and R. J. Schoelkopf, "Cavity quantum electrodynamics for superconducting electrical circuits: An architecture for quantum computation", *Physical Review A*, vol. 69, no. 6, p. 062 320, Jun. 29, 2004. DOI: 10.1103/PhysRevA.69.062320.

[23] A. Blais, A. L. Grimsmo, S. M. Girvin, and A. Wallraff, "Circuit quantum electrodynamics", *Reviews of Modern Physics*, vol. 93, no. 2, p. 025 005, May 19, 2021. DOI: 10.1103/RevModPhys.93.025005.

[24] D. I. Schuster, "Circuit Quantum Electrodynamics", PhD Thesis, Yale University, 2007.

[25] M. V. Gustafsson, T. Aref, A. F. Kockum, M. K. Ekstrom, G. Johansson, and P. Delsing, "Propagating phonons coupled to an artificial atom", *Science*, vol. 346, no. 6206, pp. 207–211, Oct. 10, 2014. DOI: 10.1126/science.1257219.

[26] T. Aref *et al.*, "Quantum Acoustics with Surface Acoustic Waves", in *Superconducting Devices in Quantum Optics*, ser. Quantum Science and Technology, R. H. Hadfield and G. Johansson, Eds., Cham: Springer International Publishing, 2016, pp. 217–244. DOI: 10.1007/978-3-319-24091-6_9.

[27] R. Manenti *et al.*, "Circuit quantum acoustodynamics with surface acoustic waves", *Nature Communications*, vol. 8, no. 1, p. 975, Dec. 2017. DOI: 10.1038/s41467-017-01063-9.

[28] K. J. Satzinger *et al.*, "Quantum control of surface acoustic-wave phonons", *Nature*, vol. 563, no. 7733, pp. 661–665, Nov. 2018. DOI: 10.1038/s41586-018-0719-5.

[29] B. A. Moores, L. R. Sletten, J. J. Viennot, and K. W. Lehnert, "Cavity Quantum Acoustic Device in the Multimode Strong Coupling Regime", *Physical Review Letters*, vol. 120, no. 22, p. 227 701, May 30, 2018. DOI: 10.1103/PhysRevLett.120.227701.

[30] A. Bienfait *et al.*, "Phonon-mediated quantum state transfer and remote qubit entanglement", *Science*, vol. 364, no. 6438, pp. 368–371, Apr. 26, 2019. DOI: 10.1126/science.aaw8415.

[31] A. Frisk Kockum, P. Delsing, and G. Johansson, "Designing frequency-dependent relaxation rates and Lamb shifts for a giant artificial atom", *Physical Review A*, vol. 90, no. 1, p. 013 837, Jul. 30, 2014. DOI: 10.1103/PhysRevA.90.013837.

[32] G. Andersson, B. Suri, L. Guo, T. Aref, and P. Delsing, "Nonexponential decay of a giant artificial atom", *Nature Physics*, vol. 15, no. 11, pp. 1123–1127, Nov. 2019. DOI: 10.1038/s41567-019-0605-6.

[33] B. Kannan *et al.*, "Waveguide quantum electrodynamics with superconducting artificial giant atoms", *Nature*, vol. 583, no. 7818, pp. 775–779, Jul. 2020. DOI: 10.1038/s41586-020-2529-9.

[34] L. Guo, A. Grimsmo, A. F. Kockum, M. Pletyukhov, and G. Johansson, "Giant acoustic atom: A single quantum system with a deterministic time delay", *Physical Review A*, vol. 95, no. 5, p. 053 821, May 8, 2017. DOI: 10.1103/PhysRevA.95.053821.

[35] H. Hu, R. Ricken, and W. Sohler, "Lithium niobate photonic wires", *Optics Express*, vol. 17, no. 26, pp. 24 261–24 268, Dec. 21, 2009. DOI: 10.1364/OE.17.024261.

[36] P. Rabiei, J. Ma, S. Khan, J. Chiles, and S. Fathpour, "Heterogeneous lithium niobate photonics on silicon substrates", *Optics Express*, vol. 21, no. 21, pp. 25 573–25 581, Oct. 21, 2013. DOI: 10.1364/OE.21.025573.

[37] K. Shibayama, K. Yamanouchi, H. Sato, and T. Meguro, "Optimum cut for rotated Y-cut LiNbO3-crystal used as the substrate of acoustic-surface-wave filters", *Proceedings of the IEEE*, vol. 64, no. 5, pp. 595–597, May 1976. DOI: 10.1109/PROC.1976.10181.

[38] M. Werninghaus, D. J. Egger, F. Roy, S. Machnes, F. K. Wilhelm, and S. Filipp, "Leakage reduction in fast superconducting qubit gates via optimal control", *npj Quantum Information*, vol. 7, no. 1, pp. 1–6, Jan. 29, 2021. DOI: 10.1038/s41534-020-00346-2.

[39] G. Calusine *et al.*, "Analysis and mitigation of interface losses in trenched superconducting coplanar waveguide resonators", *Applied Physics Letters*, vol. 112, no. 6, p. 062 601, Feb. 5, 2018. DOI: 10.1063/1.5006888.

[40] D. P. Morgan, "Surface acoustic wave devices and applications: 1. Introductory review", *Ultrasonics*, vol. 11, no. 3, pp. 121–131, May 1, 1973. DOI: 10.1016/0041-624X(73)90608-2.

[41] R. Gross and A. Marx, *Festkörperphysik*, 3rd ed. De Gruyter, 2018.

[42] M.-A. Dubois and P. Muralt, "Properties of aluminum nitride thin films for piezoelectric transducers and microwave filter applications", *Applied Physics Letters*, vol. 74, no. 20, pp. 3032–3034, May 11, 1999. DOI: 10.1063/1.124055.

[43] J. Campbell and W. Jones, "A method for estimating optimal crystal cuts and propagation directions for excitation of piezoelectric surface waves", *IEEE Transactions on Sonics and Ultrasonics*, vol. 15, no. 4, pp. 209–217, Oct. 1968. DOI: 10.1109/T-SU.1968.29477.

[44] C. Mühlenhoff, "Microwave frequency magnetoacoustic interactions in ferromagnetic thin films", Master's Thesis, WMI/TU Munich, 2017, 81 pp.

[45] G. W. Farnell and E. L. Adler, "2 Elastic Waçe Propagation, in' Thin, Layers", p. 47,

[46] A. Jung, "Characterization of Surface Acoustic Wave Devices on Various Material Systems at Room and Cryogenic Temperatures", Bachelor's Thesis, WMI/TU Munich, 2020, 65 pp.

[47] "Silicon (Si), sound velocities", in *Group IV Elements, IV-IV and III-V Compounds. Part b - Electronic, Transport, Optical and Other Properties*, ser. Landolt-Börnstein - Group III Condensed Matter, O. Madelung, U. Rössler, and M. Schulz, Eds., vol. b, Berlin/Heidelberg: Springer-Verlag, 2002, pp. 1–5. DOI: 10.1007/10832182_448.

[48] M. A. Nielsen and I. L. Chuang, *Quantum Computation and Quantum Information*, 10th anniversary ed. Cambridge ; New York: Cambridge University Press, 2010, 676 pp.

[49] S. Haroche and J.-M. Raimond, *Exploring the Quantum: Atoms, Cavities, and Photons*. Oxford University Press.

[50] C. Gerry and P. Knight, *Introductory Quantum Optics*. Cambridge University Press, 2004, 333 pp.

[51] E. Jaynes and F. Cummings, "Comparison of quantum and semiclassical radiation theories with application to the beam maser", *Proceedings of the IEEE*, vol. 51, no. 1, pp. 89–109, Jan. 1963. DOI: 10.1109/PROC.1963.1664.

[52] M. Saffman, "Quantum computing with atomic qubits and Rydberg interactions: Progress and challenges", *Journal of Physics B: Atomic, Molecular and Optical Physics*, vol. 49, no. 20, p. 202 001, Oct. 28, 2016. DOI: 10.1088/0953-4075/49/20/202001.

[53] C. J. Hood, T. W. Lynn, A. C. Doherty, A. S. Parkins, and H. J. Kimble, "The Atom-Cavity Microscope: Single Atoms Bound in Orbit by Single Photons", *Science*, vol. 287, no. 5457, pp. 1447–1453, Feb. 25, 2000. DOI: 10.1126/science.287.5457.1447.

[54] A. Zrenner, E. Beham, S. Stufler, F. Findeis, M. Bichler, and G. Abstreiter, "Coherent properties of a two-level system based on a quantum-dot photodiode", *Nature*, vol. 418, no. 6898, pp. 612–614, Aug. 2002. DOI: 10.1038/nature00912.

[55] J. Koch *et al.*, "Charge-insensitive qubit design derived from the Cooper pair box", *Physical Review A*, vol. 76, no. 4, p. 042 319, Oct. 12, 2007. DOI: 10.1103/PhysRevA.76.042319.

[56] G. Ithier *et al.*, "Decoherence in a superconducting quantum bit circuit", *Physical Review B*, vol. 72, no. 13, p. 134 519, Oct. 24, 2005. DOI: 10.1103/PhysRevB.72.134519.

[57] J. Goetz, "The Interplay of Superconducting Quantum Circuits and Propagating Microwave States", PhD Thesis, WMI/TU Munich, 2017.

[58] R. Barends *et al.*, "Coherent Josephson Qubit Suitable for Scalable Quantum Integrated Circuits", *Physical Review Letters*, vol. 111, no. 8, p. 080 502, Aug. 22, 2013. DOI: 10.1103/PhysRevLett.111.080502.

[59] D. F. Walls and G. J. Milburn, *Quantum Optics*, 2nd ed. Springer, 2008, 425 pp.

[60] F. Bloch, "Nuclear Induction", *Physical Review*, vol. 70, no. 7-8, pp. 460–474, Oct. 1, 1946. DOI: 10.1103/PhysRev.70.460.

[61] M. Frimmer and L. Novotny, "The classical Bloch equations", *American Journal of Physics*, vol. 82, no. 10, pp. 947–954, Sep. 30, 2014. DOI: 10.1119/1.4878621.

[62] K. X. Wei *et al.*, "Verifying multipartite entangled Greenberger-Horne-Zeilinger states via multiple quantum coherences", *Physical Review A*, vol. 101, no. 3, p. 032 343, Mar. 25, 2020. DOI: 10.1103/PhysRevA.101.032343.

[63] M. Kjaergaard *et al.*, "Superconducting Qubits: Current State of Play", *Annual Review of Condensed Matter Physics*, vol. 11, no. 1, pp. 369–395, Mar. 10, 2020. DOI: 10.1146/annurev-conmatphys-031119-050605.

[64] N. F. Ramsey, "A Molecular Beam Resonance Method with Separated Oscillating Fields", *Physical Review*, vol. 78, no. 6, pp. 695–699, Jun. 15, 1950. DOI: 10.1103/PhysRev.78.695.

[65] E. L. Hahn, "Spin Echoes", *Physical Review*, vol. 80, no. 4, pp. 580–594, Nov. 15, 1950. DOI: 10.1103/PhysRev.80.580.

[66] S. M. Anton *et al.*, "Pure dephasing in flux qubits due to flux noise with spectral density scaling as $1/f^{\alpha}$", *Physical Review B*, vol. 85, no. 22, p. 224 505, Jun. 5, 2012. DOI: 10.1103/PhysRevB.85.224505.

[67] D. M. Pozar, *Microwave Engineering*, 4th ed. Wiley, 2011.

[68] J. Gao, "The Physics of Superconducting Microwave Resonators", PhD Thesis, California Institute of Technology, 2008, 197 pp.

[69] P. Schmidt *et al.*, "Ultrawide-range photon number calibration using a hybrid system combining nano-electromechanics and superconducting circuit quantum electrodynamics", *Applied Physics Letters*, vol. 113, no. 15, p. 152 601, Oct. 8, 2018. DOI: 10.1063/1.5052414.

[70] R. Manenti, "Circuit quantum acoustodynamics with surface acoustic waves", PhD Thesis, University of Oxford, Dec. 2017, 152 pp.

[71] Chin-Chong Tseng, "Frequency response of an interdigital transducer for excitation of surface elastic waves", *IEEE Transactions on Electron Devices*, vol. 15, no. 8, pp. 586–594, Aug. 1968. DOI: 10.1109/T-ED.1968.16406.

[72] G. Andersson, "Quantum acoustics with superconducting circuits", PhD Thesis, Chalmers University of Technology, 2020, 98 pp.

[73] S. Datta, *Surface Acoustic Wave Devices*. Prentice Hall, 1986, 208 pp.

[74] "Interferenz, Beugung und Streuung", in *Experimentalphysik 2: Elektrizität Und Optik*, ser. Springer-Lehrbuch, W. Demtröder, Ed., Berlin, Heidelberg: Springer, 2006, pp. 299–347. DOI: 10.1007/978-3-540-33795-9_10.

[75] R. Manenti, "Surface Acoustic Wave Resonators for Quantum Information", Master's Thesis, University of Milan, 2013, 54 pp.

[76] R. N. Simons, *Coplanar Waveguide Circuits, Components, and Systems*, red. by K. Chang, ser. Wiley Series in Microwave and Optical Engineering. New York, USA: John Wiley & Sons, Inc., Mar. 1, 2001. DOI: 10.1002/0471224758.

[77] I. Besedin and A. P. Menushenkov, "Quality factor of a transmission line coupled coplanar waveguide resonator", *EPJ Quantum Technology*, vol. 5, no. 1, pp. 1–16, Dec. 2018. DOI: 10.1140/epjqt/s40507-018-0066-3.

[78] J. S. Kelly, "Fault-tolerant superconducting qubits", PhD Thesis, University of California, 2015, 207 pp.

[79] F. Deppe, S. Saito, H. Tanaka, and H. Takayanagi, "Determination of the capacitance of nm scale Josephson junctions", *Journal of Applied Physics*, vol. 95, no. 5, pp. 2607–2613, Feb. 19, 2004. DOI: 10.1063/1.1645673.

[80] P. E. Schmidt, "Nanomechanical Quantum Systems", PhD Thesis, WMI/TU Munich, 2019, 191 pp.

[81] R. Igreja and C. J. Dias, "Analytical evaluation of the interdigital electrodes capacitance for a multi-layered structure", *Sensors and Actuators A: Physical*, vol. 112, no. 2, pp. 291–301, May 1, 2004. DOI: 10.1016/j.sna.2004.01.040.

[82] P. S. Cross, "Properties of Reflective Arrays for Surface Acoustic Resonators", *IEEE Transactions on Sonics and Ultrasonics*, vol. 23, no. 4, pp. 255–262, Jul. 1976. DOI: 10.1109/T-SU.1976.30870.

[83] G. J. Dolan, "Offset masks for lift-off photoprocessing", *Applied Physics Letters*, vol. 31, no. 5, pp. 337–339, Sep. 1, 1977. DOI: 10.1063/1.89690.

[84] R. W. Revie and H. H. Uhlig, *Corrosion and Corrosion Control : An Introduction to Corrosion Science and Engineering*, 4th ed. Wiley, 2008, 513 pp.

[85] A. Dunsworth *et al.*, "Characterization and reduction of capacitive loss induced by sub-micron Josephson junction fabrication in superconducting qubits", *Applied Physics Letters*, vol. 111, no. 2, p. 022 601, Jul. 10, 2017. DOI: 10.1063/1.4993577.

[86] C. M. Quintana *et al.*, "Characterization and reduction of microfabrication-induced decoherence in superconducting quantum circuits", *Applied Physics Letters*, vol. 105, no. 6, p. 062 601, Aug. 11, 2014. DOI: 10.1063/1.4893297.

[87] T. H. P. Chang, "Proximity effect in electron-beam lithography", *Journal of Vacuum Science and Technology*, vol. 12, no. 6, pp. 1271–1275, Nov. 1, 1975. DOI: 10.1116/1.568515.

[88] M. Hiebel, *Fundamentals of Vector Network Analysis*. Rohde & Schwarz, 2016, 420 pp.

[89] S. Krinner *et al.*, "Engineering cryogenic setups for 100-qubit scale superconducting circuit systems", *EPJ Quantum Technology*, vol. 6, no. 1, pp. 1–29, Dec. 2019. DOI: 10.1140/epjqt/s40507-019-0072-0.

[90] S. Weichselbaumer, "Spin Dynamics in Strongly Coupled Spin-Photon Hybrids", PhD Thesis, WMI/TU Munich, 2020, 193 pp.

[91] *© Rohde & Schwarz; R&S®SMF100A Microwave Signal Generator datasheet*, 2019.

[92] *© Rohde & Schwarz; R&S®SGS100A SGMA RF Source datasheet.*

[93] S. Probst, F. B. Song, P. A. Bushev, A. V. Ustinov, and M. Weides, "Efficient and robust analysis of complex scattering data under noise in microwave resonators", *Review of Scientific Instruments*, vol. 86, no. 2, p. 024 706, Feb. 1, 2015. DOI: 10.1063/1.4907935.

[94] S. L. Garrett, *Understanding Acoustics: An Experimentalist's View of Sound and Vibration*, ser. Graduate Texts in Physics. Cham: Springer International Publishing, 2020. DOI: 10.1007/978-3-030-44787-8.

[95] M. S. Khalil, M. J. A. Stoutimore, F. C. Wellstood, and K. D. Osborn, "An analysis method for asymmetric resonator transmission applied to superconducting devices", *Journal of Applied Physics*, vol. 111, no. 5, p. 054 510, Mar. 1, 2012. DOI: 10.1063/1.3692073.

[96] J. Wenner *et al.*, "Surface loss simulations of superconducting coplanar waveguide resonators", *Applied Physics Letters*, vol. 99, no. 11, p. 113 513, Sep. 12, 2011. DOI: 10.1063/1.3637047.

[97] M. Pernpeintner, "Nanomechanical hybrid systems", PhD Thesis, WMI/TU Munich, 2016, 147 pp.

[98] J. Yoneda *et al.*, "A quantum-dot spin qubit with coherence limited by charge noise and fidelity higher than 99.9%", *Nature Nanotechnology*, vol. 13, no. 2, pp. 102–106, Feb. 2018. DOI: 10.1038/s41565-017-0014-x.

[99] A. Osman *et al.*, "Simplified Josephson-junction fabrication process for reproducibly high-performance superconducting qubits", *Applied Physics Letters*, vol. 118, no. 6, p. 064 002, Feb. 8, 2021. DOI: 10.1063/5.0037093.

[100] M. V. P. Altoé *et al.* "Localization and reduction of superconducting quantum coherent circuit losses". version 1. (Dec. 14, 2020), [Online]. Available: http://arxiv.org/abs/2012.07604.

[101] J. Goetz *et al.*, "Loss mechanisms in superconducting thin film microwave resonators", *Journal of Applied Physics*, vol. 119, no. 1, p. 015 304, Jan. 5, 2016. DOI: 10.1063/1.4939299.

[102] H. Wang *et al.* "Cryogenic single-port calibration for superconducting microwave resonator measurements". (Mar. 2, 2021), [Online]. Available: http://arxiv.org/abs/2103.01491.

[103] A. E. Siegman, *Lasers*. Mill Valley, California: University Science Books, 1986, 1283 pp.

[104] X. Du *et al.*, "ZnO film for application in surface acoustic wave device", *Journal of Physics: Conference Series*, vol. 76, p. 012 035, Aug. 3, 2007. DOI: 10.1088/1742-6596/76/1/012035.

[105] T. Pastureaud *et al.*, "High-frequency surface acoustic waves excited on thin-oriented LiNbO/sub 3/ single-crystal layers transferred onto silicon", *IEEE Transactions on Ultrasonics, Ferroelectrics, and Frequency Control*, vol. 54, no. 4, pp. 870–876, Apr. 2007. DOI: 10.1109/TUFFC.2007.321.

[106] W. Wang *et al.*, "High performance AlScN thin film based surface acoustic wave devices with large electromechanical coupling coefficient", *Applied Physics Letters*, vol. 105, no. 13, p. 133 502, Sep. 29, 2014. DOI: 10.1063/1.4896853.

[107] M. Li, C. Chen, R. Lu, Y. Yang, T. Wu, and S. Gong, "Temperature Stability Analysis of Thin-Film Lithium Niobate SH0 Plate Wave Resonators", *Journal of Microelectromechanical Systems*, vol. 28, no. 5, pp. 799–809, Oct. 2019. DOI: 10.1109/JMEMS.2019.2934126.

[108] D. Jun *et al.*, "Deep anisotropic LiNbO $_3$ etching with SF $_6$ /Ar inductively coupled plasmas", *Journal of Vacuum Science & Technology B, Nanotechnology and Microelectronics: Materials, Processing, Measurement, and Phenomena*, vol. 30, no. 1, p. 011 208, Jan. 2012. DOI: 10.1116/1.3674282.

[109] H. Smith, *Introduction to Quantum Mechanics*. World Scientific, May 1991. DOI: 10.1142/1271.

Acknowledgements

This thesis would not have been possible without the support and knowledge of several people accompanying me during the last year. In particular, I would like to thank:

Prof. Dr. Rudolf Gross, for giving me the opportunity to complete my Master's thesis here at the Walther-Meißner-Institut.

Priv.-Doz. Dr. Hans Hübl, for offering me this Master's thesis topic, introducing me to the field of hybrid quantum systems and quantum acoustodynamics and constantly providing me with support and ideas. Especially, I want to thank you for always helping me to see the bigger picture and leaving me space to develop and thrive within a provided framework.

Thomas Luschmann, for being a supportive and engaged advisor. It seemed like you had an answer to any question I could ask. I am very grateful for all the fabrication skills, technical insights and physical understanding I was able to learn from you and for your proof reading and support during the writing process of this thesis.

Korbinian Rubenbauer, for being the best imaginable guy to share an office with, for sharing success and (many) failures, productive physical discussions and entertaining whatever-is-on-your-mind conversations.

Dr. Daniel Schwienbacher, for many fruitful discussion about fabrication and physics and general as well as your valuable tips on academia in general.

Lukas Liensberger, Tobias Wimmer, Leon Koch and Janine Gückelhorn, for the diverting lunch breaks, your help in the lab whenever needed and giving an "underachieving Master student" insight into the life of noble PhD students.

Elisabeth Meidinger, Monika Scheufele and Philipp Krüger ,for adopting me in 108 after my old office has been wound up, for keeping me sane during the writing phase of the thesis and the constant supply with sweets and cake as well as inspirational quotes.

The other Master's students, for a pleasant and helpful ambiance.

The whole "Magnetiker"-group for the kind and cooperative atmosphere, for the easy sharing of measurement equipment and labs and for always having an open ear for problems and physics related questions.

All the other Postdocs and PhD students at the WMI, for providing support and advice whenever needed.

Thomas Brenninger and Sebastian Kammerer, for maintaining the technical facilities at the WMI and keeping the inevitable downtimes to a minimum.

The workshop team, Alex Rössl, Georg Nitschke, Christian Reichlmeier and Mario Nodes, for coming up with solutions for any technical problem I encountered and immediate help whenever needed.

All members of the WMI, for the kind and helpful atmosphere which contributed to the successful outcome of the experiments.

My girlfriend Nina Miller, for your support, listening to me thinking out loud and believing in me.

My parents, Uschi and Roman Waas, for their unconditional support at any time when I needed it and for giving me the freedom to make my own decisions. I would also like to thank you for enabling me to study here in Munich. Thank you for everything!